“Reality is that which, when you stop believing in it, doesn’t go away.”
Philip K. Dick

University of Alberta

Towards a Radiation Hardened Fluxgate Magnetometer for Space Physics Applications

by

David M. Miles

A thesis submitted to the Faculty of Graduate Studies and Research

in partial fulfillment of the requirements for the degree of

Master of Science

Department of Physics

Spring 2013
Edmonton, Alberta

To my daughter Cassandra — if you decide to write one of these things, may you do it faster than your old man.

Abstract

Space-based measurements of the Earth's magnetic field are required to understand the plasma processes of the solar-terrestrial connection which energize the Van Allen radiation belts and cause space weather. This thesis describes a fluxgate magnetometer payload developed for the proposed Canadian Space Agencys Outer Radiation Belt Injection, Transport, Acceleration and Loss Satellite (ORBITALS) mission. The instrument can resolve 8 pT on a 65,000 nT field at 900 samples per second with a magnetic noise of less than 10 pT per square–root Hertz at 1 Hertz. The design can be manufactured from radiation tolerant (100 krad) space grade parts. A novel combination of analog temperature compensation and digital feedback simplifies and miniaturises the instrument while improving the measurement bandwidth and resolution. The prototype instrument was successfully validated at the Natural Resources Canada Geomagnetics Laboratory, and is being considered for future ground, satellite and sounding rocket applications.

Acknowledgements

This thesis describes the improvement, extension and modernisation of an instrument design developed by Magnametrics, Narod Geophysics Ltd., and Bennest Enterprises Ltd. for the CASSIOPE/e-POP satellite. The analog electronics described herein were developed in close collaboration with Bennest Enterprises Ltd. The digital electronics were developed with the help of the Department of Physics Electronics Shop at the University of Alberta.

This thesis would not have been possible without the help and support of my supervisor Professor Ian Mann and a great many people including: David Barona, John Bennest, Bill Burris, Miroslaw Ciurzynski, Paul Davis, Alex Degeling, Andy Kale, Jeffrey Kavanaugh, Shengli Liu, Richard Marchand, David Milling, Kyle Murphy, Barry Narod, Louis Ozeke, Jonathan Rae, Jonathan Schmidt, Martyn Unsworth, Don Wallis, and Clare Watt.

I would like to acknowledge the Canadian Space Agency for their financial support and the opportunity to work on several interesting projects.

My deepest gratitude goes to my family: my wife Jessy, my daughter Cassie, my father Mike, my mother Wynne, my sister Sarah, and my dog Caddy. I never would have finished without their help and encouragement. Thanks for putting up with me.

Any errors or omissions are entirely my own.

Contents

Contents i

List of Tables vi

List of Figures vii

Acronyms x

1 Introduction 1

1.1 Motivation 1

1.2 Thesis Scope and Overview 2

1.3 The Solar-Terrestrial Connection 4

1.3.1 Solar Driving and Space Weather 4

1.3.2 Regions of the Ionosphere and Magnetosphere 7

1.3.3 Magnetometers for Solar System Exploration 10

1.4 Magnetic Measurements and Space Physics Research 11

1.4.1 Field Geometry and Features 12

1.4.2 Poynting Vector 12

1.4.3 Charged Particle Motion 12

1.4.4 Electromagnetic Waves 13

1.4.5 Particle Trapping and Pitch Angle 14

1.4.6 The Significance of Magnetic Measurements 15

1.5 Science Targets Requiring Fluxgate Measurements 16

1.6 Planned Missions With Fluxgate Instruments 17

2 Satellite Measurements of the Earth's Magnetosphere **20**

2.1 Representative Mission: CSA ORBITALS 20

2.1.1 Mission Science Overview 21

2.1.2 Orbit Parameters 23

2.1.3 Instrument Payload . . . 23
2.1.4 Spacecraft Overview . . . 24
2.2 Relevant Mission Data Requirements . . . 26
2.2.1 Magnetic Field Measurements as a Primary Data Product . . . 26
2.2.2 Magnetic Field Data as a Supporting Data Product . . . 28
2.2.3 Summary of Data Requirements . . . 28
2.3 Key Constraints Imposed by the Mission, Platform, and Environment . 29
2.3.1 Magnetic Field Strength . . . 29
2.3.2 Magnetic Signal from a Spinning Spacecraft . . . 30
2.3.3 Radiation Environment . . . 31
2.3.3.1 Total Integrated Dose . . . 31
2.3.3.2 Single Event Upsets . . . 33
2.3.3.3 Internal Charging . . . 34
2.3.4 Thermal Environment . . . 35
2.3.5 Electromagnetic Cleanliness . . . 36
2.3.6 Reliability Requirement . . . 36
2.3.7 Summary of Constraints . . . 38

3 Review of Fluxgate Magnetometers 40
3.1 Fluxgate Sensor Physics . . . 40
3.1.1 The Generalised Induction Equation . . . 40
3.1.2 Fluxgate Sensor Head Layouts . . . 41
3.1.3 Magnetic Feedback . . . 43
3.1.4 Other Sensor Layouts . . . 43
3.1.5 Standard Detection Technique . . . 44
3.2 Review of Recent Fluxgates for Space Applications . . . 45
3.2.1 CASSIOPE/e-POP MGF . . . 45
3.2.2 Imperial College London - Prototype . . . 46
3.2.3 THEMIS FGM Instrument . . . 47
3.2.4 The State of the Art . . . 49

4 Radiation Hard Spaceflight Instrument Design 50
4.1 System Architecture and Nomenclature . . . 50
4.2 Instrument Heritage . . . 50
4.3 Concept of Operations . . . 51
4.3.1 Sensor Design . . . 51

4.3.2 Instrument Concept 54
4.4 Major Functional Subsystems 55
4.5 Preliminary Interface Design 57
4.5.1 Power Supply and Grounding Interface 57
4.5.2 Command and Control Interface 57
4.5.3 Data Handling and Telemetry Interface 58
4.5.4 Deployment on a Boom 59
4.5.5 Thermal Interface 59
4.6 Operating Modes 60
4.6.1 Nominal Operation 60
4.6.2 In-Flight Calibration 60
4.6.3 Contingency Operation 61
4.6.4 Startup and Shutdown 61
4.6.5 Failure Mode Mitigation 61
4.7 Trade Off Studies and Design Choices 62
4.7.1 Offsetting Versus Gain Ranging 63
4.7.2 Radiation Hardened Analog to Digital Conversion 64
4.7.3 Radiation Tolerant FPGA Controller 65
4.7.4 Drive Frequency 67
4.7.5 Core Selection 67
4.8 Selected Design Improvements 68
4.8.1 Susceptibility to Ambient 60 Hz Noise. 68
4.8.2 Maximum Rate of Change 69
4.8.3 Temperature Compensation 69
4.8.4 100 krad Radiation Hardening 70
4.8.5 Size and Parts Count 71
4.9 Detailed Implementation of Selected Subsystems 71
4.9.1 Extracting Information from the fluxgate Sensor 72
4.9.2 Dual Pulse Width Modulation Feedback 77
4.9.3 Control Loop 84
4.9.4 Thermally Stabilized Reference 87
4.10 Instrument Design Summary 91

5 Instrument Characterization **92**
5.1 Test Facilities and Experimental Set-up 92
5.1.1 National Resources Canada Geomagnetics Laboratory 92

5.1.2 CARISMA Laboratory — University of Alberta 93
5.2 Spectral Analysis Techniques 94
5.3 Operation of Instrument 95
5.4 Instrument Performance Under Test 96
5.4.1 Test 1 — Instrument Resolution 96
5.4.2 Test 2 — Magnetic Noise 100
5.4.3 Test 3 — Measurement Accuracy 102
5.4.4 Test 4 — Instrument Slew Rate 103
5.5 Instrument Calibration 106
5.5.1 Error Signal Scaling 106
5.5.2 Fine Pulse Width Modulation Scaling 107
5.5.3 Coarse Pulse Width Modulation Scaling 107
5.5.4 Offset Correction 107
5.5.5 Absolute Calibration 108
5.6 Limitations of Current Prototype 109
5.6.1 Step Transients 109
5.6.2 Induction Coil Pickup 110
5.6.3 High Frequency Aliasing 111
5.7 High Frequency Performance 112

6 Conclusions and Future Work **116**
6.1 Comparison of Prototype to Previous Designs 116
6.2 Performance Versus Mission Requirements 117
6.3 Conclusions 118
6.4 Future Work 118

Bibliography **120**

A Spectral Analysis **125**
A.1 Techniques Used In This Thesis 125
A.2 Types of Fourier Transforms 125
A.3 Converting Between Amplitude and PSD 126
A.4 Parameter Selection 127
A.4.1 Normalisation of the DFT 127
A.4.2 Number of Frequency Bins 127
A.4.3 Window Functions 128
A.4.4 Minimum Spectral Separation 131

A.4.5 Averaging 131
A.5 Implementation of Spectral Transforms 132
A.5.1 Implementation of Power Spectral Density 132
A.5.2 Implementation of Amplitude Spectrum 133
A.6 Performance Using Synthetic Data 134
A.7 Performance Using Measured Data 137
A.7.1 Performance of Power Spectral Density Spectrum Calculation . . 137
A.7.2 Performance of Amplitude Spectrum Calculation 140

List of Tables

2.1 Potential mission orbits and their parameters. 23
2.2 Electromagnetic wave amplitudes from previous missions. 27
2.3 Instruments required for each science objective. 37

3.1 Performance characteristics of relevant spaceflight fluxgate magnetometers. 49
3.2 Performance characteristics of a state-of-the-art spaceflight fluxgate. . . 49

4.1 Summary of instrument requirements. 62
4.2 Technical performance metrics and current values. 63
4.3 Verilog synthesis results for a rad-hard RTAX250 target. 66
4.4 Selected commercial parts and radhard equivalents. 70

5.1 Calibration coefficients of prototype instrument. 109

6.1 Current prototype compared to the state-of-the-art spaceflight fluxgate. 116
6.2 Performance of prototype instrument against mission requirements. . . . 117

A.1 Different outputs of the Discrete Fourier Transform 126
A.2 Measured Power Spectral Density using different numbers of spectral bins.140
A.3 Measured amplitude using different numbers of spectral bins. 143

List of Figures

1.1 Artist's rendition of the Earth's magnetosphere. 5
1.2 Idealised interaction of the solar wind and terrestrial magnetic fields. . . 6
1.3 Flow of plasma within the magnetosphere due to magnetic reconnection. 7
1.4 Regions and currents in the magnetosphere. 8
1.5 Artist's depiction of the Earth's inner and outer radiation belts 9
1.6 Electron density regions of the ionosphere at different altitudes. 10
1.7 The crustal magnetic field of Mars as measured by Mars Global Surveyor. 11
1.8 Gyro, bounce and drift motion in a dipole magnetic field. 13
1.9 Pitch angle α of a charged particle moving through a magnetic field. . . 14
1.10 Charged particle mirroring in the Earth's dipole field. 15
1.11 The cusp region of the Earth's magnetic field. 18

2.1 Schematic representation of the ORBITALS Spacecraft. 21
2.2 Dynamics of the radiation belts in three energy ranges from CRRES. . . 22
2.3 Major features of the ORBITALS spacecraft. 25
2.4 Potential wave frequencies at different distances from the Earth 27
2.5 Local magnetic field strength over two representative raised perigee orbits. 30
2.6 Example spin-tone contaminated magnetic data from THEMIS. 31
2.7 Shielding thickness and radiation total integrated dose. 32
2.8 Shielding thickness and modelled short-term flux of electron radiation. . 35

3.1 Conceptual fluxgate sensor using a moving nail and coil of wire. 41
3.2 Single axis fluxgate sensor layout using a rod core. 42
3.3 Single axis fluxgate sensor layout using a ring core. 43
3.4 Block diagram of a second harmonic fluxgate magnetometer. 44
3.5 THEMIS fluxgate magnetometer sensor schematic. 48

4.1 Layout of X, Y, and Z component axes of the fluxgate sensor. 52

4.2 Wiring schematic of the X, Y, and Z components and the drive coil. . . 53
4.3 Fluxgate sensor - CASSIOPE/e-POP engineering model 53
4.4 Block diagram of a second harmonic fluxgate magnetometer. 54
4.5 Schematic of one fluxgate component showing the major components. . 55
4.6 Major functional subsystems of the fluxgate magnetometer. 56
4.7 Example data packet from CASSIOPE/e-POP. 58
4.8 Actel RTAX radiation hardened product line. 66
4.9 Relative size of new and old fluxgate electronics and sensor. 71
4.10 Equivalent circuit of a the sense coil in a short-circuit. 72
4.11 Equivalent circuit of the sensor preamplifier design. 73
4.12 Modulation of the 2f major carrier at various magnetic field strengths. . 74
4.13 V_{out} at various applied magnetic field strengths. 76
4.14 Transducer response versus applied magnetic fields. 77
4.15 Block diagram of the dual pulse width modulation feedback network. . . 79
4.16 Residuals pulse width modulation signal in $V_{feedback}$. 79
4.17 Schematic of phase variation in a single edge pulse width modulation. . 80
4.18 Phase synchronised pulse width modulation. 81
4.19 Asymmetric double edge pulse width modulation. 82
4.20 Pulse width modulation level translation for a negative going pulse. . . 83
4.21 Pulse width modulation level translation for two positive going pulse. . 84
4.22 Accumulation algorithm for analog to digital converter measurements. . 85
4.23 Control logic for the coarse and fine pulse width modulations 86
4.24 Algorithm to calculate science data from internal values. 87
4.25 Schematic for thermally controlled Zener reference diode. 89
4.26 Thermal isolation for the Zener reference diode. 90
4.27 Test-bed for thermally controlled Zener reference diode. 90

5.1 Simplified schematic of NRCan Geomagnetics Laboratory Facility. . . . 93
5.2 Test setup photo. NRCan, Geomagnetics Laboratory, Building 8. 93
5.3 Test setup schematic of UAlberta CARISMA laboratory. 94
5.4 Test setup photo at UAlberta CARISMA laboratory. 94
5.5 Operation and data flow in prototype instrument. 95
5.6 Custom Labview based real–time data capture and visualisation tool . . 96
5.7 Amplitude spectrum - No test signal. 98
5.8 Amplitude spectrum - 18 pT-RMS at 10 Hz signal. 98
5.9 Amplitude spectrum - 18 pT-RMS at 1 Hz signal. 99

5.10 Amplitude spectrum - 18 pT-RMS at 0.1 Hz signal. 99
5.11 Amplitude spectrum - 18 pT-RMS at 0.01 Hz signal. 100
5.12 Amplitude spectrum - 18 pT-RMS at 0.001 Hz signal. 100
5.13 Power spectral density noise floor of the fluxgate magnetometer. 101
5.14 Low frequency power spectral density noise floor. 102
5.15 Linearity of the fluxgate magnetometer X component. 103
5.16 Correctly nulled instrument showing small error signal. 104
5.17 Out-of-range instrument showing large and asymmetric error signal. . . 105
5.18 Successfully tracking the worst-case ORBITALS spin field. 106
5.19 180^o sensor rotation to estimate sensor offset. 108
5.20 Residual contamination from coarse pulse width modulation steps. . . . 110
5.21 Induction coil pickup from the fluxgate magnetometer sensor. 111
5.22 550 Hz test signal aliased to 350 Hz. 112
5.23 Amplitude spectrum - 18 pT-RMS at 100 Hz signal. 113
5.24 Amplitude spectrum - 18 pT-RMS at 400 Hz signal. 113
5.25 2f major carrier sideband modulation by sinusoidal magnetic fields. . . . 115

A.1 Parameters of a Hanning window function. 129
A.2 Parameters of a HFT95 flat-top window function. 130
A.3 Segmented windowed time series with no overlap. 132
A.4 Segmented windowed time series with overlapping segments. 132
A.5 Performance of spectral analysis using synthetic data 135
A.6 Performance of spectral analysis using synthetic data 136
A.7 Power spectral density with various numbers of spectral bins. 138
A.8 Zoomed power spectral density with various numbers of spectral bins. . 139
A.9 Amplitude spectra with various numbers of spectral bins. 141
A.10 Zoomed amplitude spectra with various numbers of spectral bins. 142
A.11 Measured test signal amplitude using different numbers of spectral bins. 143

Acronyms

AC Alternating Current

AM Amplitude Modulation

ADC Analog to Digital Converter

CARISMA Canadian Array for Realtime InvestigationS of Magnetic Activity

CASSIOPE CAScade, Smallsat and IOnospheric Polar Explorer

CGSM Canadian GeoSpace Monitoring

CODIF COmposition and DIstribution Function

CRAND Comic Ray Albedo Neutron Decay

CRRES Combined Release and Radiation Effects Satellite

CSA Canadian Space Agency

DAC Digital to Analog Converter

DDCM Dielectric Deep Charge Monitor

DFT Discrete Fourier Transform

EEPS Energetic Electron Proton Spectrometer

EFW Electric Fields and Waves

ELDRS Enhanced Low Dose Rate Sensitivity

ELF Extremely Low Frequency

EMC Electromagnetic Cleanliness

EMIC Electromagnetic Ion Cyclotron

ENBW Effective Noise Bandwidth

e-POP Enhanced Polar Outflow Probe

ESA European Space Agency

FFT Fast Fourier Transform

FGM Fluxgate Magnetometer

FPGA Field Programmable Gate Array

GPS Global Positioning System

HDL Hardware Description Language

HEPT High Energy Proton Telescope

I-SWEAT Ionospheric Space Weather Effects in the Auroral Thermosphere

ICI Investigation of Cusp Irregularities

IDPU Instrument Data Processing Unit

ILWS International Living With a Star

IMF Interplanetary Magnetic Field

ITAR International Traffic in Arms Regulations

JAXA Japan Aerospace Exploration Agency

LET Linear Energy Transfer

LS Linear Spectrum

LSD Linear Spectral Density

LSB Least Significant Bit

MGF Magnetic Field Instrument

MLI Multi Layer Insulation

MORE Mission of Opportunity, Radbelt Explorer

MRD Mission Requirements Document

NASA National Aeronautics and Space Administration

NENBW Normalised Effective Noise Bandwidth

NFFT number of spectral bins

NGL Narod Geophysics Ltd

NRCan National Resources Canada

ORBITALS Outer Radiation Belt Injection, Transport, Acceleration and Loss Satellite

PA Power Amplifier

PCU Power Control Unit

PCW Polar Communications and Weather

PID Proportional Integral Derivative

PII Plasmaspheric Ion Imager

PRIMO Plasma and Radiation In Molniya Orbit

PS Power Spectrum

PSD Power Spectral Density

PWM Pulse Width Modulation

RAAN Right Ascension of the Ascending Node

RAM Random Access Memory

RBSP Radiation Belt Storm Probes

$\mathbf{R_E}$ Earth Radii

REM Radiation Environment Monitor

REPT Relativistic Electron Proton Telescope

RMS Root Mean Square

SCM Searchcoil Magnetometer

SCOPE cross Scale COupling in Plasma universE

SSA Space Situational Awareness

THEMIS Time History of Events and Macroscale Interactions during Substorms

TBD To Be Determined

TID Total Integrated Dose

ULF Ultra Low Frequency

UAlberta University of Alberta

UTC Coordinated Universal Time

Chapter 1

Introduction

1.1 Motivation

Modern society increasingly relies on space-based infrastructure to support a range of services such as Earth observation, telecommunications, Global Positioning System (GPS) navigation, and electronic banking. Unfortunately, as society becomes increasingly dependent on this technology, it also becomes increasingly vulnerable to natural processes that may disrupt, affect or damage the underlying technological infrastructure. Space weather is a general term for the volatile near-Earth conditions caused by the interaction of the Sun, the interplanetary medium and the Earth's magnetosphere. Baker [1998] described how space weather is increasingly understood to be a major challenge to the long-term, reliable operation of space- and ground-based technology.

Governments and policy makers appear to be starting to take this issue seriously. For example, Britain's Meteorological Office and the USA's Space Weather Prediction Center recently signed an agreement to share data and cooperate in their work on space weather. Holdrew & Beddington [2011], the science and technology adviser to US President Barack Obama and the chief scientific adviser to UK Prime Minister David Cameron, respectively, published the motivation for this agreement in a New York Times article. They note that:

> "Space weather can affect human safety and economies anywhere on our vast wired planet, and blasts of electrically-charged gas travelling from the Sun at up to five million miles an hour can strike with little warning. Their impact could be big — on the order of $2 Trillion during the first year in the United States alone, with a recovery period of 4 to 10 years."

Canadian examples of the damaging effects of space weather include the March 13, 1989 Hydro-Québec blackout [Bolduc, 2002] and the impacts on satellites such as the temporary loss and then degraded recovery of two ANIK communication satellites in January 1994 [Shea & Smart, 1998].

The future prediction and mitigation of space weather effects will require an in-depth understanding of the physical processes that control the near-Earth environment. The complexity of this problem will require better experimental data from the Earth's magnetosphere, including a better characterisation of the Van Allen radiation belts. The radiation belts span a region of desirable satellite orbits which are under-utilised because of threat posed by the radiation environment. Studies of this region are critical to quantify and predict the threat from radiation and understand the processes which control its variability. This thesis describes the design of a radiation hardened Fluxgate Magnetometer (FGM) to make high-precision scientific magnetic measurements for future missions targeting space weather and which must operate in harsh radiation environments.

1.2 Thesis Scope and Overview

A fluxgate magnetometer designed for space applications must survive and operate reliably in the technically challenging space environment. Simultaneously, the instrument must meet stringent measurement criteria to provide reliable, high resolution data of scientific utility. Space physics missions can differ dramatically in terms of duration, radiation dose, magnetic field strength, temperature, available mass and power, and scientific objectives so that no one instrument will be optimal for all applications. The instrument described in this thesis was first designed for the Canadian Space Agency (CSA) Outer Radiation Belt Injection, Transport, Acceleration and Loss Satellite (ORBITALS) small satellite mission [Mann et al., 2006] and was subsequently updated for potential use with the CSA Plasma and Radiation In Molniya Orbit (PRIMO) secondary science payload [Mann et al., 2011] proposed for the Polar Communications and Weather (PCW) satellite mission [Trishchenko & Garand, 2011]. Both missions are described in Section 1.6. For the purposes of this thesis, the ORBITALS small satellite mission is treated as the target application.

The scope of work encompassed by this thesis included:

- Defining and quantifying the measurement requirements for the ORBITALS fluxgate magnetometer payload. This was completed under the direction of the mission's Principal Investigator, Prof. Ian Mann, and the Instrument Lead, Dr. David Milling.
- Defining and quantify the constraints imposed by the mission and the satellite platform.
- Developing an instrument concept which could meet the mission's requirements and constraints using space grade and radiation hardened components.
- Developing analog electronics subsystems and printed circuit boards for the new instrument. This was completed in a collaboration with industrial contractor Bennest Enterprises Ltd.
- Developing digital electronics subsystems and printed circuit boards for the new instrument. The implementation and fabrication of the digital subsystem printed

circuit board was completed by the Department of Physics Electronics Shop at the University of Alberta.

- Developing firmware to acquire and process raw readings from a fluxgate sensor into magnetic field measurements.
- Developing a firmware control system to provide digital magnetic feedback to linearise and null the fluxgate sensor.
- Integrating and testing the new instrument using an existing fluxgate sensor.
- Calibrating, analysing and validating the prototype instrument's performance. This was completed with assistance from Dr. Don Wallis using the facilities at the National Resources Canada (NRCan) Geomagnetism Laboratory and the University of Alberta (UAlberta) Canadian Array for Realtime InvestigationS of Magnetic Activity (CARISMA) laboratory.

The remaining sections of Chapter 1 briefly reviews some of the science targets which can be addressed with a fluxgate magnetometer to provide context and describe the motivation and applications for this type of instrument. Section 1.3 describes some of the basic physical processes underlying space plasma physics and space weather. Section 1.4 briefly reviews some of the science objectives that require magnetic field measurements. Section 1.5 discusses literature from the space plasma physics community which illustrate the need for these measurements. Section 1.6 reviews a selection of future planned satellite and rocket missions requiring magnetic measurements and which require high quality FGM instrumentation.

Chapter 2 briefly describes the ORBITALS mission, reviews the mission's science measurement requirements and discusses the constraints imposed by the mission and the operational environment.

Chapter 3 provides the theoretical background to how a fluxgate magnetometer works. The physics of the sensor head is described and a review of previous spaceflight fluxgate magnetometers is provided to document recent advances in fluxgate design and establish the state-of-the-art in spaceflight fluxgate magnetometery.

The instrument presented in this thesis is referred to as the Fluxgate Magnetometer (FGM). The underlying fluxgate design has more than two decades of terrestrial heritage through the CANOPUS/CARISMA [Rostoker et al., 1995; Mann et al., 2008], POLARIS [Eaton et al., 2005], and EMScope/EarthScope USArray [Schultz, 2009] instruments built by Narod Geophysics Ltd (NGL) [e.g., Narod & Bennest, 1990]. The NGL design has previously been modified for low-radiation space applications as the Magnetic Field Instrument (MGF) [Wallis et al., 2006] in the CSA's Enhanced Polar Outflow Probe (e-POP) payload on the CAScade, Smallsat and IOnospheric Polar Explorer (CASSIOPE) satellite. Chapter 4 reviews the heritage of the instrument design, its concept of operations and the major functional units within the instrument. The instrument improvements that have been incorporated into the new design are presented, and the relevant design choices and their implications are discussed. Finally, a detailed description of the design and implementation is provided for selected instrument subsystems. These were selected to show the breadth of factors that need to be considered for a radiation hardened space based instrument.

The FGM design presented in this thesis resulted in a prototype instrument developed to demonstrate the feasibility of meeting the ORBITALS measurement requirements with a space–based, radiation hardened fluxgate magnetometer. Since the actual flight of the instrument is beyond the scope of the thesis, Chapter 5 presents the laboratory testing and calibration performed on the prototype instrument. The performance of the prototype instrument is demonstrated with respect to the defined mission measurement requirements and goals. The limitations of the current design are also briefly discussed.

Chapter 6 compares the prototype to previous instruments, highlights the achieved science performance and discusses potential future work and application for the instrument.

1.3 The Solar-Terrestrial Connection

1.3.1 Solar Driving and Space Weather

The proceedings of the 6th Canadian Space Exploration Workshop in 2009 (`http://www.asc-csa.gc.ca/pdf/csew6_rapport-2009-05-30_en.pdf`) observed that:

> "Space is fundamentally a harsh environment — an environment that is both invisible and dominated by plasma (ionized gas), electric and magnetic fields and energetic particle radiation. The harsh conditions of space necessitate a better understanding of the environment through solar-terrestrial science in order to enable Global Space Exploration ..."

The Earth's magnetic field extends into space and is confined by the solar wind into a tear drop shaped cavity called the magnetosphere. The shape of the magnetosphere is primarily determined by the interaction of the Earth's magnetic field with charged particles and interplanetary magnetic field supplied by the Sun in the form of the solar wind. The Earth's magnetic field also receives the plasma outflow from the Earth's ionosphere. The Earth's magnetosphere is compressed on the dayside, where it is impacted by the solar wind of the rarefied plasma blowing outwards from the Sun. Similarly, the magnetosphere is stretched away from the Sun on the nightside as illustrated schematically in Figure 1.1.

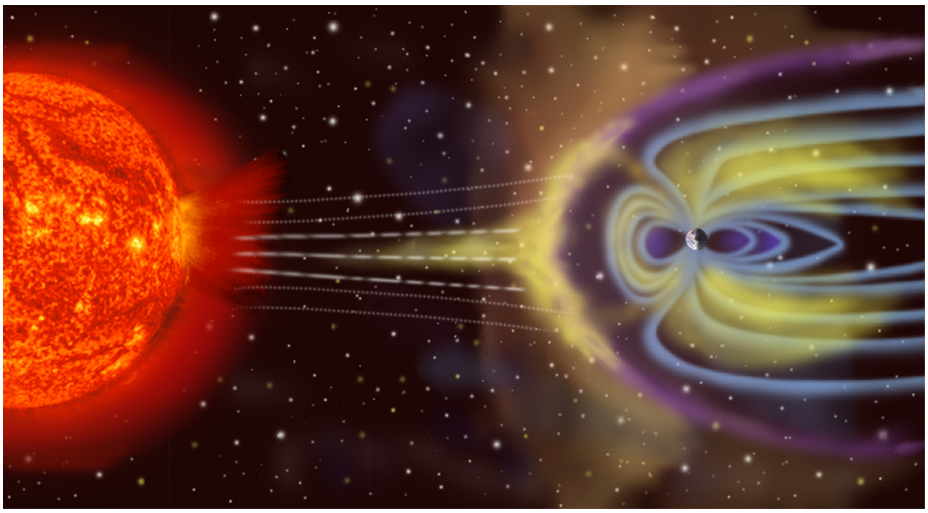

Figure 1.1: Artist's rendition of the Earth's magnetosphere. Image courtesy of NASA.

The magnetic fields originating from the Earth and the Sun can sometimes be connected as shown in Figure 1.2, through a process known as magnetic reconnection. Dungey [1963] described how when the Interplanetary Magnetic Field (IMF) has a southward component (Figure 1.2, top), it can connect to the Earth's magnetic field on the day-side, sweep over the poles, and reconnect again on the night-side, resulting in a cyclical convection process referred to as the Dungey cycle. When the IMF is aligned northward with the Earth (Figure 1.2, bottom), the IMF stands off from the Earth's magnetic field on the dayside, although reconnection can still occur at high latitudes in the nightside lobes.

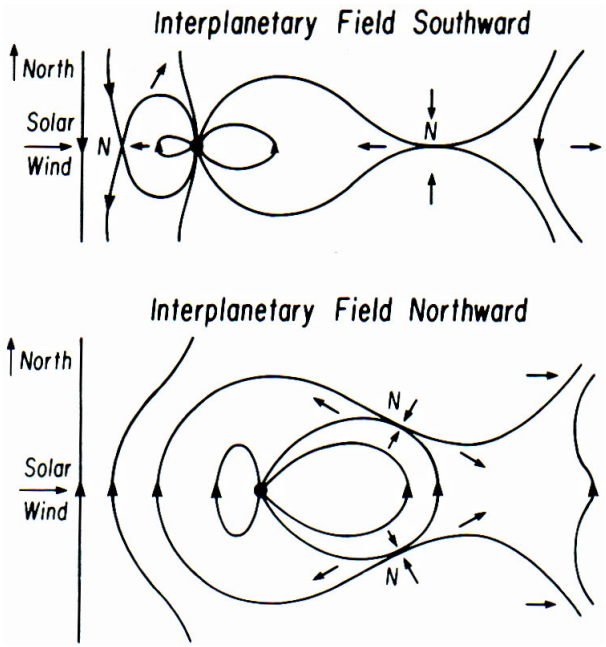

Figure 1.2: Idealised interaction of the solar wind and terrestrial magnetic fields showing magnetic reconnection. (Top) Southward IMF. (Bottom) Northward IMF. Taken from Kivelson & Russell [1995] following Dungey [1963].

Figure 1.3 shows how the Dungey cycle causes plasma to flow within the magnetosphere. The IMF connects to the Earth's magnetic field on the day-side, sweeps over the poles, and reconnects in the night-side sweeping magnetic fields and plasma in towards the Earth, around the flanks at low latitudes and back towards the dayside, through the sequence labelled 1 through 9 in Figure 1.3. This cycle creates a convection cell that the ends of the magnetic field lines trace out near the north and south poles shown in the bottom of Figure 1.3.

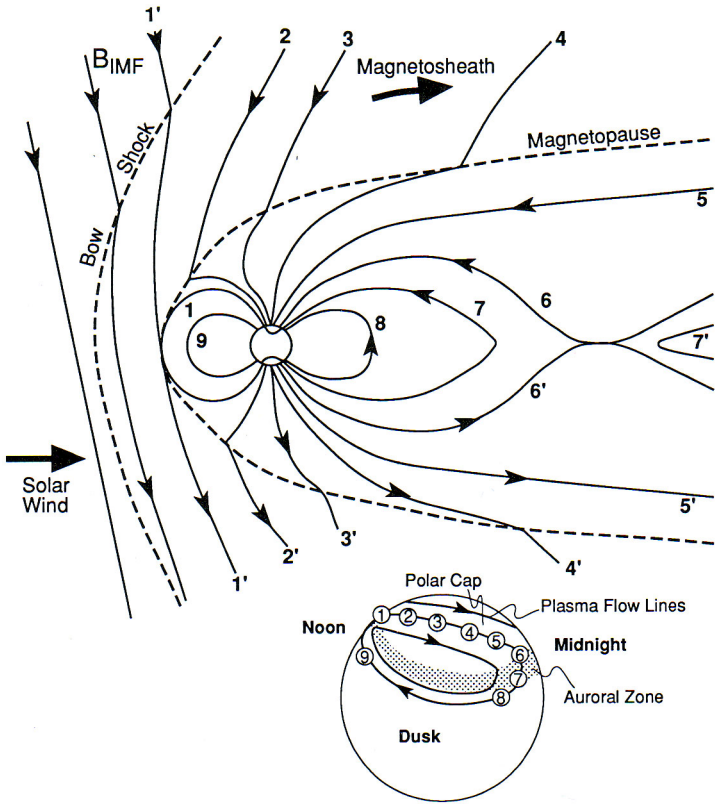

Figure 1.3: Flow of plasma within the magnetosphere due to magnetic reconnection. Taken from Kivelson & Russell [1995].

Magnetic reconnection couples the output of the Sun to the Earth's magnetosphere providing a power source for space weather processes. Magnetic measurements allow us to study when and how this coupling occurs, where the energy is transported, and under what conditions energy is stored into the magnetosphere or dissipated in to the Earth's atmosphere. Understanding these complicated, large scale processes will likely require multipoint measurements via satellite constellations (e.g., Angelopoulos et al. [2008], Escoubet et al. [2001]).

1.3.2 Regions of the Ionosphere and Magnetosphere

The principal features and regions of the magnetosphere are indicated in Figure 1.4. The Earth's primarily dipole magnetic field is compressed on the sunward dayside and is extended on the nightside. This complex geometry supports a variety of currents and magnetic waves, which transport mass, energy, and momentum through the magnetosphere. Magnetic field measurements are used to characterise the size and shape of the magnetosphere, to look for the magnetic signatures of electrical current flows, and to study the magnetic waves thought to drive mass, charge, energy, and momentum transport within the magnetosphere. The plasmasphere is the inner region of the magnetosphere and is made up of low energy plasma. The plasmasphere's outer boundary, the plasmapause, is defined by a sudden drop in plasma density.

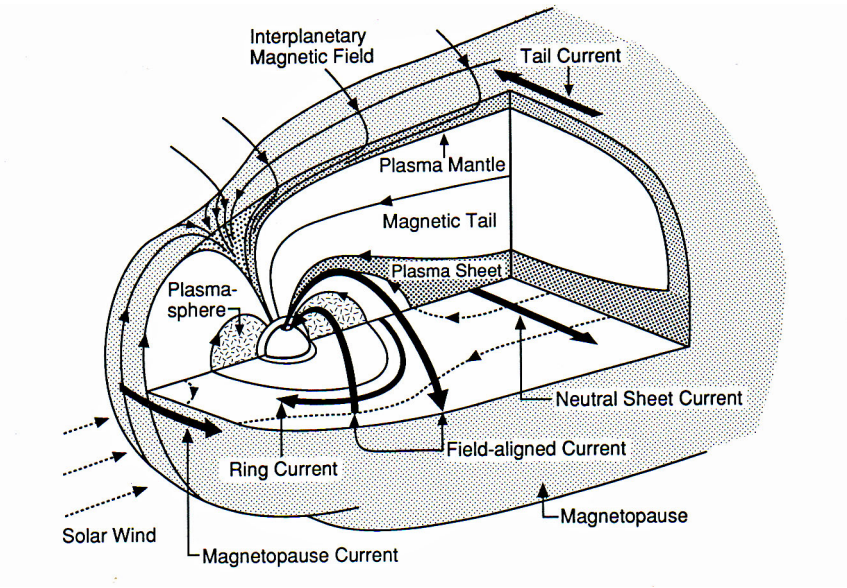

Figure 1.4: Regions and currents in the magnetosphere. Taken from Kivelson & Russell [1995].

The charged particles which make up space plasma and energetic particle radiation cannot move without being affected by, and affecting, the local magnetic field. Particles can be accelerated and trapped into concentrated torus-shaped regions called the Van Allen radiation belts (See Figure 1.5). The inner belt occurs at a geocentric altitude of around 1-3 Earth Radii (R_E), typically residing within the plasmasphere as shown in Figure 1.4. The outer belts occur at geocentric altitudes of around 4-7 R_E and the inner edge of the radiation belts is believed to track the plasmapause [Li et al., 2006]. Energetic protons in the inner belt are thought to be due, at least partially, to the decay of neutrons that are produced by the interaction of the atmosphere with cosmic rays, in a process called Comic Ray Albedo Neutron Decay (CRAND) [e.g., Freden & White, 1962]. One of the candidate sources for the energetic electron populations in the inner and outer belts is acceleration through a resonant interaction of electrons with electromagnetic waves. At times, especially during the main phase of magnetic storms, a large fraction of the radiation belts can be lost into the Earth's atmosphere due to local conditions including effects due to the strength and shape of the Earth's magnetic field or by scattering into the atmosphere by interacting with various plasma waves (e.g., review by Millan & Thorne [2007]). Within the Van Allen belts, the trapped radiation can be long-lived and can damage and degrade in-situ instrumentation, making it challenging to collect scientific measurements within the radiation belts. The fluxgate magnetometer instrument developed for this thesis is designed to survive and operate in this harsh radiation environment and to provide high precision magnetic measurements in this understudied and critical region.

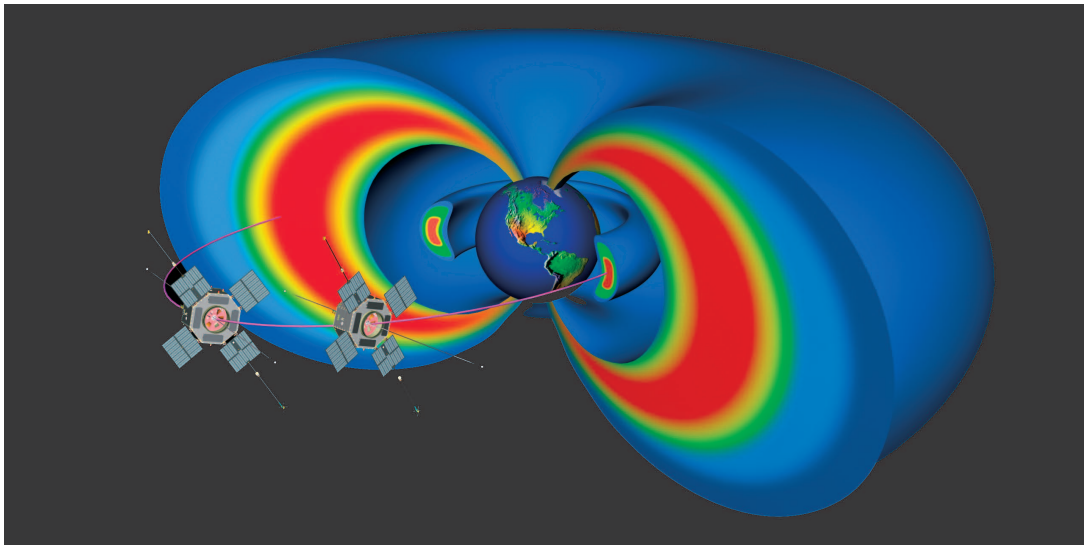

Figure 1.5: Artist's depiction of the Earth's inner and outer radiation belts. The two spacecraft are the NASA Radiation Belt Storm Probes (RBSP) satellites intended to study the radiation belts. Image courtesy of NASA. (`http://www.nasa.gov/pdf/678135main_rbsp_pk_final_hi.pdf`)

The ionosphere is commonly defined as the region above about 60 km altitude, where sufficient free electrons exist to influence the propagation of radio waves [Ratcliffe, 1972]. The ionosphere is formed primarily by ionisation of the neutral atmosphere. Its features and boundaries are complex due to collisions, recombination, and atmospheric chemistry. The existence of the ionosphere was initially postulated as a conducting layer that acted as a wave-guide for radio signals, to explain how transatlantic radio communication was possible [Kivelson & Russell, 1995]. This led to a technique known as ionospheric sounding, where short pulses of radio are transmitted upwards at different frequencies and the returning echo times are compared to the radio frequency. The critical frequency, below which radio signals will be reflected, is determined by the local refractive index which, in turn, is determined by the local electron density [Hargreaves, 1979]. This relationship allows ionospheric sounding to measure the vertical electron density profile based on the echo time, and hence altitude, at each radio frequency. These studies showed multiple discrete boundaries for different frequencies at different altitudes, which could be explained by vertical electron density variations. Figure 1.6 shows how the free electron density varies with altitude over several orders of magnitude and contains discrete transitions defining different layers labelled as D, E, and, F-regions.

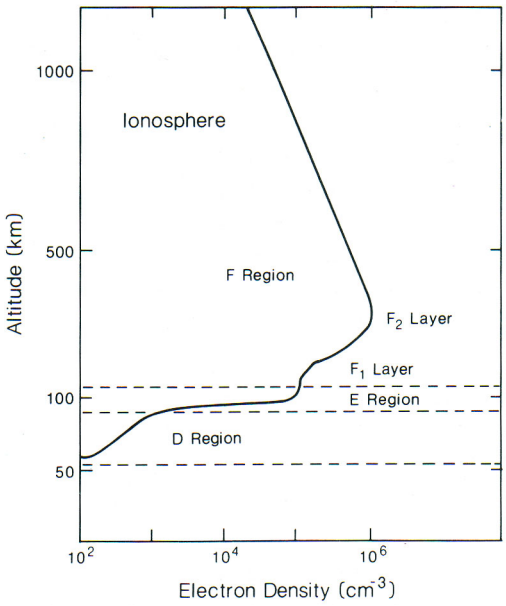

Figure 1.6: Electron density regions of the ionosphere at different altitudes. Taken from Kivelson & Russell [1995].

For a more detailed introduction to the magnetosphere and the ionosphere, the reader is directed to "Introduction to Space Physics" by Kivelson & Russell [1995].

1.3.3 Magnetometers for Solar System Exploration

The same physics responsible for the dynamics of the Earth's magnetosphere under solar wind forcing apply to a variety of other magnetised planets and moons in our solar system. Jupiter, Saturn, Neptune, Mercury and Uranus all have primary magnetic fields of various strengths and, as a result, have magnetospheres; however, the range of plasma parameters and scales can impact the response of the magnetised bodies to solar wind forcing. For example, neither Mars nor Earth's moon has a significant internal dipole field. However, Figure 1.7 shows a Martian example by Acuña et al. [1999] of how complex local magnetic fields can be present in the Martian crust. These crustal fields may form miniature magnetospheres near the surface [e.g., Halekas et al., 2008]. The dynamics of these solar wind-magnetosphere interactions, especially in the gas giants where planetary rotation can be an important factor, is still poorly understood. However, a comparative study of the response of these planetary magnetospheres offers a method to examine the relevant plasma physics over a range of relevant plasma parameters, such as incident Mach numbers and fluid, electron, and ion plasma scales and speeds.

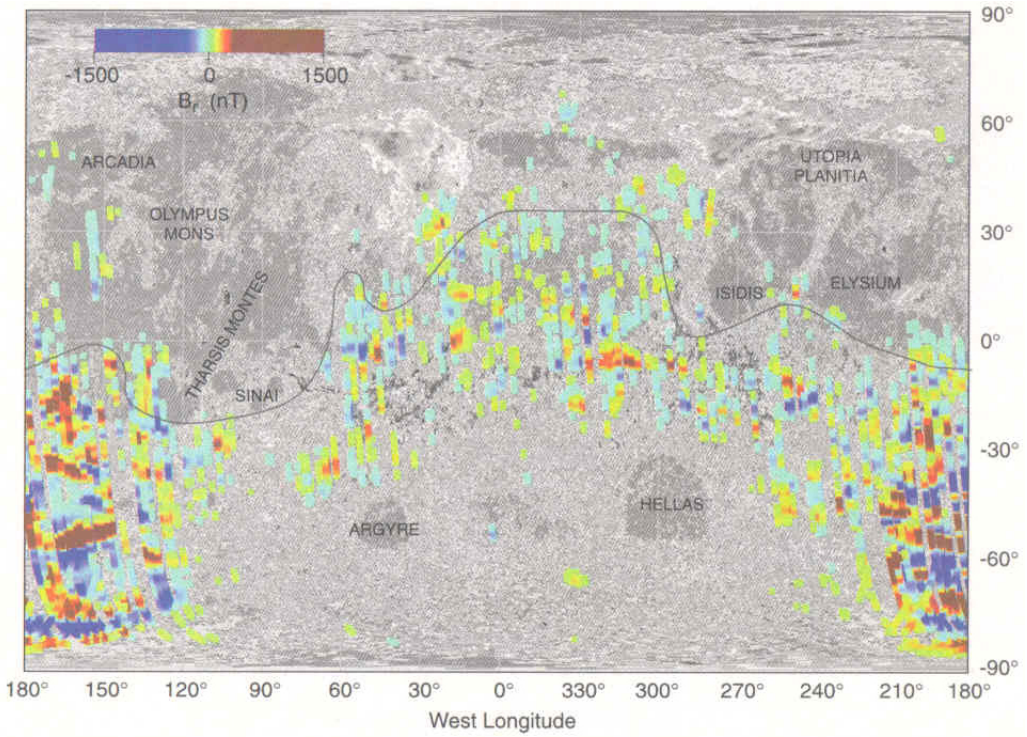

Figure 1.7: The crustal magnetic field of Mars superimposed on a image of the surface geography. The colour scheme corresponds to the radial magnetic field (B_r) measured by the Mars Global Surveyor magnetic field experiment/electron reflectometer (MAG/ER). Taken from Acuña et al. [1999].

Other potential science targets in our solar system for fluxgate measurements include: the dynamic evolution of the solar wind itself; the plasma physics at the terminator (night/day boundary) on the Earth's moon; and the structure of the termination shock, where the solar wind becomes subsonic as it approaches the heliopause at the edge of our solar system.

1.4 Magnetic Measurements and Space Physics Research

It is necessary to measure, model and interpret the shape, strength and dynamics of the Earth's magnetic field to understand the Earth's local space environment. Due to the size and complexity of the Earth's magnetosphere, magnetic measurements from a variety of locations are required to characterize its global features. Similarly, electromagnetic plasma waves play an important role in magnetospheric dynamics. Magnetic field measurements are therefore required for many of the fundamental research topics in space physics. Several examples are provided in this section to illustrate the need for space-based magnetometery.

1.4.1 Field Geometry and Features

The shape of the Earth's magnetic field and the direction of the IMF are fundamental measurements needed to understand the structure of the Earth's magnetosphere and its response to solar forcing. The shape of the field is related to how much energy has been stored in the deformation of the field from its basic dipole shape and to the rates of dayside and nightside magnetic reconnection.

1.4.2 Poynting Vector

Studies of energy transport in the magnetosphere must consider the local Poynting vector, $\mathbf{S}$ (units: $\mathrm{W/m^2}$), the energy per unit time per unit area being transported by the electromagnetic field

$$\mathbf{S} \equiv \frac{1}{\mu_0} \left(\mathbf{E} \times \mathbf{B} \right), \tag{1.1}$$

where μ_0 is the permeability (units: $\mathrm{N/A^2}$) of free space ($4\pi \times 10^{-7}$ $\mathrm{N/A^2}$). It is necessary to measure the electric field $\mathbf{E}$ (units: V/m) and the magnetic field $\mathbf{B}$ (units: T) to calculate the Poynting vector and quantify the (usually time dependent) electromagnetic energy transport.

Measurements of electromagnetic waves are also required to quantify the energy transported by perturbations in the electric ($\delta\mathbf{E}$) and magnetic ($\delta\mathbf{B}$) field via the wave Poynting vector.

1.4.3 Charged Particle Motion

The motion of charged particles in the magnetosphere is dictated by the local electric and magnetic fields. For example, particles will experience the total force $\mathbf{F}$ due to the combination of the Coulomb and Lorentz forces from their velocity $\mathbf{v}$, charge q, and the local electric field $\mathbf{E}$ and magnetic field $\mathbf{B}$.

$$\mathbf{F} = \mathrm{q}\mathbf{E} + (\mathrm{q}\mathbf{v} \times \mathbf{B}) \tag{1.2}$$

This leads to the three main charged particle motions in the magnetosphere shown in Figure 1.8. Charged particles can travel parallel to the magnetic field by spiralling in a 'gyro motion' around the field line with gyro-velocity $\mathbf{V_g}$. In a converging field such as the Earth's dipole field, the stronger magnetic field $\mathbf{B}$ at the Earth's poles can trap particles into 'bounce motion' with bounce-velocity $\mathbf{V_b}$. In an azimuthally symmetric field the trapped particles can, on average, move longitudinally in 'drift motion' with drift-velocity $\mathbf{V_d}$. Kivelson & Russell [1995] provide a more complete description of these effects.

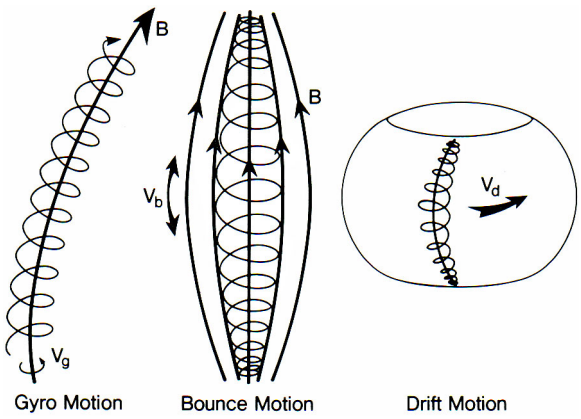

Figure 1.8: From left to right, gyro, bounce and drift single particle motion in a dipole magnetic field. Taken from Kivelson & Russell [1995].

In a dipole background magnetic field such as the Earth's, these periodic motions can combine to trap a charged particle into gyrating around a magnetic field line, bouncing between the poles, and drifting longitudinally. For example, such motion forms the basis of particle trapping in the toroidally shaped Van Allen radiation belts. Energetic particles can be monitored by using instruments that measure the energy deposited by each particle entering through an aperture. This allows the direction and speed of the particle to be determined. In general, the properties of the plasma are governed by the distribution function of the ensemble of ions and electrons. Since the motion of these charged particles is strongly controlled by the magnetic field, the orientation of **B** largely controls the structure of these particle distributions. In principle, the measured 3-D velocity distribution can sometimes provide information about the direction of **B** (e.g., in the presence of a depleted loss cone, Section 1.4.5), but no information about its magnitude; usually, **B** must be measured directly. Because the particle's path is controlled by the local magnetic field, the strength and direction of the magnetic field usually needs to be known to correctly infer the movement of charged particles.

1.4.4 Electromagnetic Waves

Magnetized plasmas can support a plethora of wave modes depending on factors such as the direction, shape, and strength of the electric and magnetic fields and the distributions of the constituent electrons and ions. The wave modes are also affected by the bulk properties and moments of the particle distributions relating to species, densities, temperatures, anisotropies, and average energies of the charged particles in the plasma. Under certain conditions, these electromagnetic waves can strongly interact with charged particles. For example, particles can exchange energy with waves in much the same way that a wave on the ocean interacts with a surfer. Electromagnetic waves can both transfer energy to charged particles and take energy from them. Under certain conditions, this can provide a mechanism to energise the magnetic waves by extracting energy from the particle distributions.

The electromagnetic waves of interest in most space physics applications have frequen-

cies in the range of millihertz to kilohertz (see Section 2 for a mission specific example). Generally, the lower frequency waves are measured using a fluxgate magnetometer while the higher frequency waves are measured using an induction coil magnetometer (in the literature, the terms searchcoil and induction coil are often used interchangeably). A review of these sensing techniques is provided in Chapter 3.

1.4.5 Particle Trapping and Pitch Angle

A charged particle moving in a magnetic field can be characterised by its 'pitch angle,' α, the angle of its velocity with respect to the magnetic field as shown in Figure 1.9.

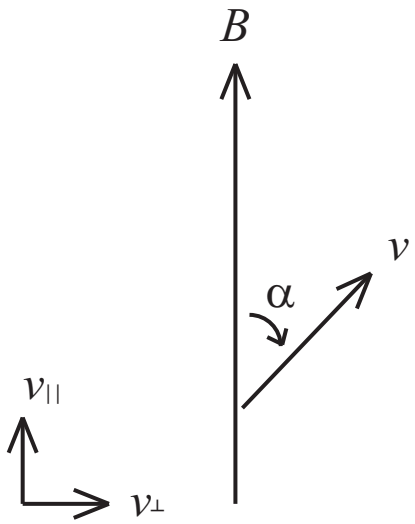

Figure 1.9: Pitch angle α of a charged particle moving through a magnetic field.

The particle's pitch angle α can be expressed as a function of the particle's velocity parallel and perpendicular to the magnetic field ($\mathbf{v}_{\parallel}$ and $\mathbf{v}_{\perp}$ respectively).

$$\tan\alpha = \frac{\mathbf{v}_{\perp}}{\mathbf{v}_{\parallel}} \tag{1.3}$$

Following the description by Walt [2005], as long as the magnetic field $\mathbf{B}$ changes slowly compared to the gyration frequency of the particle, the perpendicular momentum $\mathbf{p}_{\perp}$ and the magnetic field are linked by an approximate constant based on the magnetic moment of the particle known as the first adiabatic invariant, μ (Equation 1.4).

$$\mu = \frac{\mathbf{p}_{\perp}^2}{\mathbf{B}} = \frac{\mathbf{p}^2 sin^2\alpha}{\mathbf{B}} = \text{constant} \tag{1.4}$$

In the absence of an electric field, the particles momentum $\mathbf{p}$ is constant. As the particle follows a field line towards Earth, the strength of the magnetic field $\mathbf{B}$ increases and the particle's pitch angle α must increase to hold the first adiabatic invariant constant.

This creates a mirror point where the particle's pitch angle reaches 90^o and the particle has lost all parallel velocity. This is shown schematically in Figure 1.10.

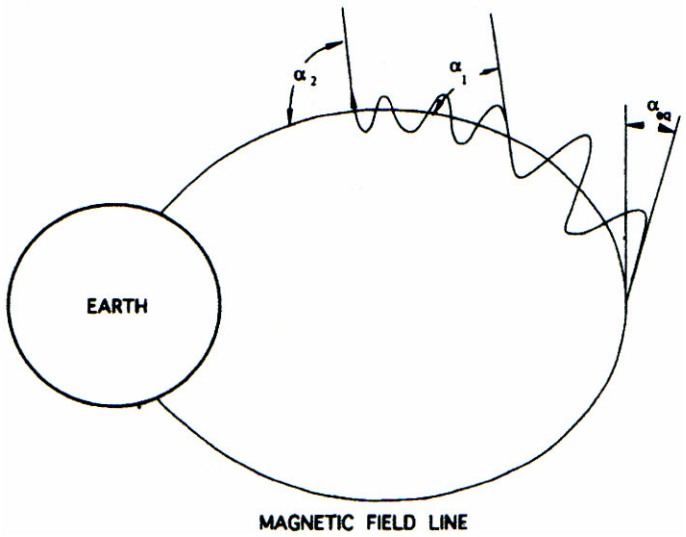

Figure 1.10: Pitch angle mirroring in the Earth's dipole field. As the particle follows a magnetic field line towards the Earth, **B** increases and the particle's pitch angle, α, increases to conserve the first adiabatic invariant ($\alpha_2 > \alpha_1 > \alpha_{eq}$). Taken from Walt [2005].

Therefore, at any location within the dipole field there is a minimum pitch angle α_{LC} after which a particle will travel close enough to the Earth to interact with the atmosphere and be lost. This 'loss cone' is defined by B, the local magnetic field strength, and B_a, the magnetic field at the top of the atmosphere ($\sim$100 km altitude).

$$\alpha_{\mathrm{LC}} = \sin^{-1}\sqrt{\frac{B}{B_a}} \tag{1.5}$$

Without a measurement of the magnetic field, **B**, it is impossible to determine whether a particle will be trapped in the magnetic field by pitch angle mirroring, or collide with the atmosphere and be absorbed and lost. This makes the magnetic field measurement essential to studies of geomagnetically trapped ions and electrons.

1.4.6 The Significance of Magnetic Measurements

The physical phenomena described above interact to produce complicated and intercoupled processes in space plasmas. Section 1.5 summarizes some of the high-level space physics science targets that will be pursued in the coming decades and demonstrates how they require measurements of the static magnetic field and low frequency magnetic waves. Fluxgate magnetometers are usually the preferred instrument for these types of measurements as they have no moving parts, are reliable and robust, can operate over a wide temperature range, and can be designed to have low noise, high accuracy and fine resolution. Induction coil (search coil) magnetometers often provide complementary

high-frequency measurements but cannot measure the static field and are inefficient at low frequencies.

1.5 Science Targets Requiring Fluxgate Measurements

Understanding many space physics phenomena requires experimental missions that (usually in combination) can span periods of at least one to two decades to characterise processes that vary over the approximately eleven year solar cycle. Addressing these types of problems requires sustained efforts from many institutions and agencies and overarching guidance from long-term strategies that cover these extended time periods. This section reviews some of the relevant guiding documents maintained by different international groups and demonstrates the need for fluxgate magnetometer measurements.

The Canadian GeoSpace Monitoring (CGSM) program (`http://cgsm.ca/doc/cgsm_sci_plan.pdf`) was formed to help understand the coupling between our planetary environment and the variability of our Sun. CGSM hopes to address the physical processes that influence space weather, climate, the radiation belts, and the aurora. CGSM is organised into five "grand challenges", which examine specific questions behind the transport of mass and energy through different scale sizes in our coupled solar-terrestrial system. Fluxgate measurements are required for these investigations to understand the movement of charged particles that transport mass and energy from the Sun to the Earth's magnetosphere.

International Living With a Star (ILWS) is a multinational collaboration between international space agencies with the mission to "Stimulate, strengthen, and coordinate space research to understand the governing processes of the connected Sun-Earth System as an integrated entity" (`http://ilwsonline.org`). The ILWS Steering Committee has representatives from the Canadian, Chinese, European, Japanese, US, and Russian space agencies. ILWS proposes to study the connected Sun-Earth system using coordinated solar-terrestrial space missions supported by theory, modelling and the open interchange of data. Fluxgate measurements will play a principal role in understanding the magnetic fields, that connect and control the Sun-Earth system.

The National Aeronautics and Space Administration (NASA) Heliophysics Roadmap (`http://sec.gsfc.nasa.gov/2009_Roadmap.pdf`), last updated in 2009, is NASA's recommended plan for 2009 to 2030 for science and technology to study the Sun and the region dominated by the Sun's output (the heliosphere). The roadmap sets out three fundamental questions:

- "What causes the Sun to vary?"
- "How do the Earth and the Heliosphere respond?"
- "What are the impacts on humanity?"

Understanding how the variations of the Sun's output impact the Earth and the heliosphere will require fluxgate measurements of the underlying magnetic field dynamics that couples these systems.

Space Situational Awareness (SSA) is an undertaking of the European Space Agency (ESA) to provide "comprehensive knowledge, understanding, and maintained awareness as far as the population of space objects in orbits, space environment, and existing threats/risks are concerned" [Bobrinsky & Monte, 2010]. This mandate is divided into three main segments: space surveillance and tracking, space weather, and near-earth objects. The space weather segment identifies both space and ground measurements of the Earth's geomagnetic field as principal inputs and data products to be delivered. Canada, as the only associated member of the ESA, is eligible in addition to European nations to bid to provide a space-ready fluxgate instrument to ESA programs in which it is participating.

Fluxgate magnetometer measurements are required to achieve the goals in each of the guiding documents described above. This demonstrates the ongoing need for spaceflight ready fluxgate magnetometers and indicates that such instruments will continue to be required in the coming decades.

1.6 Planned Missions With Fluxgate Instruments

Fluxgate magnetometers have been identified as required payload instruments on a variety of future space science missions where static field and low frequency magnetic wave measurements are needed. A selection of these applications, including both Canadian led missions and international flights of opportunity, are outlined below.

ORBITALS was designed as an infrastructure contribution to the ILWS program described in Section 1.5. The mission was planned as a CSA small satellite mission with approximately half the science instruments provided by a NASA payload called the Mission of Opportunity, Radbelt Explorer (MORE). Unfortunately, despite being highly rated for both scientific merit and technical feasibility, the mission development was suspended in 2011 due to budget constraints. The ORBITALS mission, data requirements, and operational constraints are described in more detail in Chapter 2. Interested readers are referred to the original mission concept paper by Mann et al. [2006]. The FGM design developments described in this thesis were primarily developed for the application of the CSA's ORBITALS mission.

The proposed CSA PCW mission is designed to provide operational telecommunication and imaging services to northern Canada. PCW uses two satellites in a highly inclined and highly elliptical (Molniya type) orbit which dwells over Canadian territory during apogee. This orbit also traverses many of the significant regions of the Earth's magnetosphere (though the primary requirements for the orbit were not specifically designed to enable this). PCW will provide daily passes through the radiation belts and will spend much of its orbit hanging at high altitudes providing coverage, for example, of the understudied funnel shaped regions over the poles (called the cusp) where the Earth's magnetic field opens to space (Figure 1.11). The FGM is proposed as part of a secondary science instrument package on PCW called PRIMO (see Mann et al. [2011]).

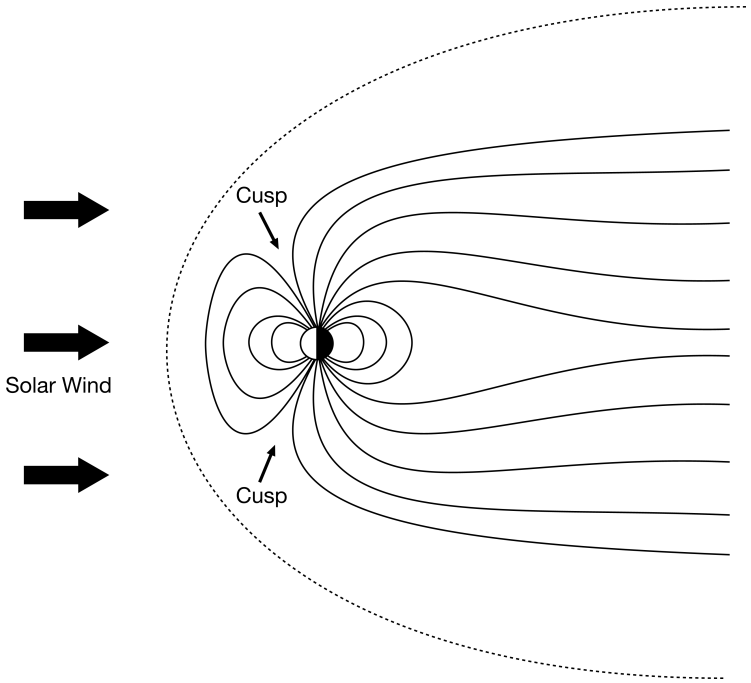

Figure 1.11: The cusp region of the Earth's magnetic field. Image credit Andy Kale.

In 2011, a team from the UAlberta was offered a no-cost launch in December 2013 for the instrument described in this thesis on the fourth Norwegian Investigation of Cusp Irregularities (ICI) sounding rocket, which will fly to an altitude of 350 km, to study the plasma processes that control space weather in polar regions. Although ICI-4 is designed to study irregularities in electron density and their interference with telecommunication, its comprehensive plasma package could be used for a variety of other applications. For example, the rocket will allow for investigations into the potential role of electromagnetic Alfvén waves in accelerating the electrons that cause the aurora. Keiling et al. [2003] used measurements from the Polar spacecraft to show that, on average, the net wave Poynting vector into the auroral oval carries enough energy to power the aurora acceleration process. However, the potential coupling between the Alfvén waves and auroral electrons is not yet fully understood.

Canadian fluxgate magnetometer payloads have also been proposed for:

- The proposed CSA Ionospheric Space Weather Effects in the Auroral Thermosphere (I-SWEAT) mission [Yau et al., 2008] to study anomalous satellite drags during magnetic storms and substorms;
- The Japan Aerospace Exploration Agency (JAXA)/CSA cross Scale COupling in Plasma universE (SCOPE) mission by Fujimoto et al. [2009] to distinguish between temporal and spatial variations in the magnetosphere using a microsatellite constellation; and
- The ESA Eidoscope addition to SCOPE by Vaivads et al. [2011] to study particle acceleration at plasma boundaries.

These projects demonstrate the ongoing demand for spaceflight ready fluxgate magnetometers such as the FGM developed in this thesis to provide data for space physics experiments.

Chapter 2

Satellite Measurements of the Earth's Magnetosphere

The FGM described in this thesis was primarily designed for flight on the proposed CSA ORBITALS small satellite mission. The ORBITALS mission concept was first published by Mann et al. [2006]. The FGM instrument development started during Phase A of the mission and was continued during a twelve month "Phase A2" risk reduction period. The ORBITALS mission was suspended in 2011. However, the FGM instrument development continued as part of its consideration as part of a secondary science payload called PRIMO on the CSA's PCW satellite mission. For the purposes of this thesis, the ORBITALS mission will be considered as the target application, but the design is applicable to most space physics missions requiring radiation hard fluxgate magnetometer instrumentation.

2.1 Representative Mission: CSA ORBITALS

The ORBITALS mission was a proposed Canadian small satellite science mission to investigate the Earth's radiation belts (shown schematically as Figure 2.1) as a Canadian contribution to the ILWS program. ORBITALS development was funded by the CSA and led by UAlberta with Magellan Aerospace Ltd. as the primary industrial partner. This Canadian small satellite would carry a full suite of plasma instruments to monitor ion and electron populations, the local magnetic and electric field, and the resulting space weather effects. In addition to its own science objectives, ORBITALS would complement the US RBSP constellation. Fundamentally, ORBITALS was intended to investigate how the radiation belts can suddenly and efficiently accelerate low energy ions and electrons to form damaging, high energy space radiation, transport them within the magnetosphere, and then drain them into the atmosphere.

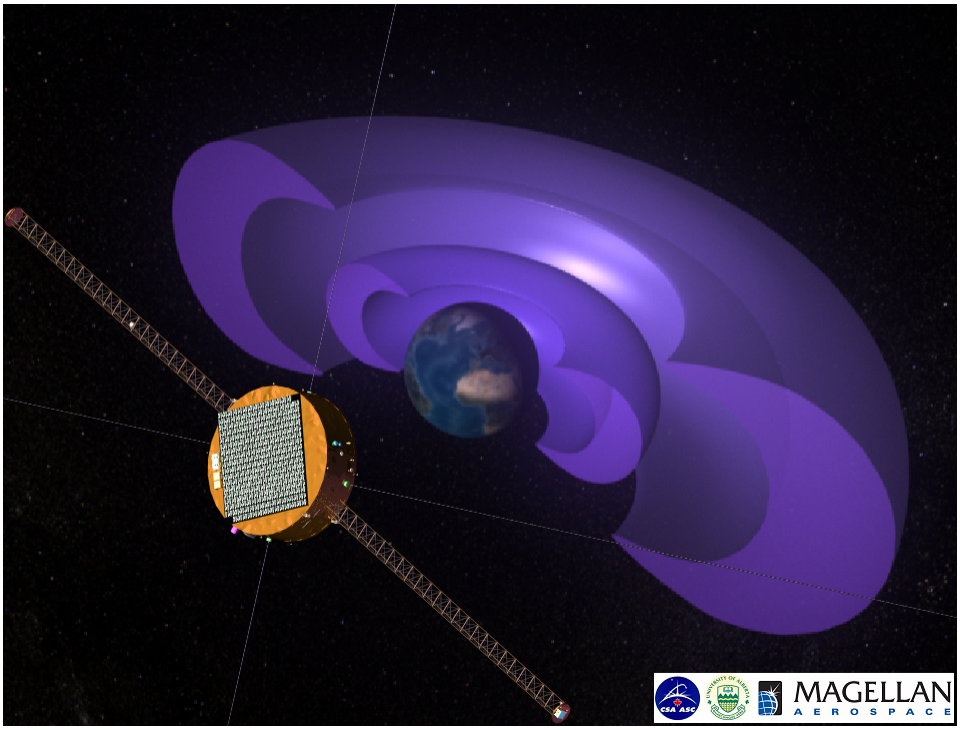

Figure 2.1: Schematic representation of the ORBITALS Spacecraft. Image credit Magellan Aerospace Ltd.

2.1.1 Mission Science Overview

ORBITALS' primary science objective was to "Understand the dynamical variation of outer radiation belt electron flux, including determining the dominant acceleration and loss processes." The best currently available data for this purpose is from the Combined Release and Radiation Effects Satellite (CRRES) mission. Figure 2.2 shows how the flux of energetic electrons can suddenly increase by four orders of magnitude. ORBITALS was designed to dwell within the radiation belts making in-situ plasma measurements to understand the processes responsible for this type of sudden energisation of the plasma and similarly to determine how the plasma decays into a quieter, lower energy state.

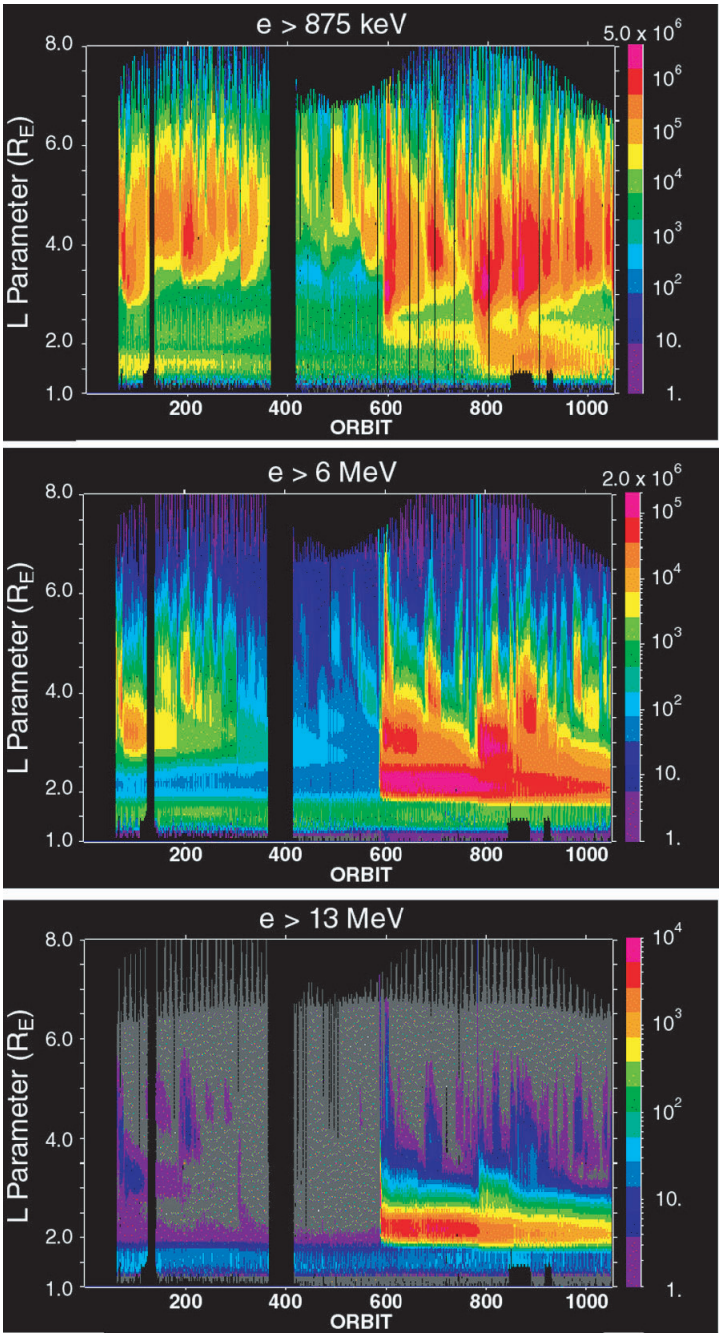

Figure 2.2: Dynamics of the radiation belts in three energy ranges as measured on each orbit of the CRRES mission. Taken from Mann et al. [2006].

One of the candidate mechanisms for electron acceleration is the resonant interaction of low energy electrons with electromagnetic waves. High precision magnetic field measurements are required to estimate the background field to both interpret particle data and to characterise the magnetic waves superimposed on this background field. ORBITALS also had several secondary and tertiary science and space weather objectives which are not discussed in detail in this thesis.

2.1.2 Orbit Parameters

The ORBITALS mission considered several orbits based on criteria including: maximising the time spent within the radiation belts, repeating ground-tracks magnetically conjugate to ground instrumentation, and the cost, complexity and logistics of achieving the orbit. Four candidate orbits are shown in Table 2.1. In all cases the orbit epoch (time of insertion into the orbit) is assumed to be 1/1/2013 12:00 Coordinated Universal Time (UTC) and the Right Ascension of the Ascending Node (RAAN) is constant at 270^o.

	Potential Orbits			
Parameters	"Raised Perigee"	"5 per 2"	"5 per 2"	"7 per 3"
Apogee Altitude (km,R_E)	33743,6.3	32835,6.1	32435,6.1	35950,6.6
Perigee Altitude (km,R_E)	6627,2.04	375,1.06	750,1.12	250,1.04
Semi-Major (km)	26563	22983	22970.5	24478
Eccentricity	0.51041	0.70617	0.68969	0.72923
Inclination (^{o})	7	7	7	7
Arg. of Perigee (^{o})	0	0	0	0
RAAN (^{o})	270	270	270	270
True Anomaly (^{o})	0	0	0	0
Period (hrs)	11.96	9.63	9.62	10.58
Orbits / Day	2 per 1	5 per 2	5 per 2	7 per 3

Table 2.1: Potential mission orbits and their parameters.

From the perspective of a magnetic field instrument, the most significant impact of the orbit selection is the altitude of the perigee. Since the strength of the Earth's magnetic field decreases with distance as $1/r^3$, lower altitude perigees have a significantly stronger maximum magnetic field amplitude. Magnetic field amplitude will also vary with orbit inclination; however, for the all the candidate orbits, the inclination was fixed at 7^o. Although the "Raised Perigee" orbit is the scientifically preferred option, the prototype fluxgate is designed to be compatible with all four orbit options.

2.1.3 Instrument Payload

The ORBITALS instrument suite is made up of four Canadian science instruments, four US science instruments named the MORE payload and two space weather instruments built by Canadian industry. The complete suite of instruments is designed to characterize the local plasma environment and measure the associate space weather effects. The complete ORBITALS payload is composed of:

Searchcoil Magnetometer (SCM): measures the three axis dynamic magnetic field via the induction coil method (UAlberta and COMDEV);

Fluxgate Magnetometer (FGM): measures the three axis static and low frequency AC magnetic field (UAlberta, Bennest Enterprises Ltd., Narod Geophysics Ltd. and COMDEV). This instrument is the topic of this thesis;

High Energy Proton Telescope (HEPT): measures MeV protons and potentially MeV electrons (UAlberta and COMDEV);

Plasmaspheric Ion Imager (PII): measures cold plasma ion species (University of Calgary and COMDEV);

Energetic Electron Proton Spectrometer (EEPS): measures medium energy electrons and protons (US MORE Payload - Aerospace Corporation);

Electric Fields and Waves (EFW): measures the two dimensional electric field in the spacecraft spin plane (US MORE Payload - University of Minnesota);

Relativistic Electron Proton Telescope (REPT): measures high energy MeV electrons and protons (US MORE Payload - University of Colorado);

COmposition and DIstribution Function (CODIF): measures the three dimensional distributions of the major species of low energy ions. The physical instrument is the flight spare from the Cluster satellite mission (US MORE Payload - University of New Hampshire);

Radiation Environment Monitor (REM): monitors radiation induced single event upsets in semiconductor memory cells and total accumulated radiation dose (Space Weather Instrument - Best Medical Canada Inc); and

Dielectric Deep Charge Monitor (DDCM): monitors charge accumulated on an isolated dielectric due to radiation (Space Weather Instrument - DPL Science Inc).

2.1.4 Spacecraft Overview

The ORBITALS spacecraft was designed by Magellan Aerospace Ltd. under contract to the CSA. The majority of the technical details of the spacecraft are proprietary and will not be described here. However, the spacecraft is described at a high level to illustrate how it constrains the FGM payload. Figure 2.3 shows the two magnetometer booms and four long wire booms for the electric field instrument on the ORBITALS spacecraft.

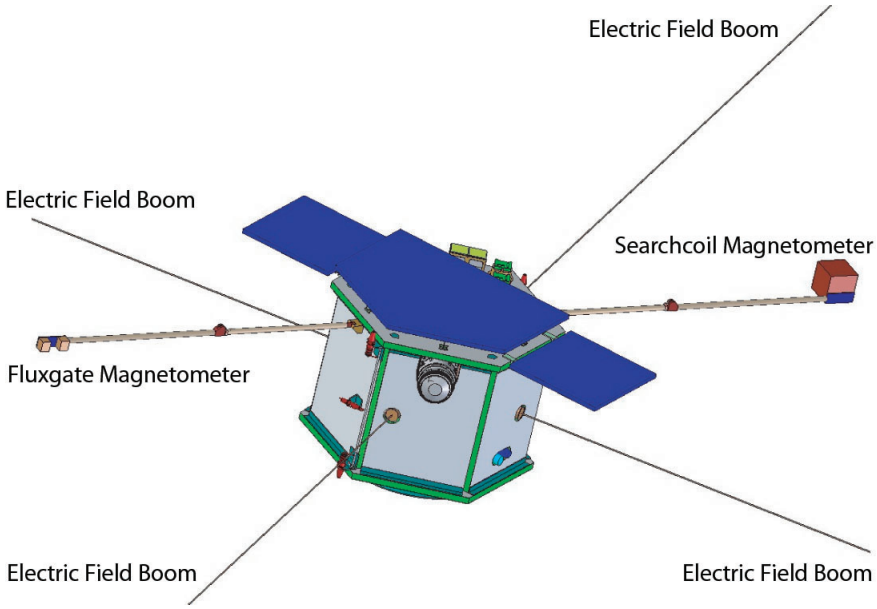

Figure 2.3: Major features of the ORBITALS spacecraft. Image credit Magellan Aerospace Ltd.

ORBITALS measures the local electric field by measuring the potential between two spherical conductors that are electrically coupled to the local plasma. The probes need to be separated by ∼80 metres to move the probes away from the electromagnetic noise of the spacecraft and to create a measurable potential difference because the gradients in the electric field in space are small (0.1 to 400 mV/m). This large probe separation is realized using wire booms, which are held in position using centrifugal force by spinning the satellite. A spinning platform also has advantages for particles instruments because a fixed, finite look direction can sweep out 360^o of coverage each spin.

The ORBITALS spacecraft is expected to produce significant electric and magnetic noise from the solar panels, battery charge and discharge currents, the spacecraft electronics, and the other instruments. Early estimates suggested that the FGM would need to be several meters from the spacecraft for the spacecraft's magnetic noise to reach acceptably low levels. Two fluxgate sensors will be mounted at different lengths along a boom to physically separate the instruments from these noise sources. This presents some mechanical challenges, but, more importantly, means that the sensor must be outside the spacecraft body and will experience a more extreme thermal environment. The instrument electronics and their aluminium housing are too heavy to be deployed on the boom and will therefore be mounted within the spacecraft. This requires that the fluxgate accommodate about three meters of cabling between the electronics and the sensor head.

Overall, the ORBITALS spacecraft is a modification of the standard Bristol aerospace small-satellite bus. This type of spacecraft has limited volume available for payloads and therefore the FGM volume envelope is constrained to ∼2250 cm^3. The size of the spacecraft also limits the amount of surface area available for solar panels and hence the available power. The total FGM power budget will therefore be limited to less than

5 Watts. Finally, the spacecraft has a finite mass limit to allow the desired orbit to be obtained using a low-cost launcher. This leads to a mass limit for the instrument, including radiation shielding, of about 5 kilograms.

The ORBITALS spacecraft is a mass, power and volume constrained measurement platform, which presents significant challenges to instrument design. The specific constraints imposed on the instrument design will be further developed and quantified in Section 2.3.

2.2 Relevant Mission Data Requirements

The ORBITALS Mission Requirements Document (MRD) by Mann et al. [2009] is the official document of record for the science requirements of the mission. The most significant requirements for the FGM are described below.

2.2.1 Magnetic Field Measurements as a Primary Data Product

The magnetic field data from the FGM has multiple uses that impose a variety of requirements on the instrument.

The FGM must be capable of operating over the entire range of magnetic field strengths experienced by the spacecraft. The magnitude of the field varies with distance from the Earth and is therefore different for each of the potential orbit options. The potential magnitude of the field is described in Section 2.3.1. However, in practice, it is highly desirable that the instrument tolerate the much larger field at the Earth's surface so that the instrument can be developed, tested and calibrated without always requiring a magnetic shield to limit the ambient field strength. This leads to an instrument range of about ±60,000 nT.

The potential frequencies of magnetic waves in the ORBITALS orbit were examined during Phase A2. The parameters of these waves are linked to underlying plasma parameters, which depend on local conditions such as the strength of the magnetic field and the density and temperature of the plasma. Figure 2.4 shows the expected frequencies of possible waves modes as a function of distance from Earth.

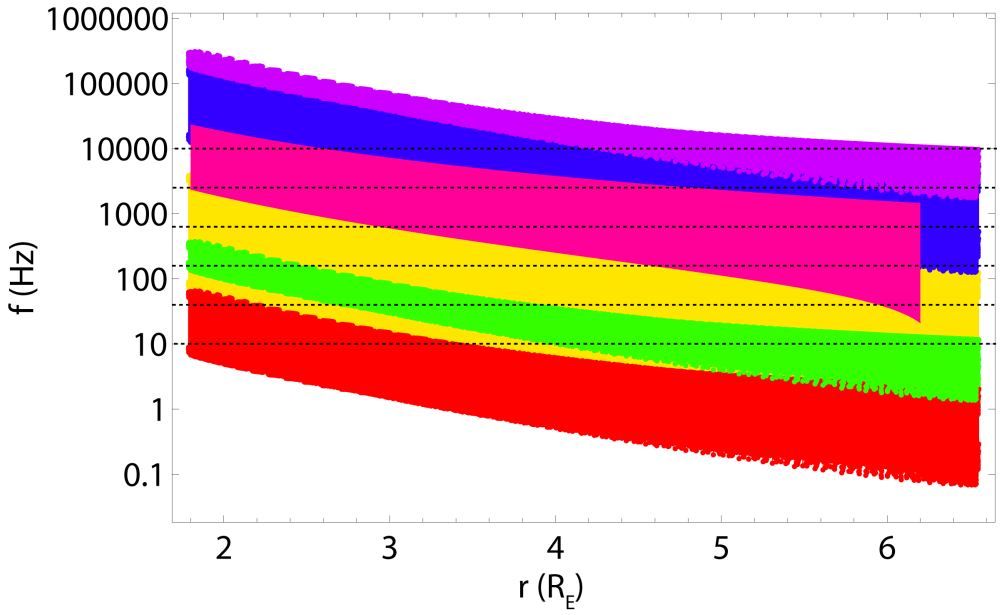

Figure 2.4: Potential wave frequencies (f) at different distances (r) from the Earth (1 Re = 1 Earth radius). Electromagnetic Ion Cyclotron (Red), Fast Magnetosonic / Lower Hybrid (Yellow), Whistler Mode (Blue), Electron Cyclotron Harmonic (Purple), Ion Cyclotron Harmonic (Green), Ion-Acoustic (Pink). Taken from [Rae et al., 2011].

The potential frequencies of interest for the ORBITALS mission therefore span from the millihertz range to several hundred kilohertz. This range of frequencies cannot reasonably be achieved by a single instrument, so the low frequency measurements from the FGM and the high frequency measurements from the SCM will together span this range.

Milling et al. [2011] showed that the sensitivity of the SCM drops below about 10 Hz but may be usable to about 1 Hz. The FGM should therefore operate up to at least 10 Hz to provide a decade of overlap with the SCM for in-flight cross-calibration.

The expected frequencies and amplitudes based on previously observed waves were assessed by project scientist Jonathan Rae. The results [I. J. Rae, Personal Communication, 2011] are summarised in Table 2.2.

Wavemode	Frequency (Hz)	Amplitude (nT pp)	Reference
EMIC	< 2	20	[Usanova et al., 2008]
Magnetosonic	0.1 - 1	50 - 400	[Liu et al., 2011]
Whistler/Chorus	100 - 10,000	0.01 - 0.1	[Li et al., 2009]
Large Amplitude Whistler	$< 4{,}000$	< 10 nT	[Wilson et al., 2011]

Table 2.2: Wave amplitudes from previous missions. EMIC refers to Electromagnetic Ion Cyclotron waves. [I. J. Rae, Personal Communication, 2011]

This review indicates that the previously observed Electromagnetic Ion Cyclotron (EMIC) waves have peak to peak amplitudes on the order of 1-10 nT in the ~Hz frequency range, which can be measured by the FGM. Long period Ultra Low Fre-

quency (ULF) waves typically have larger amplitudes. Whistler, Chorus, and Large Amplitude Whistler Mode are above the frequency range covered by the FGM. A worst case resolution of 0.1 nT would set the minimum signal to noise ratio for these types of waves to about ten to one. However, finer resolution is desirable and should be pursued if technically feasible.

2.2.2 Magnetic Field Data as a Supporting Data Product

Particle measurements made by other instruments need to be evaluated in terms of their pitch angle (see Section 1.4.5) with respect to the background magnetic field direction to determine if they are trapped in the radiation belts, or if they will precipitate into the atmosphere.

This measurement is complicated by the rotation of the spacecraft with respect to the background field. The particle data will be integrated continuously into into 10^o wide 'spin sector' bins with respect to the magnetic field. The principal investigators for the particle instruments have asked for the magnetic field to be sampled at least ten times in each spin sector at the nominal fifteen second satellite spin rate in order for the magnetic field to be a negligible error source. This leads to a requirement for the minimum magnetic field measurement cadence of:

$$\text{Sampling Rate (samples/s)} = \frac{10 \text{ samples}}{\left(15 \text{ s} \cdot \frac{10^o}{360^o}\right)} = 24 \text{ (samples/s)} \tag{2.1}$$

The particle instruments can measure particle energy with an accuracy in the range of 10 to 30%. The magnetic field accuracy should be about a factor of 100 below this value, or about 0.1%, for it to be a negligible error source.

The Poynting vector (see Section 1.4.2) is a composite data product derived from the FGM and the EFW instruments. This data product is degraded if the electric and magnetic measurements are not taken contemporaneously. This leads to a minimum requirement for the electric and magnetic fields to be sampled synchronously within 0.2 milliseconds with a goal of 40 microseconds (near the accuracy limit of the expected GPS time).

2.2.3 Summary of Data Requirements

The measurement requirements for the ORBITALS FGM are formally captured in the Instrument Specification Document by Milling et al. [2009]. The principle requirements have been reproduced here but have been reformatted and edited for ease of reading:

Measurement Resolution: The FGM payload shall measure each magnetic field sample to a resolution of at least 0.1 nT;

Cadence: The FGM payload shall measure the 3-D vector magnetic field with a cadence of at least 32 samples per second;

AC Range: The FGM payload shall measure the AC 3-D vector magnetic field up to a frequency of at least 10 Hz;

Maximum Noise: The FGM payload shall have a maximum equivalent magnetic field noise of 20 pT/$\sqrt{\text{Hz}}$ at 1 Hz. (this requirement was originally 100 pT/$\sqrt{\text{Hz}}$ for ORBITALS and was subsequently made more stringent);

Phase Response: The FGM payload shall have a phase response that is well behaved and constrained to -180 to +180 degrees up to the maximum frequency of 10 Hz;

Measurement Accuracy: The FGM payload shall measure the magnetic field on three axes with an accuracy of at least 0.1%;

Timing Accuracy: The absolute timing accuracy of the FGM payload shall be less than 40 microseconds;

FGM - EFW Relative Timing: The FGM shall be capable of returning high resolution time series data sampled at times relative to that of the EFW electric field samples, within a relative timing of less than 0.2 milliseconds with respect to the one pulse per second reference; and

FGM - EFW Relative Timing Target: The FGM should be capable of returning high resolution time series data sampled at times relative to that of the EFW electric field samples, within a relative timing of less than 40 microseconds with respect to the one pulse per second reference.

2.3 Key Constraints Imposed by the Mission, Platform, and Environment

The ORBITALS mission presents several challenges and constraints. The highly elliptical orbit travels through large and small magnetic fields, spends considerable time in the radiation belts and the instrument alternates between being warmed by the Sun and cooling rapidly when eclipsed by the Earth. The satellite has constrained mass, power, and volume, and must meet stringent reliability requirements. This section describes the principal constraints of the mission and quantifies them into verifiable requirements.

2.3.1 Magnetic Field Strength

One of the most significant constraints imposed by the mission is the maximum magnetic field strength expected in the orbit. Figure 2.5 shows how the magnetic field strength experienced in the "Raised Perigee" orbit varies between greater than 6000 nT near perigee and less than 500 nT near apogee.

The two curves shown in Figure 2.5 result from two 12-hour orbital periods and the tilt of the Earth's magnetic dipole with respect to the Earth's spin axis for the raised perigee orbit option from Table 2.1.

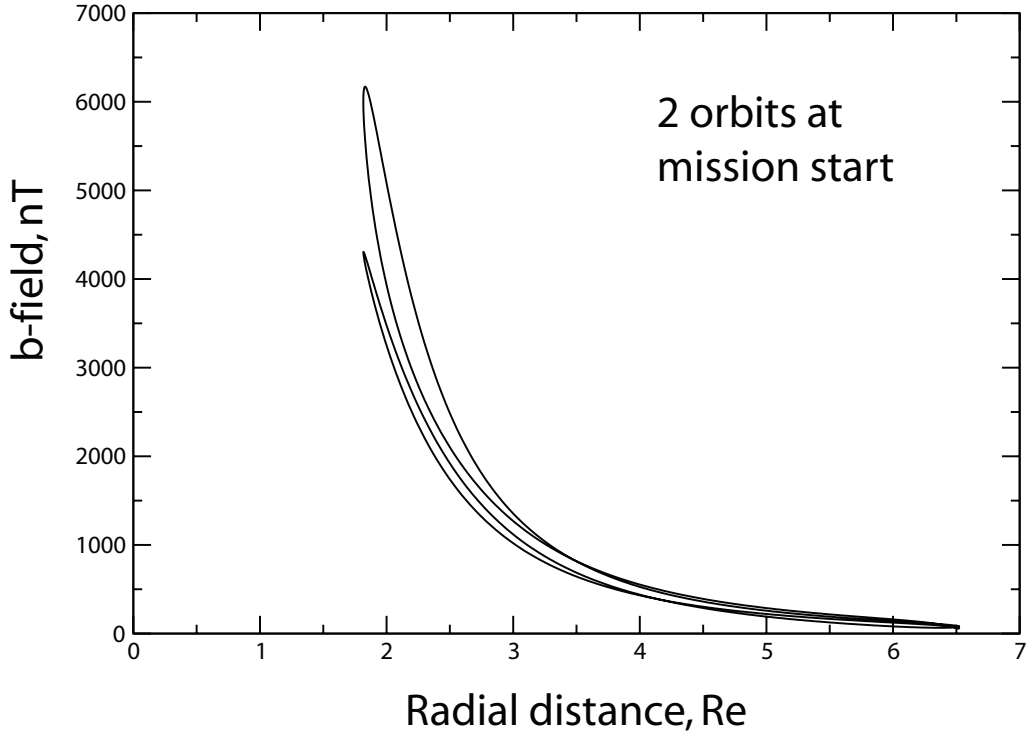

Figure 2.5: Local magnetic field strength over two raised perigee orbits. Taken from Ozeke & Mann [2011].

2.3.2 Magnetic Signal from a Spinning Spacecraft

Spinning the spacecraft, as required by the EFW instrument, has serious implications for magnetometer design because, in the frame of an instrument mounted on the spacecraft, the local magnetic field will appear to be spinning. This large dynamic field presents a very different technical challenge than measuring the quasi-static field found on the Earth's surface or on a three axis stabilized spacecraft. The magnetometer can never reach a steady-state value since the instrument will see at least two vector components vary by up to twice the magnetic field amplitude as the instrument spins through the background magnetic field. ORBITALS has a minimum spin period of 10 seconds which, in a static field of amplitude B_{max} translates to a worst-case $\frac{dB}{dt}$ slew rate of approximately

$$\frac{2 \cdot B_{max}}{t_{spin}} = \frac{2 \cdot 7000 \text{ nT}}{10 \text{ s}} = 1400 \text{ nT/s} \tag{2.2}$$

This spacecraft induced spin signal also poses problems for interpretation of magnetic field data. To a first examination, the spin signal should be expected to be sinusoidal and relatively easy to remove in post-processing. In practice, the spin period will be affected by subtle changes in spacecraft geometry due to heating and cooling. This effect is most prominent as the spacecraft enters and exits eclipse, and is compounded

by the tendency of the magnetometer booms to oscillate in response to changes in the spin frequency.

Figure 2.6 shows the an example of raw magnetometer data from the Time History of Events and Macroscale Interactions during Substorms (THEMIS) mission (green), which appears as an envelope function; the spin corrected data product is shown in red. This figure illustrates the challenge of removing the induced spin signal even during nominal conditions. Spin removal become even more complex when the spacecraft enters or exits eclipse, as the resulting temperature change can effects boom geometry, thus causing changes in spin rate.

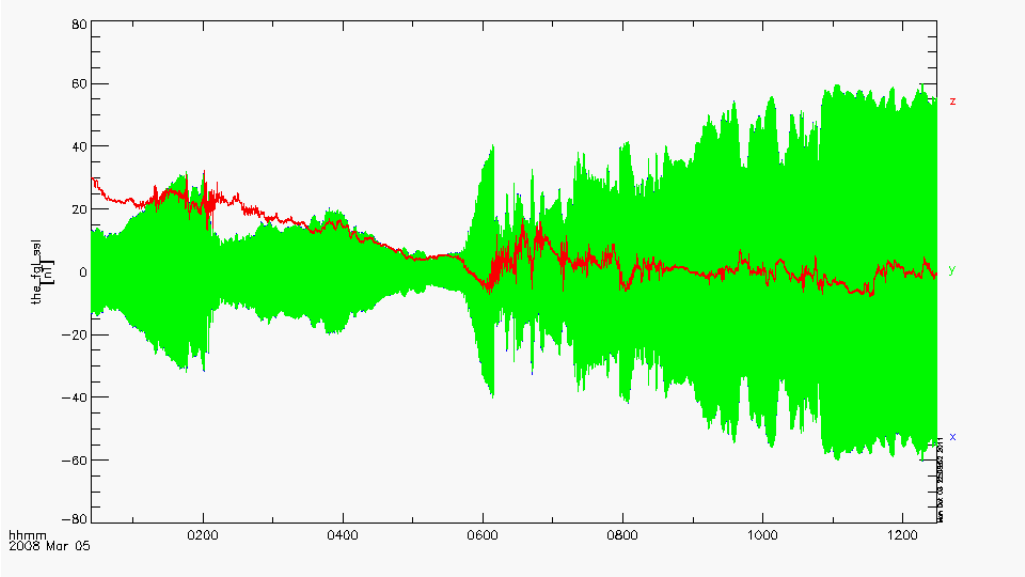

Figure 2.6: Example spin-tone contaminated magnetic data from THEMIS. Green shows the raw data and red shows the spin-corrected data. [From I. J. Rae, Personal Communication, 2011]

2.3.3 Radiation Environment

The radiation environment poses three main challenges to instrument design and each is mitigated in a slightly different way (see McClure et al. [2011]). The three principal effects and their mitigation are discussed briefly below to show how they influence instrument design.

2.3.3.1 Total Integrated Dose

Total Integrated Dose (TID) is a measure of total radiation exposure from all sources and is typically measured in units of krad. 1 rad is the dose required for 100 ergs of energy to be absorbed by one gram of matter. For comparison, 1 rad of radiation is converted to the medical dose of 1 rem by a quality factor that accounts for radiation source and type of absorber. In electronics, the quality factor is less important and the rad unit is generally effective in predicting component failure.

TID is generally mitigated in two ways. Shielding is used to reduce the total dose experienced by the instrument, and components are selected that use design techniques and materials that are resistant to TID. Space grade electronics are often guaranteed to some TID level between 10 and 300 krad. Care must be taken to check whether this guarantee relates to parametric or functional failure. Parametric failure is measured when any one of a list of vendor guaranteed specification is violated (for example, when an amplifier exceeds a noise specification). Functional failure occurs when the part no longer fulfils is primary purpose (for example when an amplifier no longer provides any amplification). Parametric failure is a much more useful criteria, as most components becomes useless to an instrument well before they functionally fail.

Radiation shielding is essential to stop the bulk of the environmental radiation. However, it can generally only reduce, rather than eliminate, the TID. Figure 2.7 shows the effect of different thickness of aluminium shielding on the expected TID for the ORBITALS mission in the raised apogee orbit.

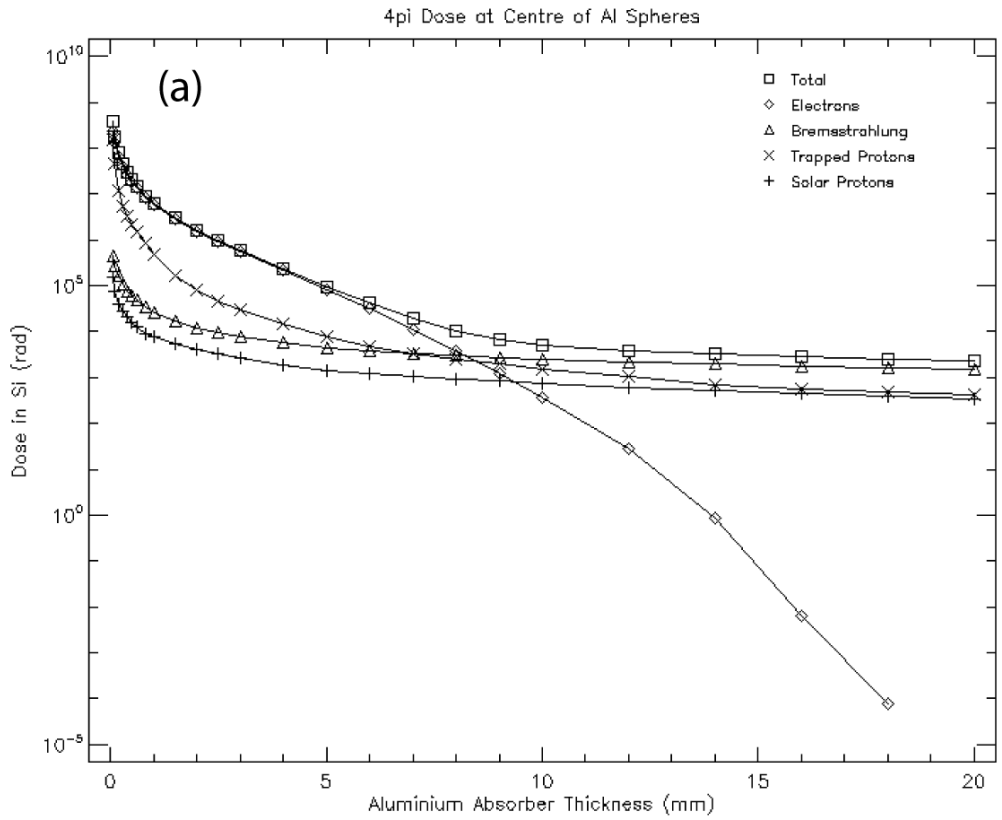

Figure 2.7: Shielding thickness and radiation total integrated dose. Taken from Ozeke & Mann [2011].

The plot shows that the first two millimetres of aluminium shielding are very effective at reducing the dose but subsequent shielding provides sharply diminishing returns. The dose due to electrons is effectively reduced at sufficient thickness. However, Bremsstrahlung X-rays and protons penetrate the shielding efficiently and quickly become the limiting factor in the TID above 7 mm of Al.

ORBITALS set two minimum requirements for TID mitigation. All electronics must be shielded by a minimum of 8 mm of Al (1 mm is provided by the spacecraft shell and 7 mm must be provided by an instrument's electronics box). All electronic components are required to have a minimum radiation tolerance of 100 krad. The 8 mm of Al requirement coincides with the inflection point in the total dose versus absorber thickness dependence. It also a pragmatic choice beyond which the mass of shielding required becomes infeasibly large. The 100 krad minimum tolerance is also a legal issue, as tolerances above 100 krad can be very difficult to procure in Canada due to the US International Traffic in Arms Regulations (ITAR) program.

A significant complication to TID screening is that the TID failure dose for some devices built using the classical bipolar transistor technology can vary by orders of magnitude depending on the dose rate. This effect is called Enhanced Low Dose Rate Sensitivity (ELDRS) and results from the way in which radiation hardened devices are tested. On a satellite, most components accumulate their radiation dose over years or decades. However, during radiation testing, the radiation dose is usually delivered over minutes, hours, or days. For field effect transistor processes, the dose rate has virtually no effect on the TID failure point. However, some traditional bipolar transistor components can survive up to 100 krad at high dose rates but fail at less than 10 krad at low dose rates.

Alternative testing mechanisms, annealing processes and accelerated testing procedures are a topic of ongoing research. However, many manufactures now screen bipolar components for ELDRS effects by testing some components at much lower dose rates. For the FGM, components built on bipolar processes were first screened for 100 krad tolerance and, where available, for ELDRS test results.

2.3.3.2 Single Event Upsets

Single event effects are transient phenomena resulting from the impact of individual highly energetic particles. In general, an individual ion or electron passes through a semiconductor creating an ionisation track (often by a strong, short-range coulomb interaction) of free charge carriers. These free charge carriers can occur in locations that were not engineered to hold charge and can temporarily force transistors into or out of conduction. These charge carriers will recombine away rapidly but may cause multiple types of effects:

Single Event Transient is a momentary change of state such as a sudden swing of an analog line or a transient on a digital line. This normally manifests as noise but may become a single event upset if the transient is transferred into a storage element like a memory cell or a latch;

Single Event Upset occurs when the transient charge changes the state of a gate. For example, a single event could toggle a individual memory cell. This allows the transient to be preserved even when the transient charge dissipates;

Single Event Latchup occurs when the transient charge carriers force a transistor (often an unintentional parasitic transistor) into a high-current state that becomes

self-sustaining. This may or may not cause long-term damage and generally requires power cycling to escape the latched state;

Single Event Rupture occurs when a single particle creates a permanent conduction path through the oxide insulator in a field effect transistor;

Single Event Burnout Occurs when a single event latchup causes sufficiently high current flow to destroy a component; and

Multiple Bit Upsets occurs when a particle's ionisation track affects several transistors causing multiple simultaneous single event upsets. Multiple bit upsets are particularly damaging because they often cannot be handled by simple error correction protocols.

The susceptibility of a particular component to single event effects is quantified using a measure called Linear Energy Transfer (LET). LET measures the energy transferred dE/dt by a single particle per unit length of absorbing material. LET is usually expressed in units of MeV-cm^2/mg. Individual components are then rated by the largest LET strike that, in testing, did not cause a single event effect. The minimum acceptable LET threshold for ORBITALS was to be set in Phase B. However, for screening purposes, a target of 50 MeV-cm^2/mg and a minimum of 35 MeV-cm^2/mg were used.

It is important to understand the limitations of LET screening. LET assumes that a single effect is related to total energy transferred regardless of source (X-ray, electron, proton, heavy ion). This is a useful approximation but isn't always true. Also, LET testing is often done at 90^o incident angles for simplicity of testing. However extrapolating to other incident angles is non-trivial as the apparent semiconductor cross-section decreases while the possibility for multiple bit upsets increases. LET is a useful screening tool but cannot completely quantify single event effects.

2.3.3.3 Internal Charging

Internal charging occurs when penetrating electron radiation causes isolated charge accumulation. During times of high electron flux, the accumulation rate can significantly exceed the bleed rate and these isolated charges can result in sufficient voltage to cause arcing and electrostatic discharge (ESD) interference. Internal charging is mitigated in two ways. Wherever possible, floating conductors are connected to ground to prevent charge build-up. Shielding is also used to reduce the electron flux experienced by the electronics. The ORBITALS shielding requirements to mitigate internal charging are based on the "safe level" of 10^5 electrons/(cm^2 s) averaged over 10 hour intervals found by Fennell et al. [2000].

Figure 2.8 shows the expected worst case electron flux behind various levels of Aluminium shielding as predicted by two different radiation models. According to the AE-8 model, 8 mm of Al is sufficient to reach the "safe level" of 10^5 electrons/(cm^2 s). The CRRES ELE model requires 10-11 mm of Al. This suggests that the 8 mm of Al required for TID mitigation should significantly mitigate internal charging. However, during times of high electron flux, some internal charging should be expected.

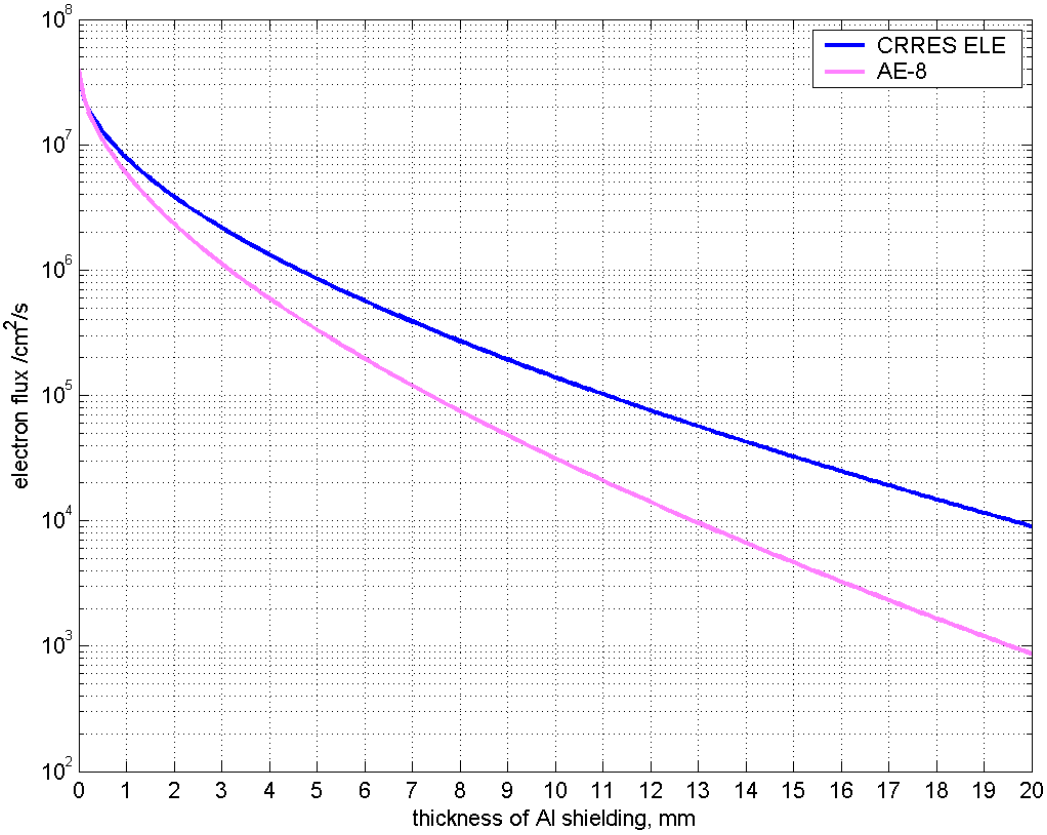

Figure 2.8: Shielding thickness and modelled short-term flux of electron radiation in the raised perigee orbit. Taken from Ozeke & Mann [2011].

2.3.4 Thermal Environment

The ORBITALS mission provides two very different thermal environments for the FGM instrument. The electronics are mounted within the spacecraft body which presents a thermally managed interface to the instrument. The sensor is deployed at the end of a boom constructed from a fine fibreglass truss and, to a first approximation, is perfectly thermally isolated.

The spacecraft specifies that the FGM electronics package will be maintained between -40^o C and +60^o C during instrument operation and -55^o C and +85^o C in non-operating survival mode. The instrument must manage its internal thermal environment such that all components remain within specification. As the instruments operate in vacuum, the electronics must be designed to conduct all generated heat to the instrument case and on to the spacecraft interface without generating hotspots.

The sensor thermal environment is potentially a more difficult issue as the spacecraft provides no thermal management and there is essentially no conductive route to dissipate heat since the sensor is located at the boom end. This is complicated because, during normal operation, the sensor will be heated by incoming solar radiation. However, during eclipse, the sensor is in total darkness and has only internally generated heat to maintain its temperature.

Full thermal analysis of the instrument is normally completed in the detailed design phase (Phase C) of a mission and is beyond the scope of this thesis. However, some preliminary modelling and design consideration are discussed in Section 4.5.5.

2.3.5 Electromagnetic Cleanliness

The Electromagnetic Cleanliness (EMC) of the ORBITALS spacecraft and instruments is essential to ensure that the electric and magnetic science measurements are free of local contamination. An EMC control board, staffed by senior mission scientists and engineers, was formed to review and audit all probable EMC noise sources. The dynamic cleanliness requirements were to be set during the Phase B preliminary design and remain To Be Determined (TBD). The three key requirements are:

1. The stray static magnetic field at the boom-end must be less than 1 nT (0.1 nT goal);
2. The stray dynamic magnetic field amplitude between 0.001 Hz and 10 kHz must be below a TBD value; and
3. The stray dynamic electric field must be minimized below 400 kHz (threshold TBD).

All components must be screened for magnetic materials to control the stray static field. Common issues include transformer cores, steel pins in connectors, bolts and nuts and the metallisation used in capacitors and resistors.

Another source of electromagnetic noise is unintentional current return through the spacecraft body. All instruments are required to be fully transformer isolated from the spacecraft power supply and all inputs and outputs must be floating differential pairs to minimize signal radiation from unbalanced current flow.

All clocks and possible radiation sources were be audited and reviewed by the EMC control board. For the FGM, the sensor is known to radiate magnetic noise at multiples of the core drive frequency. The core frequency should be above the 10 kHz magnetic range of interest for the SCM payload to prevent interference.

2.3.6 Reliability Requirement

Table 2.3 is taken from the ORBITALS MRD by Mann et al. [2009] and shows the sensitivity of each science objective (Objectives #1 to #11) to the loss of a single instrument from the payload. The ORBITALS mission was to be declared a success if the primary objective (Objective #1) or two of the three secondary science objectives (Objectives # 2 to 4) were met. The instruments and their acronyms were previously discussed in Section 2.1.3.

Objectives	#	SCM	FGM	HEPT	PII	EEPS	EFW	REPT	CODIF	REM		DDCM
										PM	DDM	
Primary	1		R	Y		Y	R	Y				
Secondary	2		R	Y		Y	R	Y				
	3		Y				Y					
	4	Y	R		R		Y					
Secondary	5			Y		Y		Y				
	6			Y		Y		Y				
	7									Y	Y	
	8											R
Tertiary	9		R				R		R			
	10	Y	R				Y		R			
	11								R			

Table 2.3: Instruments required for each science objective. Taken from Mann et al. [2009].

> Red means loss leads to the inability to meet the minimum measurement requirement for that objective. Yellow means instrument loss leads to a significant degradation of the measurement; however, redundancy or partial redundancy exists in the onboard payload suite to meet the minimum measurement requirement. [Mann et al., 2009]

Table 2.3 clearly shows that the loss of the FGM instrument would prevent mission success. This violates the principle of no single point failures and leads to an unachievable reliability requirement for the FGM. The ORBITALS mission is specified to have a reliability of better than 0.72 (out of a maximum of 1) after 18 months on-orbit with a minimum reliability of 0.85 for each payload. This figure is calculated accounting for both the spacecraft and the science payloads needed for mission success combined in series and parallel according to the multiple routes to mission success. Since the FGM is involved in almost all the science objectives, the combinatorics of the multiple routes to mission success lead to a reliability requirement for the FGM of about 0.95 after 18 months, which is considered un-achievable for a high-radiation environment.

This difficulty was addressed by duplicating the FGM instrument and creating two fully independent and fully redundant magnetometers, each meeting the minimum 0.85 reliability. Assuming that these instruments would then fail independently (e.g., no systematic failure modes) this leads to an overall reliability for the FGM payload of

$$\text{Reliability}_{\text{payload}} = 1 - [(1 - 0.85)(1 - 0.85)] = 0.978 \tag{2.3}$$

which exceeds the 0.95 reliability requirement. Systematic failure modes are difficult to quantify statistically and were considered to be addressed by good design processes,

peer review and formal engineering reviews. Ideally, two unrelated instruments would be employed to prevent a systematic failure from affecting both magnetometers. However, this was prohibitively expensive.

2.3.7 Summary of Constraints

The constraints on the ORBITALS FGM include all the restrictions placed on the instrument design by the ORBITALS spacecraft. These include mass, power, volume, data rate, radiation, cost, and schedule and are formally captured in the Instrument Specification Document by Milling et al. [2009]. A subset of these requirements, which are relevant to the development of the instrument described in this thesis, have been reproduced below. The requirements have been reformatted and modified for ease of reading:

High Cadence mode: Each FGM unit shall support a high cadence mode of at least 128 samples per second;

Peak Power Consumption: The total combined power draw of the FGM payload shall be less than 5 W (including 25% margin);

Electronics Package Mass: The total mass of the FGM electronics box, including both sets of FGM electronics, mounted within the spacecraft, including shielding and case, shall not exceed 5 kg;

Electronics Dimensions: The FGM electronics box shall not be larger, in any dimension, than 150 x 150 x 100 mm;

Sensor Heat Generation: Each FGM sensor, including coils and electronics, on the boom shall generate less than 100 mW of heat;

FGM Average Telemetry Rate: The FGM average telemetry rate shall not exceed the allocation of 6.8 kbps;

Electromagnetic Cleanliness: The FGM payload shall comply with the EMC requirements of the mission;

Radiation TID: The FGM payload shall use only parts with 100 krad minimum radiation tolerance and shall shield all parts with a minimum of 8 mm of aluminium shielding (1 mm is provided by the spacecraft shell and 7 mm must be provided by an instruments electronics box);

Deep Dielectric Charging: The FGM payload shall provide at least a minimum of 8 mm of aluminium shielding to mitigate deep dielectric charging (1 mm is provided by the spacecraft shell and 7 mm must be provided by an instruments electronics box);

Single Event Upsets: The FGM payload shall be designed and constructed to survive and recover from a single event upset of up to 35 LET;

Sensor Survival Temperature Range: Each FGM sensor shall survive indefinitely without damage while not operating within the temperature range of -55 and $+85^o$c;

Sensor Operating Temperature Range: Each FGM sensor shall operate nominally within the temperature temperature range of -40 and $+60^o$c;

Electronics Survival Temperature Range: The FGM electronics shall survive indefinitely without damage while not operating within the range of -55 and $+85^o$c;

Electronics Operating Temperature Range: The FGM electronics shall operate nominally within the temperature range of -40 and $+50^o$c;

Dual FGM units: The FGM payload shall contain two independent FGM instruments operating contemporaneously with independent interfaces to the bus; and

18 Month Reliability: Each FGM unit shall have an independent reliability of 0.85 after 18 months. This gives an overall FGM payload reliability of 0.978 considering the two FGM units as equivalent and independent. The FGM units may operate simultaneously or run with a cold spare;

Storm Operation: The FGM payload shall be designed to operate through geomagnetic storms; and

Product Assurance: The FGM payload will comply with the mission product assurance requirements (these requirements were to be fully defined in a future mission phase).

Chapter 3

Review of Fluxgate Magnetometers

There is an extensive body of literature on fluxgate magnetometery that includes many different measurement techniques optimised for particular applications. Ripka [2001] provides a detailed review to which the interested reader is referred. This chapter describes the physics of the fluxgate mechanism, outlines the standard sensor topologies, discusses three recent space-flight instruments and summarises the state-of-the-art in radiation tolerant spaceflight magnetometers.

3.1 Fluxgate Sensor Physics

3.1.1 The Generalised Induction Equation

The sensing mechanism for a FGM is a direct consequence of Faraday's law for a coil of wire with a core with a high magnetic permeability. The classical derivation, following Ripka [2001], starts with the relation of induced voltage V_i to change of magnetic flux Φ with time.

$$V_i = \frac{d}{dt}\Phi \tag{3.1}$$

For a coil of wire with N turns, an area A perpendicular to the magnetic field, and a core with effective relative permeability μ_r in a magnetic field H, this equation expands to:

$$V_i = \frac{d}{dt}\Phi = \frac{d}{dt}\left(NA\mu_0\mu_r H\right). \tag{3.2}$$

μ_0 is the permeability of free space. However, as A, μ_r and H are time-dependent it is necessary to expand the equation to:

$$V_i = \frac{d}{dt}\left(NA(t)\mu_0\mu_r(t)H(t)\right). \tag{3.3}$$

Considering each time-varying term independently gives a generalised induction equation for a coil of wire with a permeable core:

$$V_i = (NA\mu_0\mu_r)\frac{dH}{dt} + (N\mu_0\mu_r H)\frac{dA}{dt} + (NA\mu_0 H)\frac{d\mu_r}{dt} \tag{3.4}$$

The first term in Equation 3.4 generates voltage in response to a changing magnetic field. It is the basis of operation of an induction coil (search coil) magnetometer; however, it cannot be used to sense the constant magnetic field since $\frac{dH_{constant}}{dt} = 0$. The second term generates voltage in response to a change in the area of the sense coil. This could theoretically be used to measure the magnetic field by rotating the coil to change the effective cross-section area. However, this approach is generally impractical and rarely used. The third term generates voltage in response to changes in the effective relative permeability inside the coil of wire and forms the basic equation for a fluxgate magnetometer. The first and second terms are error sources to a fluxgate and often need to be isolated and removed. For now, we will consider only the third term leaving:

$$V_i = (NA\mu_0 H)\frac{d\mu_r}{dt} \tag{3.5}$$

3.1.2 Fluxgate Sensor Head Layouts

Physically, equation 3.5 means that any modulation in the effective permeability μ_r will result in a voltage that is proportional to the magnetic field H. An extremely simplistic fluxgate could conceptually be constructed by dropping a chunk of permeable material, for example a nail, through a short loop of wire as shown in Figure 3.1 (adapted from J. R. Bennest, Personal Communication, 2011).

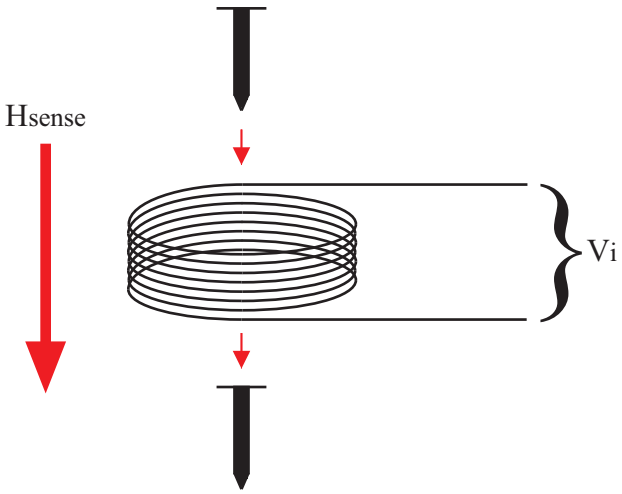

Figure 3.1: Conceptual fluxgate sensor using a moving nail and coil of wire.

When the nail is outside the coil the relative permeability μ_r will be that of air (~ 1). The relative permeability will suddenly change to that of steel (~ 100) when the nail enters the coil and then return to that of air (~ 1) when the nail exits the coil. These two steps in relative permeability will cause $d\mu_r/dt$ as the nail enters and exits the coil. Each $d\mu_r/dt$ will induce voltage that is proportional to the component of the magnetic field aligned with the coil of wire (the H_{sense} direction).

A more practical way of creating a fluxgate sensor is to modulate the permeability of the core by periodically saturating the core with a drive winding. The simplest implementation of this is the rod fluxgate that is shown schematically in Figure 3.2.

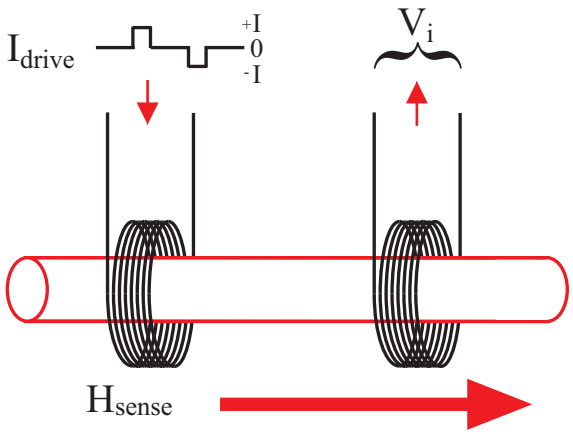

Figure 3.2: Single axis fluxgate sensor layout using a rod core.

Figure 3.2 shows drive current I_{drive} and drive winding. The peak current $\pm I$ is chosen such that I_{drive} will periodically saturate the core and then allow it to un-saturate. The bipolar drive current is used so that the core saturation alternates direction and does not magnetise the core. Each unsaturated/saturated transition is necessarily a $d\mu_r/dt$ event and induces a voltage V_i proportional to the magnetic field in the H_{sense} direction. The main disadvantage of this design is that it is functionally a transformer and couples the drive signal I_{drive} to the sense output V_i. I_{drive} and its harmonics can be very large making it difficult to isolate and measure the fluxgate signal.

An alternate design (and which is used in this thesis) is the "ring core" layout shown in Figure 3.3. The bar is replaced with a ring such that the drive winding is now a toroid. The fluxgate action remains the same, I_{drive} periodically saturates the ring core, this modulates the permeability seen by the pickup windings inducing a voltage V_i proportional to the magnetic field in the H_{sense} direction. However, the transformer action is reduced and the anti-symmetry of the field generated by I_{drive} reduces the contamination of V_i. Another advantage of a ring core sensor is that, since the ring is grossly cylindrically symmetric, it can be rotated within the sense winding to minimize the drive signal coupling, due to the imperfections in the ring and windings, without significantly affecting the sensing action.

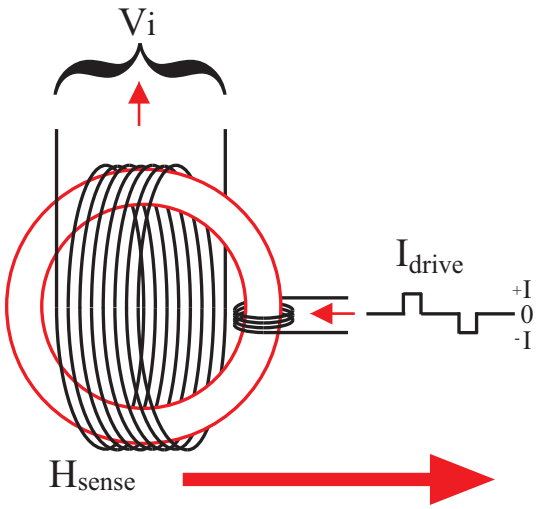

Figure 3.3: Single axis fluxgate sensor layout using a ring core. The fluxgate action from saturating the core with current I_{drive} creates a voltage V_i proportional to the magnetic field in the H_{sense} direction.

3.1.3 Magnetic Feedback

Many fluxgate magnetometers use magnetic feedback to improve the linearity of the instrument, to extend the operating range of magnetic field strengths, and to prevent unwanted de-magnetisation effects in the core. A proportion of the averaged sensor output for each component is used to drive a solenoid that opposes the local magnetic field for that component. This can either require another set of windings parallel to the sense coil or can be achieved by injecting current back into the sense coil itself.

The feedback current can be scaled to completely cancel the field at the sensor allowing the fluxgate action to act as a small-signal null detect. In this case, the amount of current required to null the sensor becomes a proxy for the local magnetic field.

3.1.4 Other Sensor Layouts

There are several other commonly used layouts for fluxgate sensors. Two matched bar cores can be used in series with equivalent, but oppositely wound drive windings. In this configuration, the fluxgate signal adds while the transformer coupled drive signals cancel. An oval or racetrack core can be used as a compromise between a ring-core and bar-core sensor. However, Ripka [2001] reported mechanical issues with small amounts of mechanic stress concentrating in the regions of high curvature and causing noise. Finally, some instruments use a Helmholtz coil pair for the feedback winding to ensure a uniform magnetic feedback field. However, it isn't clear that this significantly improves instrument performance.

3.1.5 Standard Detection Technique

The classic design for a fluxgate magnetometer is the second harmonic analog detector, which measures the sensor output at the frequency 2f (twice the drive frequency f). Figure 3.4 shows an example block diagram by Ripka [2001].

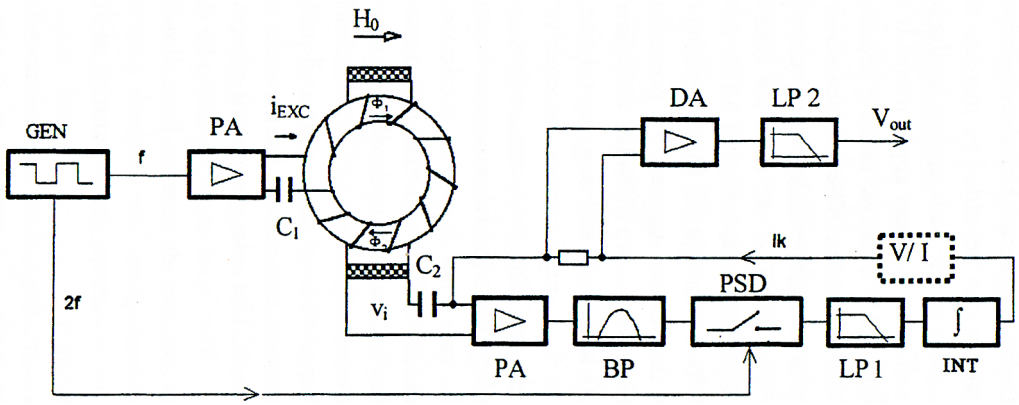

Figure 3.4: Block diagram of a second harmonic fluxgate magnetometer. Taken from Ripka [2001].

Using the nomenclature from Ripka [2001], the drive generator (GEN), and power amplifier (PA) generate a series of current pulses (i_{EXC}) from 0 to $\pm I$ at frequency f, which periodically saturate the core. The external field H_0 then generates a fluxgate voltage v_i at frequency $2f$. This signal is amplified (PA), bandpass filtered (BP) at $2f$ and then chopped by a phase-sensitive detector (PSD in Figure 3.4) locked to twice the GEN frequency. The signal is then low-pass filtered (LP1) to remove the detector edges and then integrated (INT) into a pseudo static voltage corresponding to the measured field. Finally, the voltage is converted into a current and driven back into the sense winding as global negative magnetic feedback. The quantity of current required to null the fluxgate sensor is then measured using a small current sense resistor and a differential amplifier (DA), and low pass filtered (LP2) again to form the final measurement quantity (V_{out}).

This type of second harmonic analog design has historically been the basis of most high-quality fluxgate instruments. A controllable ultra-stable current source can be added to the magnetic feedback current to add or subtract offsets and extend the instruments measurement range in large magnetic fields.

Recent magnetometer literature has generally focused on alternate ways to extract information from the fluxgate signal (e.g., Magnes et al. [2003], O'Brien et al. [2007], and Magnes et al. [2008]). These include directly digitising v_i and implementing the analog signal processing firmware, measuring the phase offset (rather than amplitude) of the v_i spikes and using correlation coefficients between v_i and a reference waveform.

Section 3.2 analyses three recently published space fluxgate magnetometers and discusses their objectives, constraints and design features. Section 3.2.4 provides a summary of relevant recent instruments to describe the state-of-the-art.

3.2 Review of Recent Fluxgates for Space Applications

The new fluxgate magnetometer design described in this thesis was developed for the ORBITALS application because no known existing instrument could meet the mission's science requirements and survive the expected radiation environment. Three notable recent spaceflight fluxgates are described in detail below. The MGF instrument from the CSA e-POP payload is the design on which the instrument in this thesis is based but is not sufficiently radiation tolerant for the ORBITALS mission. The prototype, developed by Imperial College London, represents one of the more extensive recent examples of replacing analog circuitry with digital processing. However, the Imperial College London prototype has a limited range and does not temperature compensate the sensor. NASA's THEMIS fluxgate magnetometer is a recently deployed, and highly successful, spaceflight instrument. However, the THEMIS instrument uses radiation mitigation techniques which are not considered acceptable in the harsh radiation environment of the ORBITALS mission. Each of these instruments is discussed below.

3.2.1 CASSIOPE/e-POP MGF

The MGF payload for the e-POP mission by Wallis et al. [2006] was developed through a collaboration between Magnametrics, Narod Geophysics Ltd. and Bennest Enterprises Ltd. Flight firmware for the MGF was developed by the author and Jonathan Schmidt of Minerva Technology Inc. The satellite has two fluxgate sensors deployed at different distances along a single boom and an electronics box containing independent electronics for the two sensors.

Many of the CASSIOPE/e-POP science objectives require knowledge of the magnetic field. However, the primary objective for the MGF payload is the characterization of electric currents flowing into and out of the auroral ionosphere. These currents distort the local magnetic field, causing errors in magnetic mapping from the magnetosphere to the ground, carry significant energy into the ionosphere and can support the propagation of electromagnetic Alfvén waves.

Ideally, these currents would be characterised by measuring the induced vector curl in the local magnetic field. However, this cannot be practically achieved on a single low-altitude spacecraft. Instead, the gradient of the field is measured along the spacecraft track and combined with the physically motivated assumption that the currents are aligned with the magnetic field. This led to a requirement for a resolution of about 0.1 nT and a sampling rate of 160 samples per second. Finally, the difference between measurements of the two MGF instruments can be used to estimate and compensate for the magnetic signature of the spacecraft following the technique of Ness et al. [1971].

The MGF sensor is based on the NASA MAGSAT sensor design by Acuña et al. [1978] and employs two toroidally wrapped Infinetics ring cores. Each ring is then wrapped with two orthogonal sense coils such that X and Y are each derived from a single ring while Z is the average of the two rings. The sense coils are also used as magnetic feedback coils to null the local field and allow the Infinetics cores to operate in a small signal configuration.

No suitable Analog to Digital Converter (ADC) capable of 21 bits of resolution at 160 samples per second was available when the MGF was being designed. Therefore, a 12 bit Digital to Analog Converter (DAC) was used to null the majority of the main field using the sense/feedback coil and the residual -128 to +128 nT field was digitised using a 12 bit ADC.

The cores are driven into hard saturation at 16,457 Hz and the resulting second harmonic output is amplified, synchronously detected, analog integrated and then measured. Analog temperature compensation is used to reduce temperature dependence due to changes in the sensor geometry.

The MGF has a single operating mode and is designed to operate continuously. The two magnetometers making up the MGF payload are synchronised to reduce cross-contamination, are functionally identical, and independent to provide redundancy. However, the two sensors share a common communication channel so, if the payload loses synchronisation with the spacecraft, the inboard magnetometer stops transmitting to prevent both magnetometers from trying to simultaneously talk on the same channel.

The radiation considerations of the instrument are not discussed in detail except that "The proto-type and proto-flight instruments were exposed to 3000 Rads of radiation, respectively, and both continued to operate properly" [Wallis et al., 2006]. For context, the total dose for the mission is estimated by Thomas et al. [2006] as 8.6 krad behind 3 mm of Al, 4.5 krad behind 5 mm of Al and 3.4 krad behind 7 mm of Al. The instrument is based around an Atmel Microcontroller, which is a consumer grade part and has no manufacturer specified radiation tolerance. Radiation testing by Avery et al. [2011] of another part in the same family, the ATMEGA1280, found functional failure at 18.3 krad. This appears to have been acceptable for CASSIOPE/e-POP. However, for the harsh radiation environment of ORBITALS, the combination of consumer grade electronics and low radiation tolerance would not be acceptable.

3.2.2 Imperial College London - Prototype

The Space Magnetometer Laboratory of Imperial College London has developed a prototype radiation tolerant digital fluxgate magnetometer [O'Brien et al., 2007] based on the analog design used on the Double Star mission. The prototype is a proof of concept of a highly integrated, Field Programmable Gate Array (FPGA) based, digital instrument that can be manufactured to a 100 krad tolerance.

The prototype is not linked to a specific mission and therefore has no formal science requirements. Its measurement goals were set to a generic requirements including a noise floor of less than 10 pT/$\sqrt{\text{Hz}}$ noise, a 10 pT resolution and a measurement rate of greater than 30 samples per second.

The sensor is based on the design used for the Double Star mission and features a toroidally wrapped ringcore with a common sense/feedback winding tuned to the second harmonic of the drive frequency. The output of the sense winding is amplified and driven into a single bit comparator connected to a FPGA. The FPGA implements a Sigma–Delta ADC conversion algorithm to digitise the sensor to 13 bits of resolution

without requiring a dedicated ADC chip. The FPGA also generates a feedback bit stream that is level shifted and then driven back into the sense/feedback winding using a feedback resistor.

The digitised sensor output is run through a digital bandpass filter and the magnitude and phase of the 2f output is measured by calculating a correlation against a reference 2f cosine waveform. The digital filter length is picked so that it has a null at f and 3f to reduce the impact of drive frequency noise. This algorithm generates 976 samples per second of raw data that is digitally low-pass filtered and down-sampled to a final data rate of 22 or 122 samples per second.

A significant limitation of this design is that the total instrument range is limited to $\pm$327 nT. The authors note that achieving the required instrument linearity across a larger range will require a more involved DAC scheme.

The radiation considerations of the instrument are discussed at a conceptual rather than detailed level in the instrument paper. The instrument is described as "radiation tolerant" because the majority of the signal processing is done in a FPGA, which has a rad-hard equivalent part. The Sigma–Delta converter and digital feedback design removes the dependence on traditionally radiation soft ADC and DAC components. However, this technique introduces a dependence on analog gates and comparators. The authors note that "whilst versions of these components radiation tolerant up to a TID of 100 krad do exist, they are not as fast (slower switching times, longer propagation delays) as the commercial parts. This design must be tested with radiation tolerant components." This suggests that it may not be a trivial matter to manufacture a fully 100 krad tolerant instrument while maintaining the performance achieved in the prototype.

3.2.3 THEMIS FGM Instrument

The Technical University of Braunschweig in Germany developed the fluxgate magnetometer instrument [Auster et al., 2008] on the five satellite THEMIS mission. Each satellite had a single fluxgate sensor deployed on a two meter boom. The fluxgate is not a stand-alone instrument as its electronics are tightly integrated with the central Power Control Unit (PCU) and Instrument Data Processing Unit (IDPU). The high level of integration, short boom, and lack of a second sensor reduced cost, mass and power but created stringent EMC requirements and required significant EMC screening once the spacecraft was integrated.

The THEMIS FGM was designed to measure magnetic perturbations from geomagnetic substorms, which pass the spacecraft on time scales of $\sim$0.1 s with total changes in the single nT range. It was also intended to study Extremely Low Frequency (ELF) waves in the 15-40 Hz range, which in previous observations (Equator-S) had amplitudes in the order of 0.5 nT. These science targets led to minimum measurement requirements of at least 0.1 nT resolution at a cadence of 10 Hz. The FGM was also required to measure the main field near the Earth for attitude determination leading to a maximum field strength requirement of 25,000 nT.

The THEMIS FGM is a digital instrument where the output from the fluxgate sensor

is pre-amplified and then immediately digitised. Essentially all the data processing is done digitally in an FPGA. The feedback field for the sensor is constructed from two cascaded 12 bit DACs and the remaining field is digitised with a 14 bit ADC. The 24 bit magnetic field measurement is then the appropriately scaled and summed value of the two DACs and the ADC. The sensor is based on a custom ring-core made from a rolled foil of 13Fe-81Ni-6Mo alloy. The ring-cores are treated with an ageing process, which includes ultra sonic treatment, vibration, and temperature cycling, to achieve a noise floor of 5 pT/$\sqrt{\text{Hz}}$ at 1 Hz. The cores are wrapped toroidally and then driven at 8192 Hz.

As shown in Figure 3.5a, the THEMIS FGM uses two nested ring-cores with pairs of pickup windings for X and Y and a single larger pickup winding for Z. The THEMIS FGM also uses separate Helmholtz coils to provide feedback on each axis (Figure 3.5b).

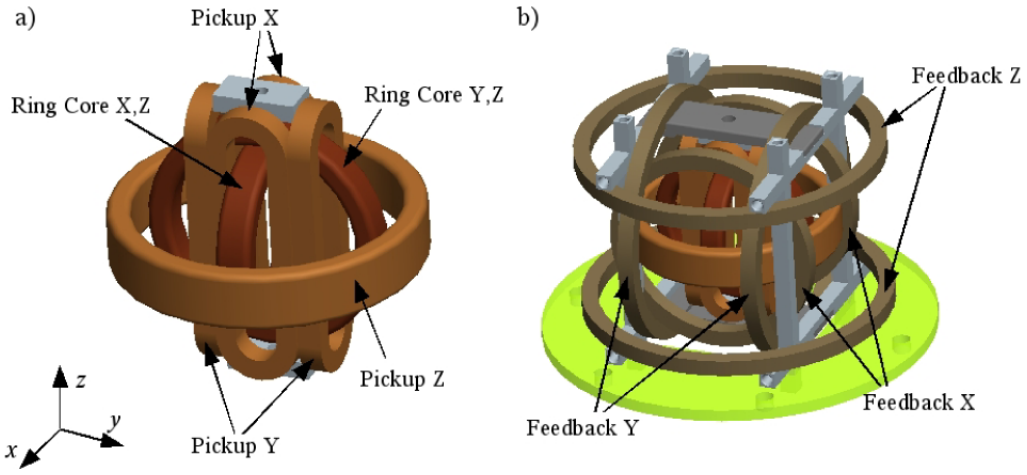

Figure 3.5: THEMIS fluxgate magnetometer sensor schematic. Taken from Auster et al. [2008].

The output of the sensor is digitised at four times the drive frequency with the intention of removing the inductively coupled odd harmonics of the drive signal. The feedback Helmholtz coils are used to almost completely compensate the external field and use the ring-core in a small-signal configuration. The data product is created from the two DACs and the ADC using calibration coefficients determined before launch. The data is then 'ranged' by selecting the smallest 16-bit range that can contain the magnitude of the signal, shifting the 24 bit measurement appropriately into a 16 bit datum, and marking the data packets with current scaling. In some cases, the data stream is filtered and down-sampled to a lower cadence than the nominal 128 samples per second.

The approach to radiation tolerance is not described in detail by Auster et al. [2008] except that "Frequent crossing of the radiation belt requires a reasonable radiation tolerance of the electronics". However, the paper cites the use of "14-bit ADCs (Maxwell 7872) and 12-bit DACs (Maxwell 8143)". These parts achieve their radiation tolerance partially through embedded shielding (trade-name "Rad-Pack"). This approach to radiation mitigation tends to have geometric vulnerabilities (e.g., vulnerable to omnidirectional radiation) and is less effective against high-energy radiation, which tends

to penetrate the shielding. For example, the manufacturers datasheet [Maxwell Technologies, 2009] states "In a GEO orbit, RAD-PAK provides greater than 100 krad (Si) radiation dose tolerance.". For the ORBITALS missions, with long dwells in the highly energetic radiation belts, this type radiation mitigation is not considered acceptable.

3.2.4 The State of the Art

Table 3.1 summarises the key performance metrics of recent and historical fluxgate magnetometers designed for space applications.

Mission	Max B (±nT)	Resolution (nT)	Rate (sps)	Noise ($pT/\sqrt{Hz}$) at 1 Hz	Power (W)	Reference
MJS'77 - High	50,000	8 ranges	25	1000	0.12/axis	[Acuña, 1974]
MJS'77 - Low	2,000,000	2 ranges	25	13	0.09/axis	[Acuña, 1974]
Pioneer XI	1,730,000	338	0.08	unknown	0.3	[Acuña & Ness, 1975]
CRRES	45,000/850	22/0.4	16	unknown	unknown	[Singer et al., 1992]
Astrid-2	61,865	0.118	2048	unknown	unknown	[Pedersen et al., 1999]
AMPTE/IRM	60,000/4000	1.8/0.12	32	25	6.9	[Luehr et al., 1985]
CASSIOPE/e-POP	65536	0.0625	160	7	1.1	[Wallis et al., 2006]
Proto – DAWN	2,000	70	144	7	unknown	[Magnes et al., 2003]
DoubleStar	32764/128	4/0.016	22	5	3.6	[Carr et al., 2005]
Proto – Imperial	327	0.01	22/122	10	unknown	[O'Brien et al., 2007]
Proto – SMILE	50,000	0.1	250	30	0.33	[Forslund et al., 2008]
Proto – ASIC	60,000	0.014	128	8	0.06	[Magnes et al., 2008]
THEMIS	25,000	0.003	128	10	0.8	[Auster et al., 2008]
RBSP	65536/4096	2/0.13	64	unknown	unknown	[Kletzing, 2011]

Table 3.1: Performance characteristics of relevant spaceflight fluxgate magnetometers.

A modern fluxgate magnetometer should meet the parameters in Table 3.2 to be competitive with the best available instruments and prototypes available worldwide.

Parameter	State of the art
Range	± 65,000 nT
Resolution	0.010 nT
Cadence	100 sps
Noise	10 $pT/\sqrt{Hz}$ at 1 Hz
Power	< 1 W

Table 3.2: Performance characteristics of a state-of-the-art spaceflight fluxgate.

No known existing instrument can simultaneously provide this state of the art performance while meeting the stringent radiation requirements of the ORBITALS mission. Chapter 4 discusses the design techniques used to improve the CASSIOPE/e-POP MGF instrument design to combine the robust radiation tolerance of a primarily digital instrument with the temperature compensation of a traditional analog fluxgate magnetometer and meet the ORBITALS mission requirements.

Chapter 4

Radiation Hard Spaceflight Instrument Design

4.1 System Architecture and Nomenclature

The nomenclature used in this chapter to describe the FGM payload and subcomponents is as follows:

The FGM sensor refers to one three-axis sensor designed to be mounted on a spacecraft boom. The FGM sensor is composed of a mounting block, two ring cores, two drive windings, and three sense coils.

The FGM electronics refers to one set of electronics, which is capable of supporting one FGM sensor. The FGM electronics is composed of analog filters and digitizers for signals from three components from the sensor, an FPGA, and support electronics.

A FGM unit refers to an independently, functioning combination of one FGM sensor and one FGM electronics set.

The FGM electronics box refers to the shielded electronics box designed to be mounted within the spacecraft. Since for some applications dual fluxgates units may be flown, this box may contain more than one unit.

The FGM payload is, for the purposes of this thesis, assumed to be composed of two independent FGM units. The FGM electronics for both instruments are hence housed in one FGM electronics box within the spacecraft.

4.2 Instrument Heritage

The FGM payload is based on a previously developed design by Magnametrics, Bennest Enterprises Ltd. and Narod Geophysics Ltd (see [Wallis et al., 2006]), which will be flown on the e-POP payload of the CSAs CASSIOPE satellite as the MGF payload.

The MGF design is based on a ground instrument designed by Narod Geophysics Ltd and Bennest Enterprises Ltd. That design was, in turn, based on work done by Mario Acuña and used in many missions (e.g., Acuña et al. [1978]).

This thesis describes modifications and improvements to the MGF design for the ORBITALS mission and the proposed PRIMO payload on the CSA's PCW mission. The new FGM design uses only electronic components that have 100 krad, Class S equivalents to provide a way of manufacturing the instrument for spaceflight applications in a high radiation environment. The physical fluxgate sensor, the ring-core drive circuitry, the isolated power supply, and the analog temperature compensating are inherited from the MGF instrument with modest modification. The instrument concept and all other instrument subsystems (including the integration of digital feedback with analog temperature compensation) were redesigned in this thesis for the ORBITALS application. The new design presented in this thesis has a reduced parts count and is no longer dependent on high-performance commercial components. This has been achieved by removing much of the analog signal conditioning and providing equivalent digital functionality in an FPGA.

The FGM presented in this thesis reached the fidelity of a bench prototype demonstrating the critical instrument subsystems and allowing the instrument performance to be tested and quantified. It includes a new digital subsystem, developed at UAlberta for the CSA ORBITALS mission, a new analog subsystem developed in collaboration with Bennest Enterprises Ltd., and a modified fluxgate sensor already developed and available from the CSA's CASSIOPE/e-POP satellite. The sensors used in early development were too noisy to validate the resolution and noise performance of the instrument. The test results shown in this thesis were taken using a sensor constructed from low-noise Infinetics ring cores. This sensor is a spare from the CASSIOPE/e-POP MGF instrument and was temporarily loaned to the author by Don Wallis of Magnametrics for this development work. Sensors for flight on new missions would need to be secured separately.

4.3 Concept of Operations

4.3.1 Sensor Design

The sensor used for performance testing in the FGM is an engineering spare from the CSA's CASSIOPE/e-POP mission. The sensor uses two orthogonal ring-core sensors (Figure 4.1) to measure three geometric components of the magnetic field.

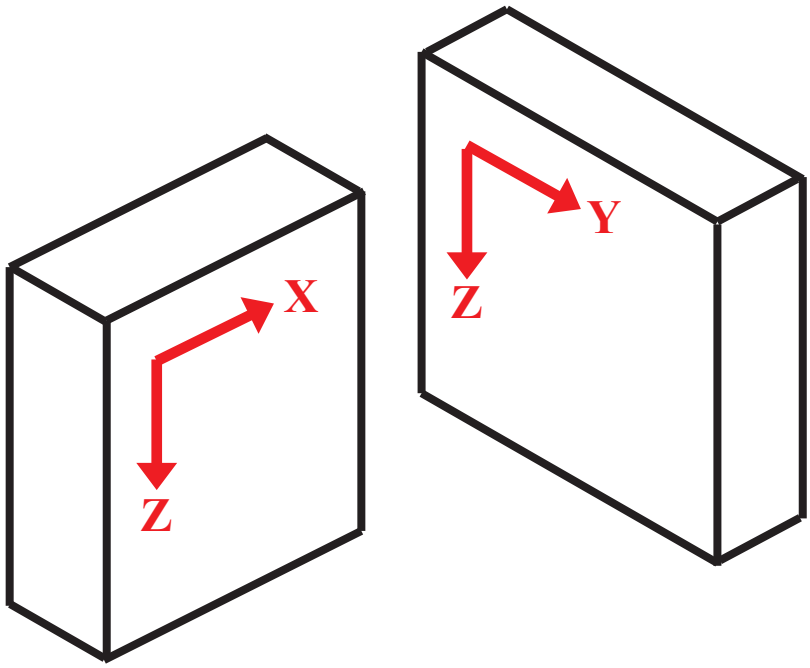

Figure 4.1: Layout and composition of X, Y, and Z axes of the fluxgate sensor showing instrument and measurement coordinate system. (Adapted from J. R. Bennest, Personal Communication, 2011).

Figure 4.2 shows how the X and Y component components each have a single sense winding while Z uses the sum of the orthogonal components of the two cores. The sensor uses legacy Infinetics cores of which only a small stock remain. The double wound sensor layout requires one fewer core than winding each component on a separate ring. This gives the Z component slightly different sensitivity, but this effect is removed during calibration. Triple winding a third component on a single ring is technically possible (see Forslund et al. [2008]) but mechanically tricky and not well suited to the planar geometry of the ring. Figure 4.3 illustrates the sensor used in the prototype instrument.

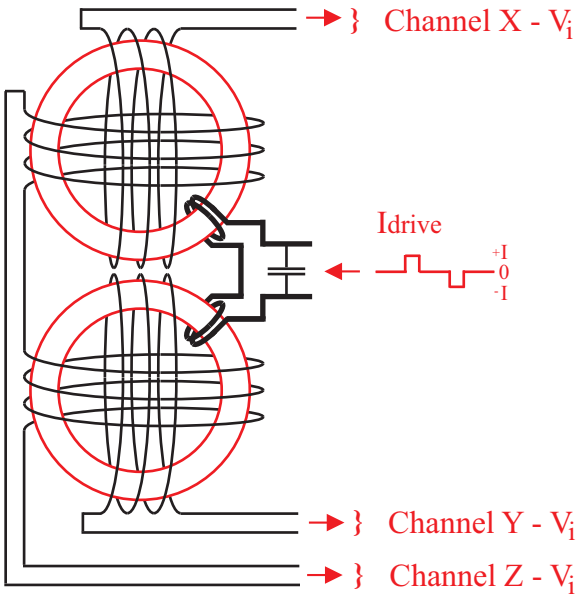

Figure 4.2: Schematic showing the wiring of the X, Y, and Z components and the drive coil. The two cores are mounted orthogonally so that X, Y, and Z measure three orthogonal components of the vector field. The double-wound component has a different analog sensitivity, which is compensated in calibration.

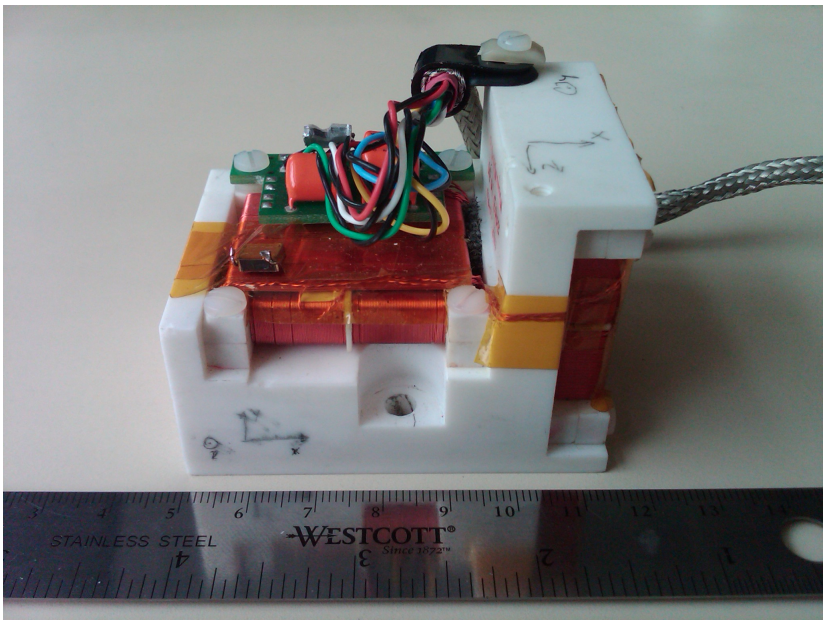

Figure 4.3: Fluxgate sensor - CASSIOPE/e-POP engineering model

Both rings have toroidal drive windings, which are connected in series and driven with a common signal. This ensures that both cores simultaneously saturate when $I_{drive} = \pm I$ and unsaturate when $I_{drive} = 0$. The single capacitor in Figure 4.2 is tuned to the drive

coil and drive frequency to speed up the core saturation. The capacitor also provides temporary energy storage to reduce the current transients in the drive cabling.

4.3.2 Instrument Concept

Figure 4.4 repeats the classic second harmonic detector described in Section 3.1.5. In the current prototype FGM we follow the same general design concept except that several functions are implemented in digital processing.

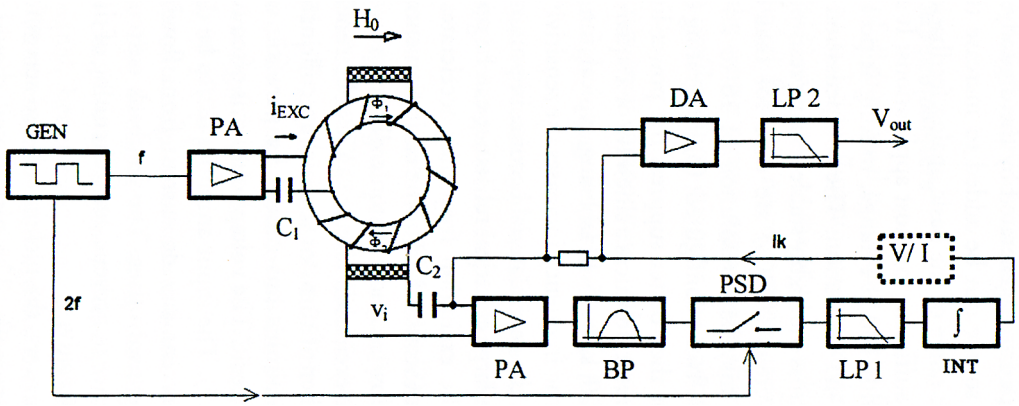

Figure 4.4: Block diagram of a second harmonic fluxgate magnetometer. Taken from Ripka [2001].

The bandpass (BP), phase synchronous detector (PSD), low-pass (LP1), and integrator (INT) hardware in the classic design are replaced with an ADC to digitize the signal, an FPGA to execute signal processing in firmware and a DAC to provide feedback. Figure 4.5 shows a single component block diagram of the new instrument. An FPGA controller generates a 28,800 Hz drive signal that is power amplified (PA) and sent into the drive winding to periodically saturate and and unsaturate the ring cores. This modulates the core permeability in each magnetometer component, creating a fluxgate signal that corresponds to the magnetic field strength inside the sensor. The fluxgate current is converted to a voltage (I/V) and is sampled by the analog to digital converter (ADC) to become the input to a control loop implemented in the FPGA. The output of the control loop is converted into high-precision current (V/I) providing feedback to servo the magnetic field in the sensor head towards zero field. The major subsystems of the instrument are discussed in Section 4.4 below.

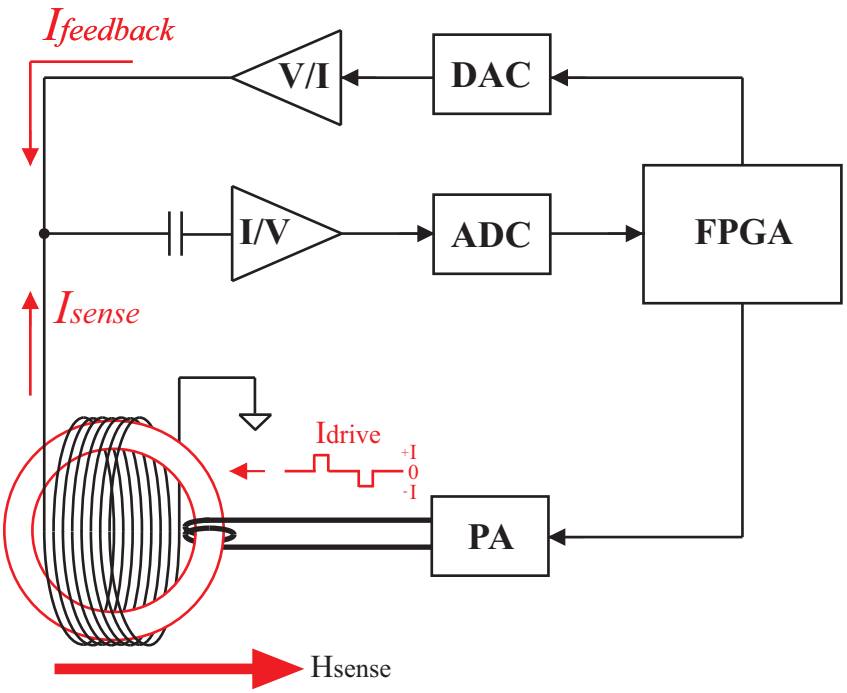

Figure 4.5: Schematic of one fluxgate component showing the major components.

The bandpass (BP) filter is removed and phase synchronous detector (PSD) in the classic design is replaced with an ADC sampling the instantaneous output of the sensor. The low-pass filter (LP1) and integrator (INT) in the feedback loop are implemented in digital processing. The differential amplifier (DA) and measurement low-pass filter (LP2) are no longer required as the final data product can be derived from digitally filtered data. A DAC is used to provide feedback based on the digital data.

4.4 Major Functional Subsystems

The FGM payload is composed of two independent fluxgate units. As shown in Figure 4.6, each instrument has a several major subsystems as described below:

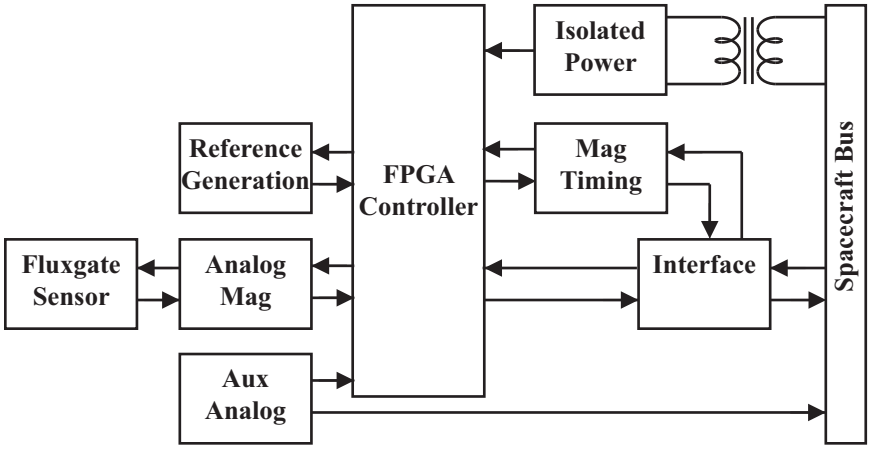

Figure 4.6: Major functional subsystems of the fluxgate magnetometer.

Fluxgate Sensor is based on two double-wound permalloy ring cores;

Mag Timing generates drive signal for the sensor and allows for synchronous detection of the sensor error signal. The drive signal must be synchronized between the two fluxgate instruments in the FGM payload to prevent interference;

Analog Mag contains analog circuitry to null the fluxgate sensor and condition the error signal for digitization;

Reference Generation provides thermally stabilized voltage reference;

Isolated Power provides transformer isolation from bus power and regulation of the required multiple internal rail voltages. The switching power supply must by synchronized between the two fluxgate instruments in the FGM payload to prevent interference;

FPGA Controller provides control logic for each instrument. The controller generates Pulse Width Modulation (PWM) signals for digital to analog conversion. The controller also accumulates and telemeters science data;

Interface provides RS-422 high speed serial connection for data output at one packet per second. It also implements a RS-422 serial port for command and control; and

Aux Analog provides thermistor outputs to allow the spacecraft to monitor the state of health of the payload and provide thermal management.

Each FGM unit has three orthogonally aligned magnetometer axis constructed around two permalloy ring cores (cf. Figure 4.1). The three magnetometer components are mounted on a block of machinable ceramic called MACOR, which has excellent temperature stability. This keeps the components from mis-aligning due to temperature variations. The FPGA controller generates a drive signal that periodically saturates and un-saturates the ring-cores. This modulates the core permeability in each magnetometer component creating current pulses corresponding to the local magnetic field

strength. These current pulses are converted to a voltage and digitized in phase with the drive signal creating a synchronous detector. The amplitude of these current pulses is the input to a control loop implemented in the FPGA. Two summed PWM signals create a high-precision current source that is driven back into the sense coil to oppose the environmental field and drive the magnetic field inside the sensor head towards zero.

Because the digital feedback is always trying to drive the field in the sensor to zero, the output of the sensor is both a partial measurement of the field and the instantaneous error in the digital feedback value. A detailed breakdown of this algorithm is provided in Section 4.9.3. The sensor output is therefore referred to as the 'error signal' to be consistent with control system nomenclature. The output data for each magnetometer component is then the scaled sum of the feedback PWMs and the error signal. Data are typically accumulated and packaged with state of health information into one-second packets, which are telemetered to the spacecraft.

4.5 Preliminary Interface Design

The FGM payload interfaces defined for ORBITALS and PRIMO were slightly different due to variations in spacecraft designs. However, the major functional interfaces are common to both designs and are described below.

4.5.1 Power Supply and Grounding Interface

The FGM payload will meet the grounding and power isolation requirements set by the mission. Each FGM unit implements a custom switching power converter that provides full isolation from the bus supply, is internally current limited, is self-starting, synchronizes to the instrument clock to prevent interference with instrument operation, and synchronises with the other FGM unit to prevent cross-interference. The prototype power supply design is inherited from the e-POP MGF design and uses a commercial controller chip. A rad-hard controller chip is available, but has no drop-in equivalent commercial part. A future, higher fidelity, prototype could implement the rad-hard controller chip; however, both parts are well understood and the risk of moving to the rad-hard chip is considered very low.

4.5.2 Command and Control Interface

Each FGM unit implements a standard serial interface (19200 8N1) for command and control. This interface is used to transmit science data in the prototype. However, in the flight hardware, it will be used as the control interface to change sampling rates and to tune instrument performance while in orbit via table uploads.

4.5.3 Data Handling and Telemetry Interface

Each FGM digitizes and accumulates science measurements to form data packets. The two FGM units operate and send data to the bus independently. The FGM data packets will be a mixture of scientific measurements, timing, sequence and state of health information. The two FGM units must usually be fully redundant to achieve the overall payload reliability and this is a requirement assumed for the design presented here. Consequently, the data paths for the two units must also be completely independent. The format for the data packet on ORBITALS or PRIMO has not been formalized but, for the purposes of this thesis, is assumed to be similar to that used for the CASSIOPE/e-POP mission as shown in Figure 4.7.

column:	1		2		3		4		5		6		7		8	
row:																
1	DLE		STX		PID		MSB length		LSB length		-- spare --		-- spare --		ldmeasurement	
2	aux	1	- 0 -		x-dac	1		y-dac	1		z-dac	1		x-AD	1	
3	y-AD	1		z-AD	1		x-AD	2		y-AD	2		z-AD	2		x-AD
4	%		y-AD	%		z-AD	%		x-AD	&		y-AD	&		z-AD	&
5	aux	2	- 0 -		x-dac	2		y-dac	2		z-dac	2		x-AD	'	
6	y-AD	'		z-AD	'		x-AD	6		y-AD	6		z-AD	6		x-AD
7	7		y-AD	7		z-AD	7		x-AD	8		y-AD	8		z-AD	8
8	aux	%	- 0 -		x-dac	%		y-dac	%		z-dac	%		x-AD	9	
9	y-AD	9		z-AD	9		x-AD	10		y-AD	10		z-AD	10		x-AD
10	11		y-AD	11		z-AD	11		x-AD	12		y-AD	12		z-AD	12
11	aux	&	- 0 -		x-dac	&		y-dac	&		z-dac	&		x-AD	13	
12	y-AD	13		z-AD	13		x-AD	14		y-AD	14		z-AD	14		x-AD
13	15		y-AD	15		z-AD	15		x-AD	16		y-AD	16		z-AD	16
14	aux	'		x-dac	'		y-dac	'		z-dac	'		x-AD	17		
15	y-AD	17		z-AD	17		x-AD	18		y-AD	18		z-AD	18		x-AD
16	19		y-AD	19		z-AD	19		x-AD	20		y-AD	20		z-AD	20
17	aux	6		x-dac	6		y-dac	6		z-dac	6		x-AD	21		
18	y-AD	21		z-AD	21		x-AD	22		y-AD	22		z-AD	22		x-AD
19	23		y-AD	23		z-AD	23		x-AD	24		y-AD	24		z-AD	24
20	aux	7		x-dac	7		y-dac	7		z-dac	7		x-AD	25		
21	y-AD	25		z-AD	25		x-AD	26		y-AD	26		z-AD	26		x-AD
22	27		y-AD	27		z-AD	27		x-AD	28		y-AD	28		z-AD	28
23	aux	8		x-dac	8		y-dac	8		z-dac	8		x-AD	29		
24	y-AD	29		z-AD	29		x-AD	30		y-AD	30		z-AD	30		x-AD
25	31		y-AD	31		z-AD	31		x-AD	32		y-AD	32		z-AD	32
26	aux	9	- 0 -		x-dac	9		y-dac	9		z-dac	9		x-AD	%%	
27	y-AD	%%		z-AD	%%		x-AD	%&		y-AD	%&		z-AD	%&		x-AD
28	%'		y-AD	%'		z-AD	%'		x-AD	36		y-AD	36		z-AD	36
29	aux	10	- 0 -		x-dac	10		y-dac	10		z-dac	10		x-AD	37	
30	y-AD	37		z-AD	37		x-AD	38		y-AD	38		z-AD	38		x-AD
31	39		y-AD	39		z-AD	39		x-AD	40		y-AD	40		z-AD	40
32	aux	11	- 0 -		x-dac	11		y-dac	11		z-dac	11		x-AD	41	
33	y-AD	41		z-AD	41		x-AD	42		y-AD	42		z-AD	42		x-AD
34	&%		y-AD	&%		z-AD	&%		x-AD	&&		y-AD	&&		z-AD	&&
35	aux	12	- 0 -		x-dac	12		y-dac	12		z-dac	12		x-AD	&'	
36	y-AD	&'		z-AD	&'		x-AD	46		y-AD	46		z-AD	46		x-AD
37	47		y-AD	47		z-AD	47		x-AD	48		y-AD	48		z-AD	48
38	aux	13	- 0 -		x-dac	13		y-dac	13		z-dac	13		x-AD	49	
39	y-AD	49		z-AD	49		x-AD	50		y-AD	50		z-AD	50		x-AD
40	51		y-AD	51		z-AD	51		x-AD	52		y-AD	52		z-AD	52
41	aux	14	- 0 -		x-dac	14		y-dac	14		z-dac	14		x-AD	'%	
42	y-AD	'%		z-AD	'%		x-AD	'&		y-AD	'&		z-AD	'&		x-AD
43	''		y-AD	''		z-AD	''		x-AD	56		y-AD	56		z-AD	56
44	aux	15	- 0 -		x-dac	15		y-dac	15		z-dac	15		x-AD	57	
45	y-AD	57		z-AD	57		x-AD	58		y-AD	58		z-AD	58		x-AD
46	59		y-AD	59		z-AD	59		x-AD	60		y-AD	60		z-AD	60
47	aux	16	- 0 -		x-dac	16		y-dac	16		z-dac	16		x-AD	61	
48	y-AD	61		z-AD	61		x-AD	62		y-AD	62		z-AD	62		x-AD
49	63		y-AD	63		z-AD	63		x-AD	64		y-AD	64		z-AD	64
								...								
110	aux	37	- 0 -		x-dac	37		y-dac	37		z-dac	37		x-AD	145	
111	y-AD	145		z-AD	145		x-AD	146		y-AD	146		z-AD	146		x-AD
112	147		y-AD	147		z-AD	147		x-AD	148		y-AD	148		z-AD	148
113	aux	38	- 0 -		x-dac	38		y-dac	38		z-dac	38		x-AD	149	
114	y-AD	149		z-AD	149		x-AD	150		y-AD	150		z-AD	150		x-AD
115	151		y-AD	151		z-AD	151		x-AD	152		y-AD	152		z-AD	152
116	aux	39	- 0 -		x-dac	39		y-dac	39		z-dac	39		x-AD	153	
117	y-AD	153		z-AD	153		x-AD	154		y-AD	154		z-AD	154		x-AD
118	155		y-AD	155		z-AD	155		x-AD	156		y-AD	156		z-AD	156
119	aux	40	- 0 -		x-dac	40		y-dac	40		z-dac	40		x-AD	157	
120	y-AD	157		z-AD	157		x-AD	158		y-AD	158		z-AD	158		x-AD
121	159		y-AD	159		z-AD	159		x-AD	160		y-AD	160		z-AD	160
122	-- spare --		-- spare --		-- spare --		-- spare --		-- spare --		-- spare --		MSB-CRC		LSB-CRC	

Figure 4.7: Example data packet from CASSIOPE/e-POP. Orange cells contain metadata such as packet identifiers (DLE and STX), packet counters (PID), the length of the data packet (MSB/LSB length), error detections (MSB/LSB CRC) and state of health information (aux). The feedback values for each component (DAC) are shown in grey. The sampled values (AD) for the X, Y, and Z components are shown in green, blue and yellow respectively. [J. R. Bennest, Personal Communication, 2007]

4.5.4 Deployment on a Boom

The two three-axis FGM sensors are designed to be deployed at various lengths away from the spacecraft along a boom to minimize the noise or bias caused by other electronics or magnetic materials on the spacecraft. This also provides measurements at two different distances from the spacecraft to estimate the noise of the spacecraft. The FGM's drive frequency may also be visible to any SCM on the mission so the FGM and SCM should be mounted as far apart as practical. Often, this is implemented using two booms on opposite sides of the spacecraft. If required, alternative mounting arrangements for the FGM can be considered especially if the FGM is considered as a secondary payload. Mounting two magnetometers on one boom, having magnetometers mounted on solar panels, etc., can be explored as required to provide some science measurements without affecting the primary payloads. In the worst case, and with considerable loss of measurement fidelity, the booms can be omitted but this is not usually an appropriate design solution for a dedicated science mission. The exact length of the boom required to meet the design requirements of the signal to noise ratio will vary from mission to mission. Here we simply assume that the sensors will be boom mounted.

4.5.5 Thermal Interface

Each FGM sensor would be effectively thermally isolated when mounted on the boom. Early analysis for ORBITALS suggested that passive thermal Multi Layer Insulation (MLI) blanketing and the dissipation of ∼100 mW driving the ring-cores is sufficient to maintain the FGM sensor to within its operating temperature range [Moffat & Girard, 2011]. Consequently, the design presented here assumes that there will be no survival heaters for the FGM. Other missions, especially those with shorter or more thermally conductive booms, should evaluate whether survival heaters are required.

The FGM electronics box is assumed to be mounted with good thermal contact to the spacecraft bus. Each FGM electronics card is thermally mated to the aluminium electronics box along the card edges and via aluminium stand-offs and bolts. Analysis for the earlier e-POP suggested that self-heating and thermal conduction was sufficient to maintain each FGM electronics card within its operating temperature range. This analysis should be repeated for the new design before flight hardware is manufactured.

Each FGM instrument maintains a thermally isolated, temperature controlled Zener diode as an ultra-stable voltage reference. Since the Zener diode's temperature is managed by the instrument, from the point of view of a thermal model it can be considered to be a constant temperature point with a finite power output. The thermal analysis of the FGM sensor and electronics box should be repeated once the printed circuit board layout is finalized, probably during the preliminary design phase of a future mission.

4.6 Operating Modes

Each FGM unit currently has only one operational mode; it automatically generates and telemeters data when powered on. Future firmware control will provide two configurable data cadences (128 sps and 32 sps) for the baseline design. However, the only difference is the degree to which the measurements are down-sampled to form the science data. Other operational modes could be added to provide diagnostic or firmware update functions. In-flight calibration is done in post-processing using normal science data and does not require a mode change. There are also three non-operating contingency modes to protect the instrument and the spacecraft in the event of an instrument failure or adverse on-orbit conditions. The operating and non-operating modes are described below.

4.6.1 Nominal Operation

Each FGM unit continuously generates a periodic drive signal, which is sent into its two drive coils. The output of each sense coil is conditioned and digitized as described in 4.9.1. Each FGM unit constructs data packets composed of three axes of magnetic field data, state of health, housekeeping, formatting and error correction information.

The FGM is designed to require minimal user intervention once deployed. The FGM will continually measure the magnetic field providing information about low frequency magnetic waves up to the Nyquist frequency (the maximum theoretically resolvable frequency, defined by half the sampling frequency). Data will be sent in structured packets to the spacecraft bus to be telemetered to the ground.

Ground-based data processing will then apply the known calibration data for the instrument to account for offset, sensitivity, orthogonality, and cross-talk of the sensor axes. The spin of the spacecraft is then fit to the data to attempt to remove it and the data are transformed from the spacecraft frame to a geomagnetic frame. Finally, automated algorithms archive and index the data to allow the science team to browse, download, and visualise the magnetic measurements.

4.6.2 In-Flight Calibration

The FGM does not currently implement any active in-flight calibration. The standard science data will be analysed in post-processing to estimate changes in the instrument performance. More complex in-flight calibration involving step response and linearity, are possible but would require significantly more complex firmware and an operational mode change. The risk and benefit of such calibration should be assessed for future applications of the instrument.

The FGM will be calibrated against an accepted magnetic reference before flight to fully characterise the response of the instrument. Once on-orbit, changes in an instrument's performance cannot be measured directly but must be inferred from its measurements of environmental magnetic signals. For example, instrument offset can be estimated by using the spin of the spacecraft to invert the sensor with respect to the local geomagnetic

field and applying the technique described in Section 5.5.4. Similarly, magnetic wave measurements in the overlapping frequency range between the two FGM units and the SCM can be used to measured relative changes in instrument sensitivity. However, these comparisons cannot estimate the absolute calibration of any of the instruments.

4.6.3 Contingency Operation

The FGM has three simple contingency modes designed to protect the instrument against errors in the nominal 28 ± 6 V power supply from the spacecraft and protect the spacecraft from excessive current draw by the instrument. The threshold voltages in the power supply are determined using the reverse breakdown voltages of selected Zener diodes and differ slightly from the ideal values based on the availability of parts.

Under voltage When the input voltage is less than 23 Volts (∼28 V - 6 V) the FGM power converter holds itself off, thereby disabling the unit. A threshold of 20 Volts is used when the instrument is on to prevent hysteresis due to changes in the input voltage when is loaded by the instrument turning on;

Overvoltage If the input voltage exceeds 35 Volts (∼28 V + 6 V) the FGM power converter turns itself off, disabling the unit and protecting it from damage; and

Overcurrent The FGM power converter has a soft-current limit where, when the input current passes a configurable threshold, the internally regulated voltages will decrease until the input current falls back below the soft-current limit. This protects the spacecraft by limited the maximum possible current draw by the instrument without using a fuse or circuit breaker. The instrument can survive indefinitely with its soft current limit active but it will not operate reliably.

4.6.4 Startup and Shutdown

An FGM unit is not a state-dependent instrument and has no diagnostics or calibrations to perform on startup. Therefore, the FGM payload has no turn-on or turn-off constraints.

4.6.5 Failure Mode Mitigation

The FGM payload is designed to not propagate failures to other instruments or the spacecraft. More specifically:

- The FGM is able to be shut down by the spacecraft at any time without warning;
- The FGM implements a current limit to constrain the amount of current that can be drawn from the spacecraft; and
- The two FGM instruments are synchronized to prevent mutual interference. The synchronizing electronics are redundant and either instrument can operate independently should the other instrument fail.

4.7 Trade Off Studies and Design Choices

Several trade off studies were undertaken to evaluate what design techniques should be used for the ORBITALS application. These ranged from high level questions such as "should the instrument have the same resolution in a large magnetic field as in a small magnetic field" to the science related such as "what frequency should be used to excite the sensor" to the technological such as, "what microchip should be used for the on-orbit data processing".

There are too many requirements on the fluxgate magnetometer payload (Chapter 2) for it to be practical to assess the impact of each possible design option on every requirement. Table 4.1 summarises the mission requirements (Section 2.2.3) and constraints (Section 2.3.7) of the ORBITALS mission and highlights those that have the highest impact on either the quality of the science data or the accommodation of the instrument on the spacecraft.

Parameters	Requirement	Impact
Resolution	< 0.1 nT	Critical
Cadence	≥ 128 sps	
AC Range	≥ 10 Hz	
Noise Floor	≤ 20 pT/$\sqrt{\text{Hz}}$ at 1 Hz	Critical
Phase Response	$\leq \pm 180^0$ (0 - 10 Hz)	
Amplitude Accuracy	$\leq 0.1\%$	
Timing Accuracy	≤ 40 μs	
FGM/EFW Timing	≤ 0.2 ms (40 μs goal)	
Peak Power (2 units)	≤ 5 W	Critical
Electronics Mass	≤ 5 kg	Critical
Electronics Dimensions	$\leq$ 150x150x100 mm	
Sensor Heat Generation	≤ 100 mW	
Average Telemetry Rate	≤ 6.8 kbps	
Electromagnetic Cleanliness (EMC)	TBD	
Total Integrated Dose (TID)	≥ 100 krad	Critical
Radiation Shielding	$\geq 7 + 1$ mm Al	
Single Event Threshold	≥ 35 LET	
Sensor Survival Temp	-55 to $+85^o$c	
Sensor Operating Temp	-40 to $+60^o$c	
Electronics Survival Temp	-55 to $+85^o$c	
Electronics Operating Temp	-40 to $+50^o$c	
Dual FGM units	Fully Independent	
18 Month Reliability	≥ 0.978 for payload	
Storm Operation	Operate During	
Product Assurance	TBD	

Table 4.1: Summary of instrument requirements derived from the mission requirements (Section 2.2.3) and constraints (Section 2.3.7).

The five critical parameters of measurement resolution, noise floor, power consumption, mass, and radiation tolerance were used to inform the trade-of studies and design

choices for the prototype instrument presented here. These parameters are refereed to as the 'technical performance metrics' in systems engineering and are used to summarise how a design performs compared to its requirements. Table 4.2 shows the technical performance metrics for the ORBITALS and PRIMO fluxgate magnetometer payload. For example, the resolution of the instrument must be less smaller than 100 pT and has no minimum specification.

Parameter	Unit	Min	Max
Magnetic Resolution	pT	N/A	100
Magnetic Noise	pT/$\sqrt{\text{Hz}}$ at 1 Hz	N/A	20
Total Power Consumption	W	N/A	5.0
Total Mass	kg	N/A	4.6
Radiation Tolerance	krad	100	N/A

Table 4.2: Technical performance metrics and current values.

4.7.1 Offsetting Versus Gain Ranging

The operation of the FGM would be comparatively simple if the resolution requirement could be met by simply digitising the sensor with an ADC. The magnetic range of the instrument was set to ± 65,536 nT to cover the expected geomagnetic field experienced in space and during ground testing. Resolving 0.1 nT on this field would require (2 · 65,536 nT) / 0.1 nT = 1,310,720 possible values or a 21 bit ADC. A survey of 100 krad tolerant Class S ADCs was completed and the highest resolution digitizer available was 16 bit RH1604, the radiation tolerant version of the Linear Technology LTC1604 commercial part. The next highest resolution device available was the 14-bit RAD1419, the radiation tolerant version of the Linear Technology LT1419 commercial part.

There are two possible design techniques that could be used to restore 24 bits of resolution. In an offsetting instrument [e.g. design by Wallis et al., 2006], a precise offset is created and applied to the sensor to oppose the main field. The full datum is then the digital sum of the applied offset and the measured residual signal. In a gain ranging instrument [e.g. design by Kletzing, 2011], the overall instrument sensitivity (gain) is configurable and is changed periodically to keep the measurement within the digitization range. With gain ranging, the instrument has lower resolution when the absolute field strength is large.

A gain ranging design has 16 bit precision to digitise the entire local magnetic field. A 16 bit ADC with the least significant bit set to 0.1 nT resolution can resolve a maximum field strength of

$$0.1 \text{ nT} \cdot \frac{2^{16}}{2} = \pm 3,277 \text{ nT} \tag{4.1}$$

In a larger field, the least significant but must be made coarser to expand the measurement range of the instrument. For example, when the instrument is operated on the ground where the field is large it would be in its coarsest mode. In order to span the ±65,536 nT main field it would need to set its resolution to

$$\frac{\pm 65,536 \text{ nT}}{2^{16}} = 2 \text{ nT} \tag{4.2}$$

Consequently, gain ranging can only meet the 0.1 nT resolution requirement defined in Section 2.2.3 when the local magnetic field is small (below 3,277 nT).

An offsetting design would allow the instrument to meet its resolution requirement regardless of the local magnetic field strength and hence at all points in any of the candidate orbits. This also allows the instrument to meet its resolution in the magnetic field at the Earth's surface simplifying design, testing and calibration. However, offsetting requires a stable, noise free but variable offset signal to avoid introducing an error. A highly stable reference voltage and a very low noise DAC are required to create such an offset. The offsetting design is the superior solution if it can be achieved using sufficiently radiation tolerant parts.

Early development work for the ORBITALS FGM included a proof of concept high precision, thermally stabilized Zener voltage reference and DAC based on a PWM. Based on these successful technology demonstrations, the prototype FGM presented here is designed as an offsetting instrument. The detailed implementation of the PWM DAC and reference are provided in Sections 4.9.4 and 4.9.2 respectively. These subsystems have the added benefit of allowing the FGM to meet its resolution requirements in any geomagnetic field from the Earth's surface upwards. This makes it not only compatible with all the possible ORBITALS orbits but also with the magnetic field strength experienced in any Earth orbit, providing flexibility for future space missions.

4.7.2 Radiation Hardened Analog to Digital Conversion

The first iteration of the digital subsystem was designed using the highest resolution ADC available, the 16 bit LTC1604. However, subsequently available test results by Irom [2006] for the RH1604 suggested heavy ion strikes can trigger a destructive latch-up condition where the chip gets stuck in a non-operating mode, draws excessive power, and burns itself out. As a result, the 16 bit RH1604 has been replaced with the 14 bit RAD1419 in the design presented here.

The offsetting system used to null the fluxgate sensor and produce 24 bit data products using a 14-bit converter would nominally require a DAC with 10 bits of resolution. However, the fluxgate signal is superimposed on a large amplitude residual of the drive frequency, requiring the input range of the ADC to be set four times (2 bits) wider to prevent saturation. Most digital to analog converters are noisy at slightly less than the resolution of their Least Significant Bit (LSB). However, in the offsetting design, the DAC only requires $\sim$12 bits of resolution but must be stable and quiet at the 24 bit level to avoid being the dominant noise source in the error signal. During the development work for ORBITALS, a survey of 100 krad DACs was completed and none was found to be suitable for this application. As a result, the FGM has a custom DAC developed using two summed PWM signals.

The PWM repetition rate needs to be at least an order of magnitude above the maximum operating frequency of the magnetometer for the analog filters to sufficiently

attenuate the fundamental PWM tone such that it does not saturate the ADC. This leads to a 12 bit PWM with a repetition rate around 14,400 Hz, which would require a $14,400 \cdot 2^{12} = 50$ MHz clock. Unfortunately, the best 100 krad analog switches available cannot switch above 20 MHz. However, the DAC can be built up from two, 10 bit PWMs at a 14,400 Hz repetition rate, which are scaled and summed using a resistor array. The summing network needs to be built from precision, ultra-low temperature co-efficient resistors to sum the signals accurately and to avoid introducing temperature dependence. The only known manufacturer of such resistors is Vishay.

The precision Vishay resistors are not specifically sold as radiation tolerant, so the manufacturer was asked to provide test data on their susceptibility to radiation TID. Vishay provided radiation test data for their RNC90 product, which uses the same bulk foil technology for the resistive element. In the test data [B. Demers, Personal Communication, 2011] showed no measurable change in resistance up to 100 Mrad of dosage. This suggests that the 100 krad dosage should have no impact on the Vishay high-precision resistors.

Two PWMs summed with precision resistors provide a way to achieve 24 bits of resolution in the FGM using parts that meet the 100 krad radiation design requirement. The summed PWMs generate a 16 bit offset that is stable and noise free to 24 bits. The offset is used to null the magnetic field in the fluxgate sensor and a 14 bit ADC captures the resulting error signal. The appropriately scaled sum of the two PWMs and the error signal reconstitutes the full 24 bit measurement of the magnetic field. This design solution was implemented in the prototype instrument presented in this thesis.

4.7.3 Radiation Tolerant FPGA Controller

The prototype FGM uses a low-cost Altera EP3C40F324 commercial reprogrammable FPGA because the UAlberta Department of Physics electronics shop had previous experience and development tools for this product line. The planned flight FPGA is the Actel RTAX250 300 krad tolerant single time programmable FPGA. The current firmware is written in standard Verilog hardware description language, which is supported by both types of FPGA. It is possible to synthesize the current operational firmware against the Actel target to estimate the amount of FPGA capacity required in the flight FPGA. The internal Random Access Memory (RAM) structures of the two FPGAs are sufficiently different that code modification will be required in order for the RAM allocation to synthesize correctly. However, the unmodified synthesis provides a useful rough measure of device utilization.

The current prototype Verilog firmware provides an estimated 80% coverage of the functional blocks required for final FGM digitizer. The results of synthesising code against an Actel RTAX250 target is shown in Table 4.3. The estimate for "RAM Blocks" is incorrect (zero) due to significant differences in how memory hardware is handled in the two FPGA architectures.

```
*************************************************
Device Utilization for RTAX250SCG624
*************************************************
Resource                Used    Avail    Utilization
-------------------------------------------------
IOs                     59      248          23.79%
Modules                 1122    4224         26.56%
Sequential modules      410     1408         29.12%
Combinational modules   704     2816         25.00%
Global HCLKs            0       4             0.00%
Global RCLKs            3       4            75.00%
RAM Blocks              0       12            0.00%
-------------------------------------------------
```

Table 4.3: Verilog synthesis results for a rad-hard RTAX250 target.

The current firmware is therefore estimated to use roughly 30% of the RTAX250 resources. The fully implemented firmware is therefore expected to consume approximately $\frac{30\%}{0.8} = 40\%$ of the FPGA. This usage level is consistent with design practices, which recommend the preservation of a 50% margin to allow for future modifications. However, the Actel RTAX product family allows the flight FPGA selection to be deferred to later in the development cycle when the flight firmware is more complete. The RTAX family currently includes four options as shown in Figure 4.8.

Device	RTAX250S/SL	RTAX1000S/SL	RTAX2000S/SL	RTAX4000S/SL
Capacity				
Equivalent System Gates	250,000	1,000,000	2,000,000	4,000,000
ASIC Gates	30,000	125,000	250,000	500,000
Modules				
Register (R-cells)	1,408	6,048	10,752	20,160
Combinatorial (C-cells)	2,816	12,096	21,504	42,840
Flip-Flops (maximum)	2,816	12,096	21,504	42,840
Embedded RAM/FIFO (without EDAC)				
Core RAM Blocks	12	36	64	120
Core RAM Bits (k=1,024)	54 k	162 k	288 k	540 k
Clocks (segmentable)				
Hardwired	4	4	4	4
Routed	4	4	4	4
I/Os				
I/O Banks	8	8	8	8
User I/Os (maximum)	248	418	684	840
I/O Registers	744	1,548	2,052	2,520
Speed Grades	Std., -1	Std., -1	Std., -1	Std., -1
Temperature Grades	E, B, EV*	E, B, EV*	E, B, EV*	E, B, EV*
Package				
CCGA/LGA	624	624	624, 1152	1272
CQFP	208, 352	352	256, 352	352

Figure 4.8: Actel RTAX radiation hardened product line. Taken from `http://www.actel.com/products/milaero/rtaxs/`

"Equivalent system gates" is a measure of FPGA capacity and shows that up to 16 times more capacity is available from the larger chips in the Actel RTAX product family.

The four chips are footprint compatible using the CCGA-624 or CQFP-352 footprint, so the specific FPGA could be changed without modifying the printed circuit board. The FGM design assumes that an Actel RTAX FPGA from this family of chips will ultimately be selected for the flight hardware. The specific chip will be selected once the firmware is more complete. Unfortunately, the Altera and Actel product lines are not foot-print compatible so a different printed circuit board layout will be required for the flight hardware.

4.7.4 Drive Frequency

The FGM excites its sensor with a series of current pulses into the drive winding on the permalloy sensor cores. The drive winding is toroidal to minimize the radiated signal. However, the FGM sensor still broadcasts a magnetic signal at its drive frequency. The CASSIOPE/e-POP MGF and early ORBITALS prototypes used a 14.4 kHz drive frequency, which is within the 20 kHz measurement bandwidth of the baseline ORBITALS design requirement for the SCM in the ORBITALS application. The FGM drive structure was therefore modified as part of the new design development to move the fundamental frequency above 20 kHz to minimize this source of magnetic interference.

The FGM prototype is designed and presented here with a doubled drive frequency of 28.8 kHz to keep all the instrument functions synchronised. This required doubling the ADC sampling rate, increasing the FPGA clock frequency to process the additional data and changing the resonance frequency of the drive winding by adjusting the tuning capacitor in the fluxgate sensor. The FGM prototype operates successfully with a 28.8 kHz drive frequency and the CASSIOPE/e-POP fluxgate sensor tolerates the faster drive with the modification of a single capacitor to update the tuning of the drive circuit. The design and test results presented in this thesis reflect the 28.8 kHz drive frequency. The most significant impact of this change is a modest increase in the power required to drive the sensor; however, the instrument still draws less than 1.5 W and is well within its 2.5 W power budget (See Section 2.3).

The faster 28.8 kHz drive frequency, after its successful demonstration in this thesis, is now the baseline configuration for the FGM. In subsequent development work for the PRIMO mission, the upper frequency goal of the SCM instrument was increased to 50 kHz. It may therefore be appropriate to double the FGM drive frequency again to 57.6 kHz to move it beyond the new SCM measurement range in a future version of the instrument; however, this is not considered in this thesis.

4.7.5 Core Selection

The FGM prototype uses a periodically saturating, low-noise 6-81 permalloy ring core to sense the local static magnetic field. Historically, the best Canadian magnetometers have been built from cores manufactured by Infinetics. These are no longer in production or available for purchase.

A limited supply of these legacy cores exists and cores have been promised for the ORBITALS FGM. The re-use of this magnetometer design for future missions will require a new source of low-noise ring cores. Narod Geophysics Ltd. in Vancouver, BC is currently undertaking research that may provide an alternative core. However, the final specifications and availability of these cores remains to be determined. In the absence of these cores, the instrument can be constructed from existing alternative lower grade cores; however, the noise floor will degrade to about 30 pT/$\sqrt{\text{Hz}}$ at 1 Hz.

The prototype fluxgate has been constructed and tested using legacy Infinetics cores on loan from Dr. Don Wallis of Magnametrics. However, the FGM prototype design will require a new supply of low-noise ring cores for future missions. This will be pursued in future development.

4.8 Selected Design Improvements

As previously noted, the prototype instrument is based on the MGF instrument developed for the CSA CASSIOPE/e-POP satellite. This section highlights some of the principal improvements that have been made to the MGF design for the ORBITALS and then the PRIMO /PCW satellite missions as part of the design development presented in this thesis.

4.8.1 Susceptibility to Ambient 60 Hz Noise.

The MGF instrument from CASSIOPE/e-POP used a 12 bit ADC chip and a slow offsetting algorithm. This design is well suited to the three axis stabilized e-POP satellite where the instrument is essentially fixed with respect to the background field and the expected rates of change of the magnetic field in the frame of the sensor are small. Unfortunately, this design limits the bandwidth of the instrument such that the 60 Hz field created by electrical wiring on Earth can saturate the ADC chips. The MGF has auxiliary 60 Hz filters, which could be firmware-selected to connect in parallel with the normal feedback circuit to reduce the 60 Hz signal by more than 35 dB. These filters allowed the MGF to operate in terrestrial 60 Hz field, but impacted the instrument's high-frequency phase linearity. This made the MGF difficult to characterise and calibrate as it could only be operated in its flight configuration, 60 Hz filters out of circuit, in a magnetic shield or a similarly magnetically quiet environment.

The new prototype instrument has a higher resolution ADC and has fast digital feedback, which can compensate for the 60 Hz field in most laboratories. This makes the instrument easier to test and develop because it can be operated normally on a laboratory bench. More importantly, it also makes the design suitable for ground deployment as it can operate in the presence of the 60 Hz field found in most ground applications in North America (50 Hz in other locations).

4.8.2 Maximum Rate of Change

The CASSIOPE/e-POP MGF is based on a ground instrument designed by Narod Geophysics Ltd. [Narod & Bennest, 1990], which uses a highly filtered reference source, high parametric gain, and a very slow offsetting algorithm to prevent instrument oscillation. This design works well for an instrument mounted in a ground station and is fixed in the Earth's field. However, as a consequence of this design, the ground instrument can take several minutes to servo into range if the sensor head is rotated 180^o with respect to the background magnetic field.

The updates for the CASSIOPE/e-POP MGF design gave the instrument a maximum rate of change (slew rate) of 3840 nT/second. However, the oscillation in the measured field after each offsetting step caused by the heavy filtering in the design would prevent the instrument from settling to a steady state value when slewing at this rate. This design works well for the three axis stabilized satellite such as the CSA's CASSIOPE/e-POP. However, the ORBITALS spinning platform results in a spin rate of up to 2800 nT/second (7000 nT maximum field in the raised perigee orbit with a 10 seconds spin period), which would prevent the CASSIOPE/e-POP MGF design from ever settling to the ambient field.

The new prototype design presented here has a usable slew rate exceeding 12,800 nT per second, which is more than sufficient for ORBITALS and many spinning spacecraft applications. Sounding rockets can spin substantially faster (typically ∼6 Hz rather than ∼0.1 Hz) and can operate at lower altitudes, which have a stronger magnetic field. These types of applications would require slew rates more than an order of magnitude faster than the current design. This could be achieved by increasing both the PWM repetition rate and the analog low-pass filter frequency, thus allowing the analog magnetometer subsystem to settle faster. This would require either a faster analog switch (although no faster 100 krad tolerant analog switches have been identified) or adding a third PWM to each component. The presently developed digital feedback design has demonstrated that the current fluxgate prototype meets the ORBITALS requirements, and has shown that significant increases in bandwidth are possible in principle for future missions.

4.8.3 Temperature Compensation

The sense windings in any fluxgate magnetometer sensor will expand and contract slightly with temperature. Unless compensated for, this will change the area of the coil and give the instrument a temperature dependent sensitivity. This temperature effect can be compensated using an unbalanced transconductance amplifier and balancing the temperature dependent change in coil impedance against the change in coil area. This technique has been used in magnetometers developed by Acuña [Acuña et al., 1978] and Narod Geophysics Ltd [Narod & Bennest, 1990]. However, it has not yet been combined with a digital magnetometer design. Section 4.9.2 shows how, for the first time, the new prototype FGM design combines the simplicity, efficiency and radiation tolerance of a digital magnetometer with the technique for analog temperature compensation of the fluxgate sensor developed by Acuña et al. [1978].

4.8.4 100 krad Radiation Hardening

The CASSIOPE/e-POP MGF instrument was built from commercial parts and had limited radiation tolerance and testing (see Section 3.2.1). The ORBITALS mission has a significantly larger expected radiation dose due primarily to the significant time it spends in the Van Allen radiation belts because of its orbit. ORBITALS requires space grade (Class-S) parts with a minimum radiation tolerance of 100 krad (see Section 2.3.3).

A prototype constructed from these parts would have been prohibitively expensive for a Phase A concept study. For example, an operational amplifier that is worth less than $10 in a commercial grade costs over $1,000 as a Class-S, 100 krad grade component. Space grade parts can also have purchasing lead-times on the order of a year making them impractical on the time scales of a Master's thesis.

To reconcile these conflicting requirements, the FGM prototype was constructed from commercial parts that are functionally equivalent to available 100 krad Class-S parts. Where possible, parts with equivalent or similar footprints have been used. For example, Table 4.4 shows the critical components for the digital electronics card (developed in collaboration with the Department of Physics Electronics Shop). The table shows the commercial parts used in the prototype, the equivalent 100 krad Class-S part and the purpose of the component within the instrument.

Commercial Part	Radhard Equivalent	Description
EP3C40F324	RTAX250S/SL	Program once FPGA, Actel
EPCS16SI8N	W28C0108	EEPROM, Northrop Grummand
ZXMP6A17E6	IRHLUBC7970Z4	PMOSFET, International Rectifier
ZXMN10B08E6	IRHLG77110	NMOSFET, International Rectifier
1N5819HW	SS5819UR-1	DIODE, Sensitron
LT1009IDR	RH1009M	2.5V Voltage Ref, Linear Technology
LT1671CS8	RH1011	Comparator, Linear Technology
74HCT541	HCTS541MS	Buffer, Intersil
CB3LV-3C-3M6864	2101R3M68640BAS	TCXO, Vectron
MAX3160	HS26CLV31	RS422 transceiver, Intersil
LT1007CS8	RH1499M	Opamp, Linear Technology
ADG619BRTZ	HS303ARH	Analog Switch, Intersil
LTC1419	RAD1419	ADC, Radiation Assured Devices

Table 4.4: Selected commercial parts and radhard equivalents.

Building the prototype from equivalent commercial parts allowed the full instrument to be prototyped and tested in Phase A rather than Phase B or Phase C as in most missions. Another advantage of this process is that the prototype instrument, being constructed from low-cost commercial grade parts, could be mass manufactured in the future for sounding rocket or ground applications where the expected radiation dose is negligible.

4.8.5 Size and Parts Count

The direct sensor digitisation and digital feedback in the developed prototype have removed the need for most of the analog electronics found in the earlier e-POP MGF [Wallis et al., 2006] and the Narod Geophysics Ltd. ground instrument [Narod & Bennest, 1990]. The FPGA has also replaced most of the discrete digital logic required in the earlier designs. Figure 4.9 shows the relative size of the original Narod Geophysics Ltd. electronics (a), the new prototype electronics (b), and an example sensor head (c). (to scale)

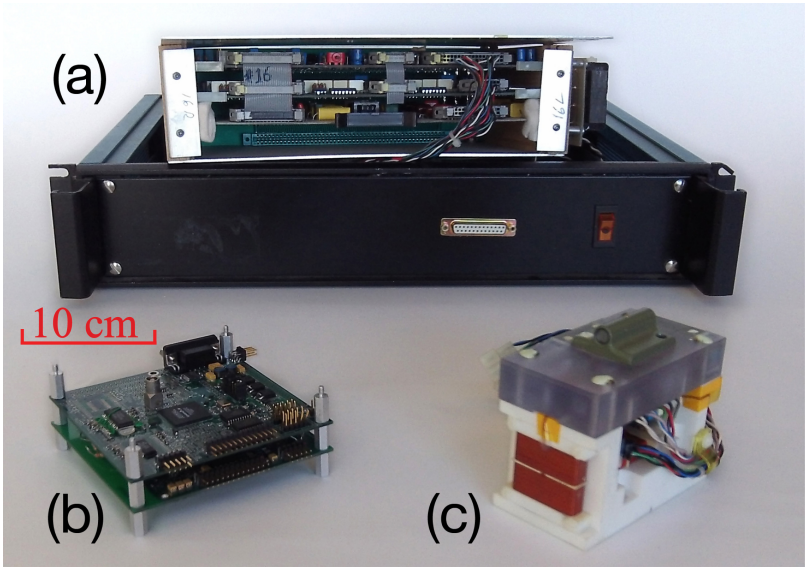

Figure 4.9: Relative size of the original Narod Geophysics Ltd. electronics (a), the prototype electronics (b), and an example sensor head (c). (to scale)

The prototype developed here was built for testing from two cards to reduce the time and cost of successive hardware revisions and there is sufficient spare printed circuit board area to combine the two cards into a single card of the same geometry for the final flight model.

Although the prototype has a significantly lower parts count than the CASSIOPE e-POP MGF, the final physical dimensions of the electronics will be approximately equal. The 100 krad, Class-S parts are generally large ceramic packages and metal cans designed to be easily opened and inspected during qualification testing. The parts used in the CASSIOPE/e-POP MGF are smaller plastic encapsulated parts that, due to the minimal testing required for commercial grade parts, do not need to be opened for visual inspection.

4.9 Detailed Implementation of Selected Subsystems

Several subsystems of the prototype fluxgate are described in further detail in this section to illustrate the type of design work that was undertaken in the course of this

thesis. The discussed topics are:

- How information is extracted from the fluxgate sensor (Section 4.9.1);
- The use of PWM to create a stable, temperature compensated feedback source (Section 4.9.2);
- The control loop logic for the digital feedback (Section 4.9.3); and
- The construction of a radiation hardened reference source for the instrument (Section 4.9.4).

4.9.1 Extracting Information from the fluxgate Sensor

The prototype fluxgate uses digital processing in a FPGA controller for most of the signal processing required to extract fluxgate data from the sensor. However, some minimal signal conditioning is required before the signal can be digitised.

The fluxgate induction equation (Equation 3.5) relates the voltage across the sense coil to the local magnetic field H. However, it is equally meaningful, and often more useful, to think in terms of the current generated by the coil. Figure 4.10 shows the result of short-circuiting the sense coil by connecting both ends of the coil to ground. R_{wire} is a lumped resistance used to account mathematically for the resistance of the copper wire in the coil.

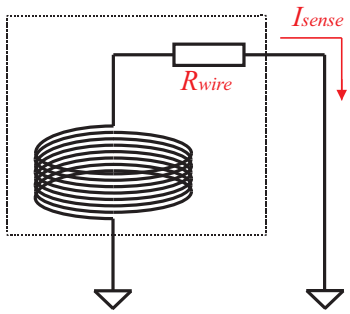

Figure 4.10: Equivalent circuit of a the sense coil in a short-circuit. R_{wire} is a lumped resistance to account for the finite conductance of the copper wire in the sense coil.

The voltage across the coil is forced to zero by the short circuit; however, there is still a circulating current determined by ohms law where V_i is the unloaded coil voltage.

$$I_{sense} = \frac{V_i}{R_{wire}} \tag{4.3}$$

Substituting the fluxgate induction equation from Equation 3.5 gives

$$I_{sense} = \frac{(NA\mu_0 H)\,\frac{d\mu_r}{dt}}{R_{wire}} \tag{4.4}$$

Holding the coil in a short-circuit has the advantage of linearising the coil response by suppressing self-resonance. In practice, the sense coil is connected to a virtual ground point provided by the inverting input of an operational amplifier. Figure 4.11 shows an equivalent circuit for this pre-amplifier configuration.

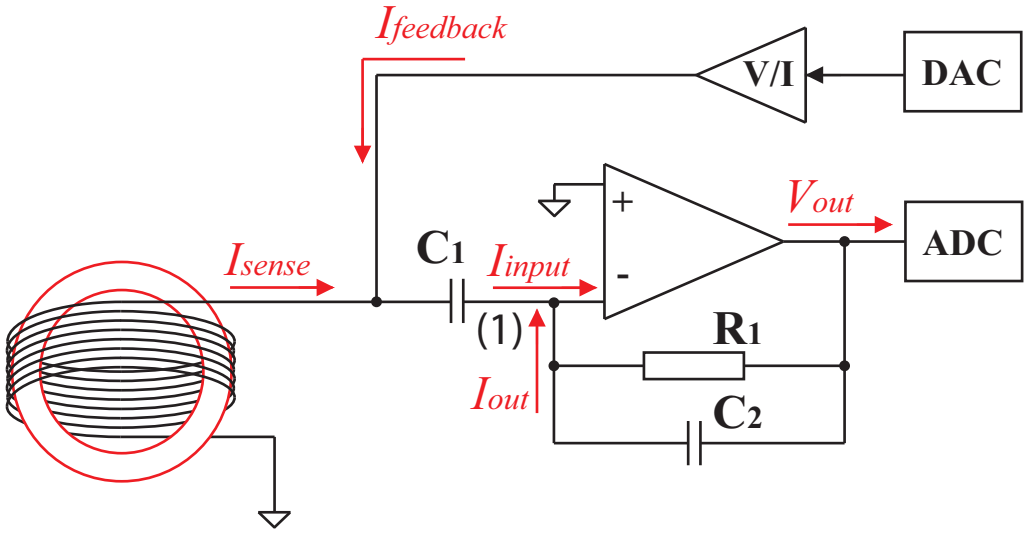

Figure 4.11: Equivalent circuit of the sensor preamplifier design.

The operational amplifier is configured as a transimpedance amplifier (current to voltage converter) and is selected to be approximated by the ideal amplifier assumptions (zero input current, zero offset, arbitrarily large gain). As the net current at the inverting input must be zero, Kirchhoff's current law analysis at node (1) shows that

$$I_{net} = I_{sense} + I_{input} + I_{out} = 0 \tag{4.5}$$

The input current to the amplifier is essentially zero ($I_{input} = 0$). The capacitor C_1 is selected such that it passes the second harmonic AC fluxgate signal but blocks the quasi-static signal from the feedback DAC so $I_{feedback} = 0$ at the 2f frequency (twice the drive frequency, F). C_2 keeps the amplifier from oscillating and suppresses high frequency noise but doesn't pass significant current at the $2f$ frequency. I_{out} can be re-written using ohms law ($I_{out} = V_{out}/R_1$). Making these substitutions give

$$0 = I_{sense} + I_{input} + I_{out} + I_{feedback} \tag{4.6}$$

$$0 = I_{sense} + 0 + \frac{V_{out}}{R_1} + 0 \tag{4.7}$$

$$V_{out} = -R_1 \cdot I_{sense} \tag{4.8}$$

I_{sense} from the fluxgate sensor is balanced by I_{out} from the amplifier feedback. Finally, substitution for I_{sense} using 4.4 gives

$$V_{out} = -\frac{R_1}{R_{wire}} N A \mu_0 H \frac{d\mu_r}{dt} \tag{4.9}$$

The pre-amplifier therefore provides a voltage V_{out} that is proportional to the instantaneous fluxgate action $\frac{d\mu_r}{dt}$, provides configurable gain via resistor R_1 and is a low-impedance output, which can be digitised without loading and distorting the source.

The V_{out} signal is composed of the $\frac{d\mu_r}{dt}$ fluxgate action at the 2f frequency and the transformer coupled harmonics of the drive signal at f, 2f, etc. The fluxgate action will cause V_{out} to pulse at 2f in proportion to the local magnetic field. However, these pulses will be superimposed on the constant, phase locked f and 2f residuals of the drive signal. This is most easily visualised using a Fast Fourier Transform (FFT) amplitude spectrum. Figure 4.12 shows a spectral plot of V_{out}. The fluxgate sensor was placed in a solenoid in a magnetic shield (see Section 5.1 for details of the experimental setup). Static magnetic fields of -7,048, -1,695, 0, +1,785, and +7,137 nT (panels left to right) were applied using the solenoid and the resulting error signal was captured using a bench top spectrum analyser. Note how the different magnetic fields modulate the amplitude of the 2f major carrier via the fluxgate action. However, the 2f carrier is present even when the field is zero due to the residual drive signal.

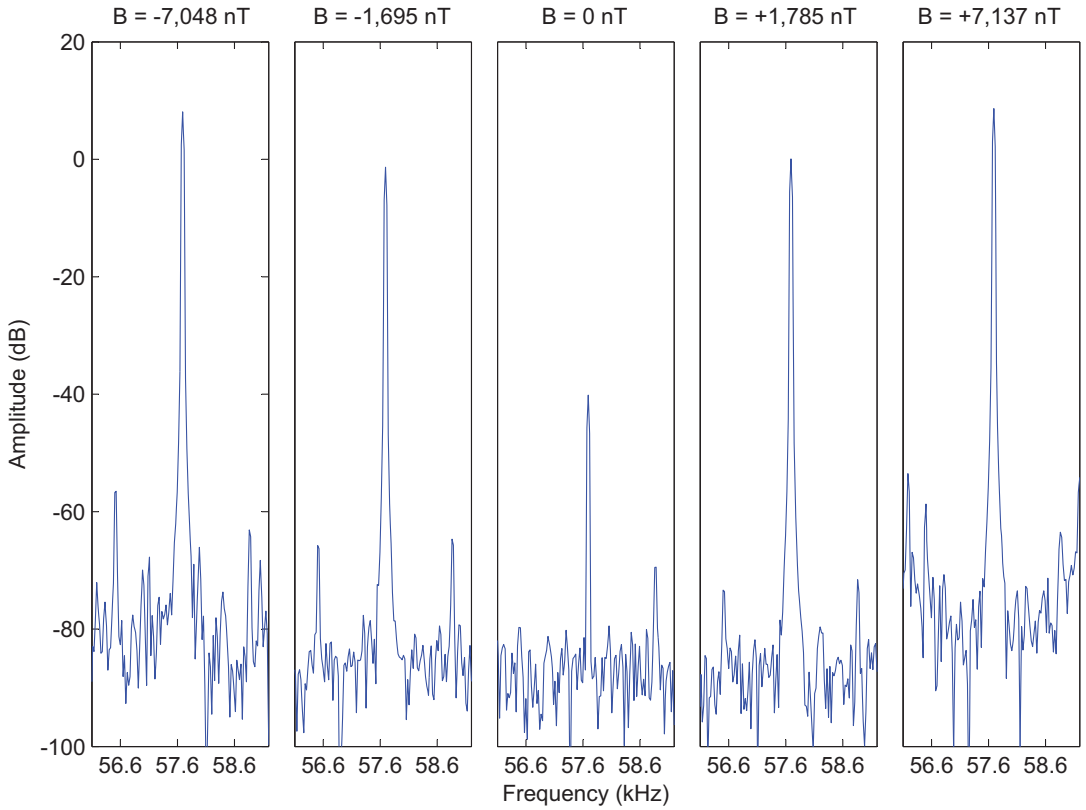

Figure 4.12: Modulation of the 2f major carrier at various magnetic field strengths.

Figure 4.13 shows a time series of V_{out} under different external magnetic fields. Panel (a) shows a large positive field, panel (b) shows a small positive field, panel (c) shows

a near zero field, panel (d) shows a small negative field, and panel (e) shows a large negative field. The data was collected by disabling magnetic feedback, placing the sensor in a solenoid within a magnetic shield, and applying various magnetic field strengths using the solenoid. The vertical red lines in Figure 4.13 show the trigger points, where the ADC samples V_{out}, phase locked to the $2f$ signal effectively creating a synchronous detector. The irregularity on the decreasing slope when B = +24,821 nT varies by axis and individual sensor. It is believed to be related to minor manufacturing imperfections in the sensor core.

Note how the amplitude of the $2f$ pulses, as measured at the ADC trigger points, tracks the applied magnetic field in amplitude and polarity. However, even in a nearly zero field (-65 nT), there is a residual Alternating Current (AC) signal from the drive current primarily at f and $2f$. The ADC measurements must be averaged over an even number of samples to cancel the harmonics. It is important to note that even in a strong field (+24,821 nT and -24,431 nT) the amplitude of the error signal at the ADC trigger points is monotonic and strictly increasing with magnetic field. This is essential because any local extrema or out-of-range polarity inversion would cause the control loop to apply feedback in the wrong direction.

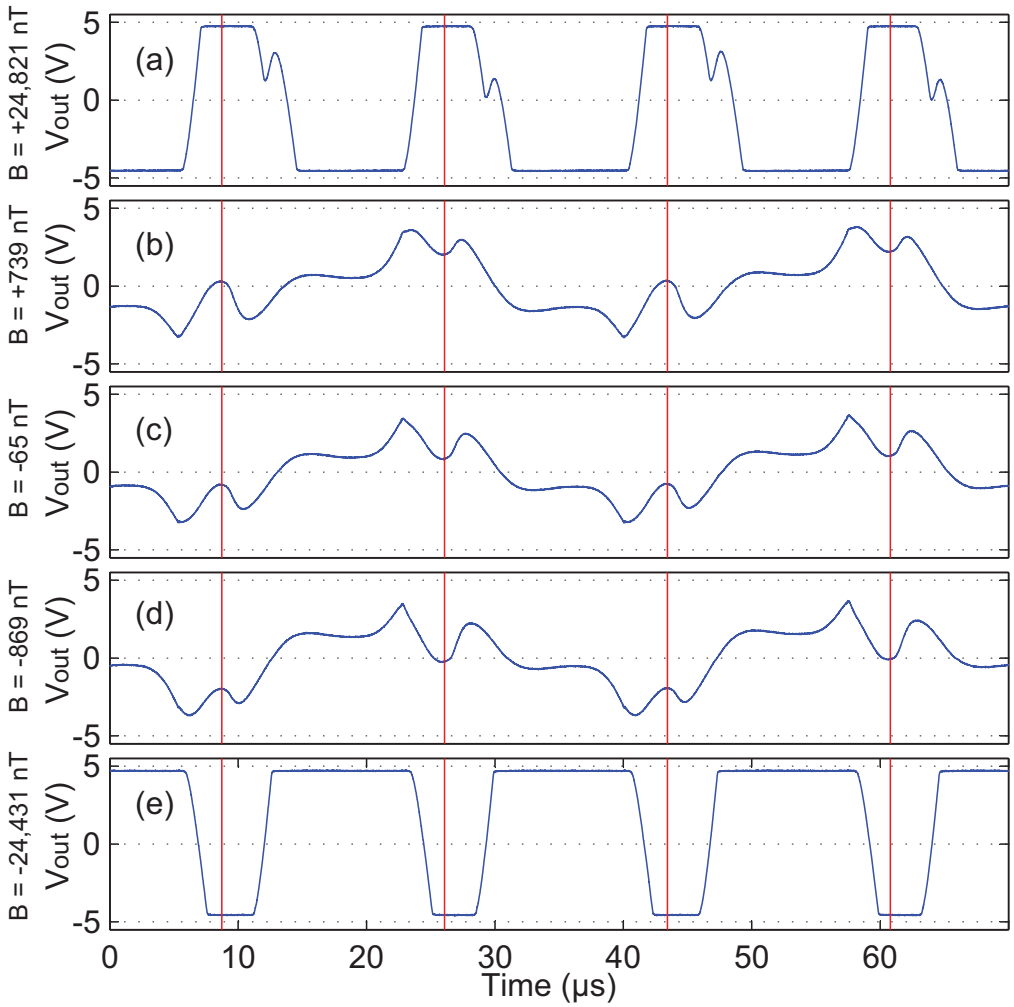

Figure 4.13: V_{out} at various applied magnetic field strengths. Vertical red lines show the ADC sampling times synchronised to pulse from the periodic saturation of the ring-core. Panel (a) shows a large positive field, panel (b) shows a small positive field, panel (c) shows a near zero field, panel (d) shows a small negative field, and panel (e) shows a large negative field.

The ADC has an input range of ± 2.5 V so it will saturate well before the ± 5 V analog signal. However, because the signal is sampling at 2f but contains a large 1f component, it is possible for the even samples to saturate while the odd samples remain in range (or vice versa). Consequently, the sensor has four saturation points: half positive saturation, full positive saturation, half negative saturation, and full negative saturation. Figure 4.14 shows the averaged digitised value of a sensor signal versus the applied magnetic field. As before, the sensor was placed in a solenoid in a magnetic shield to apply different static magnetic fields strengths. Each point is averaged over one second to suppress the local 60 Hz noise.

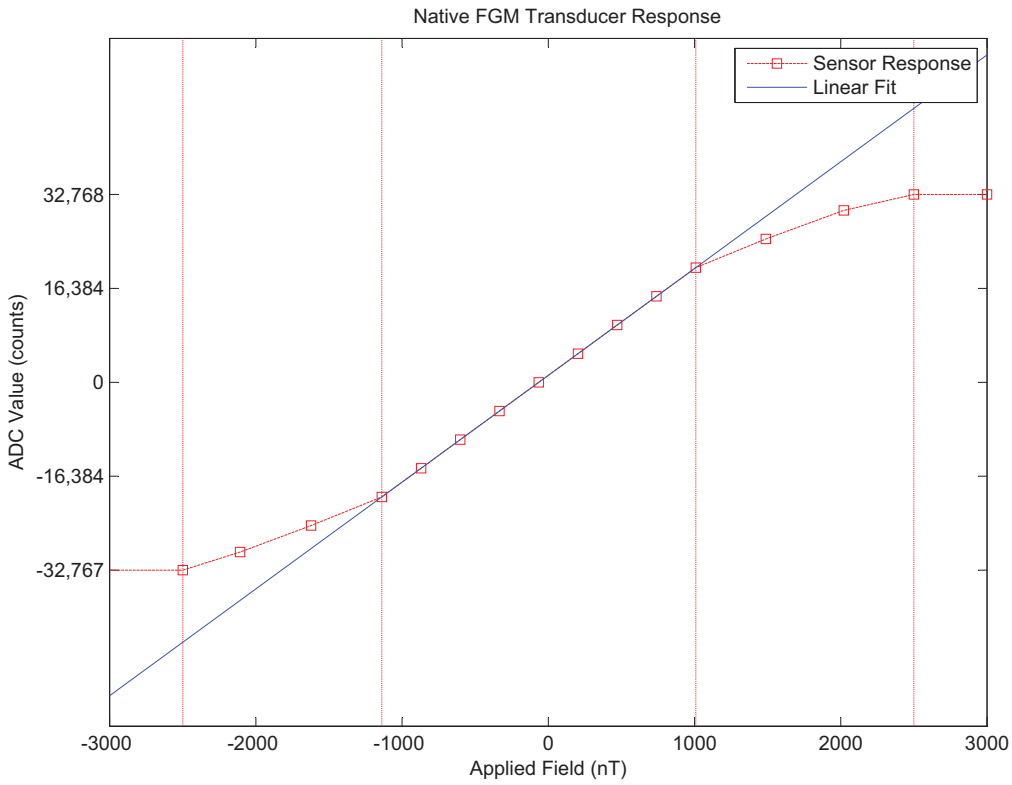

Figure 4.14: Transducer response versus applied magnetic fields. Vertical lines show approximate half and full-saturation points.

In the linear region, the transducer has a measured Root Mean Square (RMS) error of 3 nT. However, in an active sensor, the instrument feedback is constantly pushing the transducer towards zero. The effect of this RMS error will be minimized in a well-nulled sensor as the majority of the measurements will be taken in a small subset of the total linear region near zero field.

4.9.2 Dual Pulse Width Modulation Feedback

A PWM based DAC changes its average measurement by changing the duty cycle of a square wave at a fixed repetition rate. A low-pass filter is then used to remove the square wave frequency leaving only the average value. A PWM based DAC feedback system has three components:

1. A digital switch creating a variable duty cycle pulse train;
2. A low-pass filter to remove the switching frequency; and
3. A voltage to current converter to drive the feedback coil.

Some digital fluxgate magnetometers (e.g., O'Brien et al. [2007]) omit the low pass filter and simply drive the digital pulse train into the feedback coil using a resistor for current

conversion. To the first order, the resistor acts as a voltage to current converter. The average feedback current is the same and the input filters on the sensor will generally remove the switching frequency. However, a simple resistor is not a controlled current source and any change in the sensor temperature will change the impedance of the feedback coil and, consequently, the effective gain of the feedback system. This temperature effect can be compensated by using an unbalanced transconductance amplifier and balancing the change in coil impedance against the change in coil area with temperature. However, this technique requires a low-pass reconstruction filter to avoid clipping the feedback amplifier and hence requires a low-pass filter to remove the comparatively large switching signal from the PWM.

The feedback frequency range should generally be wide enough to include the sampling frequency to make the feedback control loop robust and stable. The prototype instrument samples at 900 samples per second or about 1 kHz. The low-pass reconstruction filter requires about one decade of frequency to reduce the switching signal sufficiently to avoid saturating the feedback amplifiers or about 1 kHz $\cdot$ 10 = 10 kHz. To ensure the feedback is locked in phase with the other instrument functions, the repetition rate of the PWM was set to 14,400 Hz (the next divisor of the common clock frequency).

The magnetic range of the instrument was set to $\pm$ 65,536 nT field to cover the expected geomagnetic field experience in ground and space applications. Resolving 8 pT in within this range is 16,384,000 possible values or slightly less than 2^{24} or 24 bit resolution. The best available radiation hard ADC can provide 14 bits of resolution; however, two bits are lost accommodating the switching residuals for an effective 12 bits of resolution. This requires the remaining $24 - 12 = 12$ bits of resolution to be provided by the feedback network.

The base frequency required for a simple PWM based feedback circuit could be calculates as:

$$\begin{aligned} \text{Base Frequency} &= \text{Repetition Rate} \cdot \text{Possible Values} && (4.10)\\ &= 14,400 \text{ Hz} \cdot 2^{12} && (4.11)\\ &= 14,400 \text{ Hz} \cdot 4,096 && (4.12)\\ &= 58,982,400 \text{ Hz} \approx 60 \text{ MHz} && (4.13) \end{aligned}$$

This is significantly faster than the best available radiation hardened analog switches, whose performance becomes marginal at speeds around 2 MHz [Rooney & Frye, 2008].

Figure 4.15 shows a functional diagram of a dual PWM feedback network that solves this problem. Each 10-bit PWM sets its output level by the duty-cycle of the square wave. The low-pass filter reduces the amplitude of the 14,400 Hz repetition rate residual signal. The voltage of the fine PWM is attenuated to set its gain and provide two bits of overlap for the control system. The fine PWM is then summed with the coarse PWM to create a voltage that can be set with a $(10 - 2) + (10 - 2) = 16$ bit resolution. The low-pass reconstruction filters do not completely suppress the 14,400 Hz repetition rate. However, the amplitude is small enough that a classical analog transconductance power amplifier can be used to convert the voltage output into a temperature compensated current source.

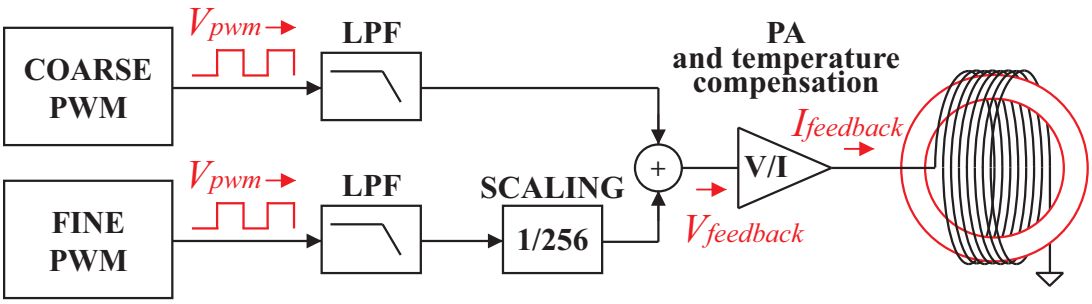

Figure 4.15: Block diagram of the dual pulse width modulation feedback network.

Figure 4.16 shows $V_{feedbacl}$ (top panel) from which is created from the coarse (middle panel) and fine (bottom panel) PWM. The three voltages were captured simultaneously from the operating prototype instrument using a bench-top oscilloscope. Note that, although the reconstruction low-pass filter has removed the majority of the PWM repetition rate and altered the phase, there is still a significant (5 mVpp) sinusoidal residual.

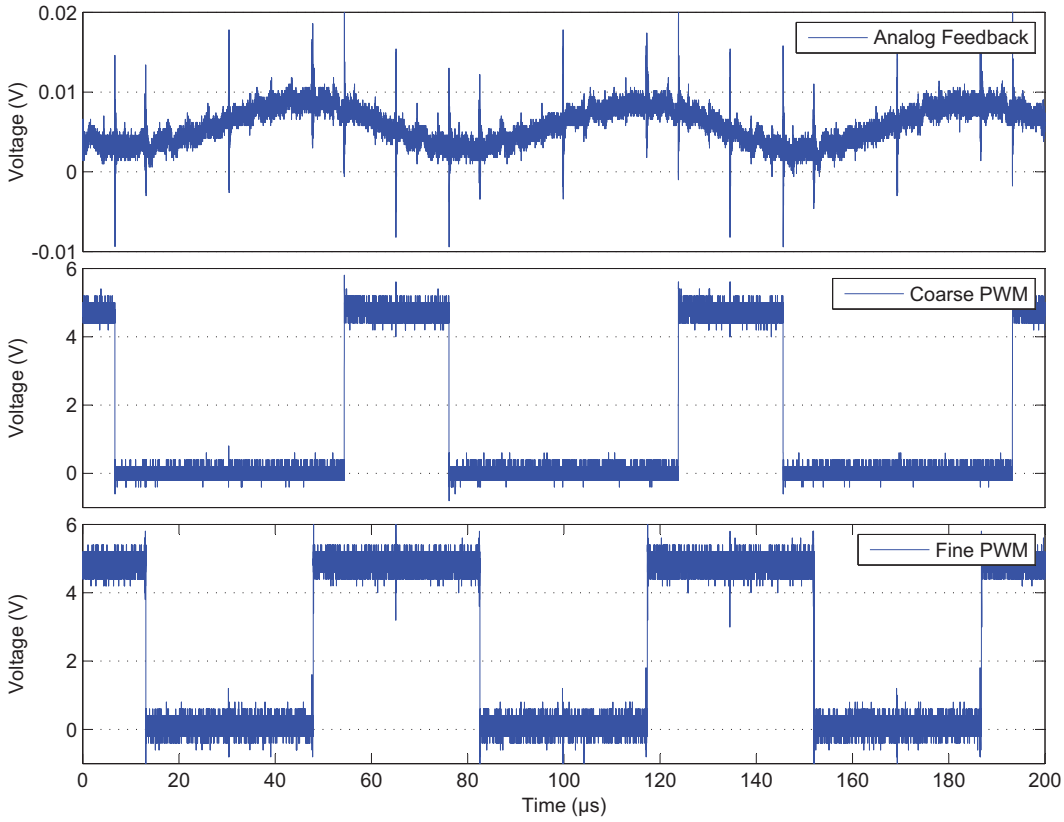

Figure 4.16: Residuals pulse width modulation signal in $V_{feedback}$. $V_{feedbacl}$ (top panel) is created from the coarse (middle panel) and fine (bottom panel) PWMs.

The repetition rate is intentionally set at an integer divisor of the sampling frequency to minimize the average contribution of the sinusoidal residual and prevent the PWM

repetition rate from beating against the sampling rate. However, in this standard fixed frequency PWM configuration, the phase of the repetition-rate residual depends on the duty cycle of the PWM. The PWMs and the ADC sampling are locked together in phase by the fundamental clock of the instrument. However, the phase of the sinusoidal residual of the PWMs depends on the value of the PWM duty cycle as shown schematically in Figure 4.17. The phase of the sinusoidal residual changes by $\sim 180^o$ between a low PWM duty cycle (top panel) and a high PWM duty cycle (bottom panel). The apparent amplitude of the sinusoidal residual, as measured at the ADC sampling point marked by the vertical red line, changes in response to the phase of the residual as well as its amplitude.

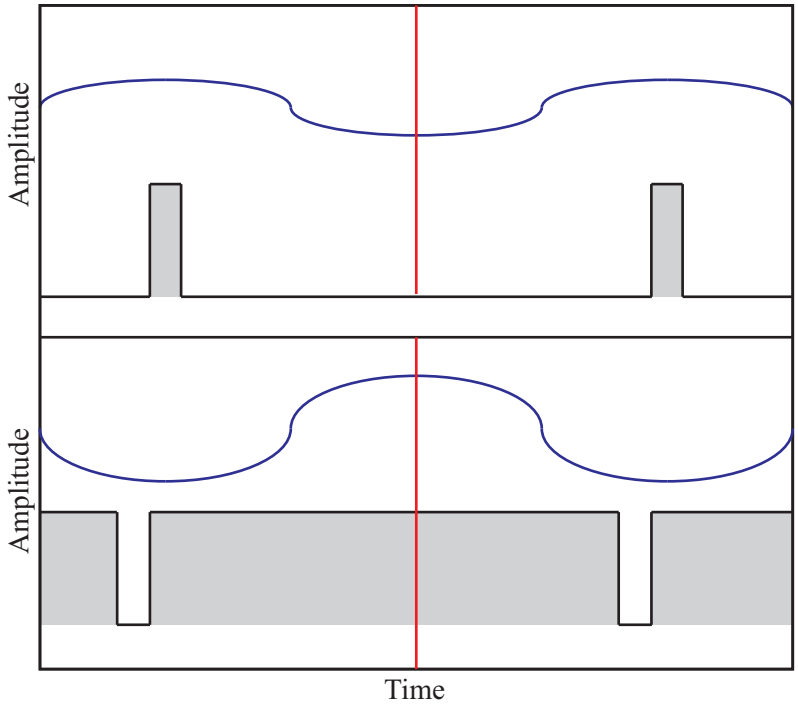

Figure 4.17: Schematic of phase variation in a single edge pulse width modulation. Black shows input pulse width modulation signal. Blue shows sinusoidal residual after filtering. Red shows the phase locked sampling point. The top panel shows a small duty cycle and bottom panel shows a large duty cycle.

This phase change would introduce another error source as the sampled amplitude of even a fixed amplitude residual signal would vary as the changing phase pushed the residual sinusoid across the ADC sampling point. To minimize this effect, the fluxgate prototype implements a fixed frequency and fixed phased double edged PWM as shown in Figure 4.18. Note how the overall phase of the PWM is constant with respect to the sensor's error signal and the ADC sampling points.

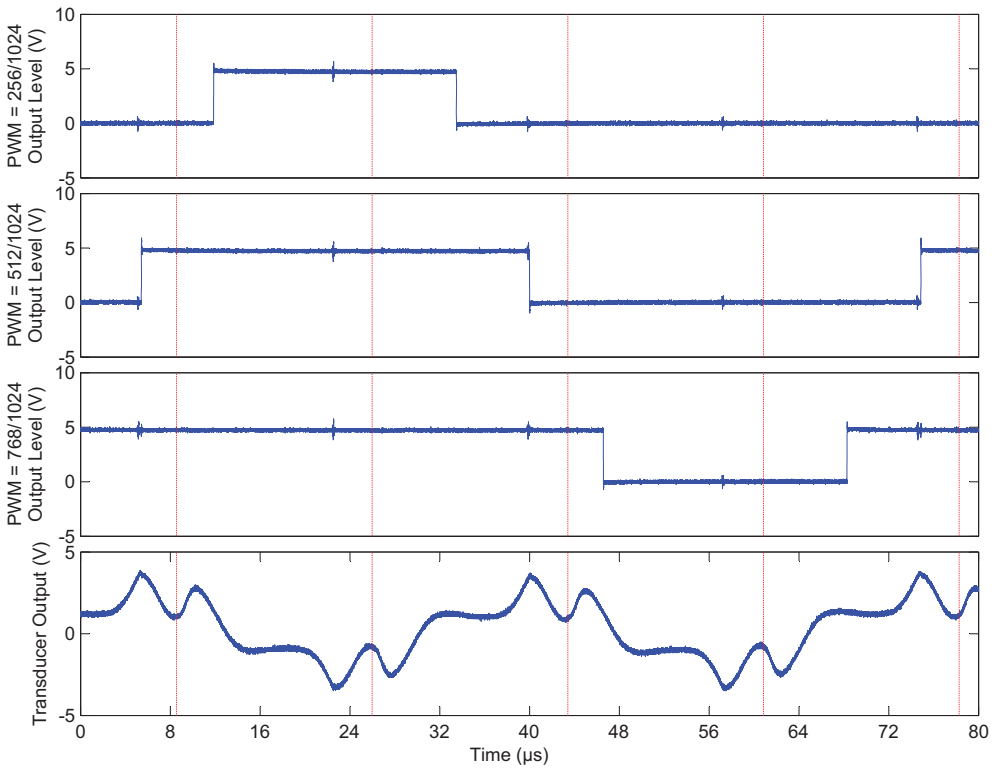

Figure 4.18: Phase synchronised pulse width modulation. The top three panels show PWM signal for duty cycles of 256/1024, 512/1024, and 768/1024. The bottom panel shows the relative phase of the transducer output. The vertical red lines show trigger points of the analog to digital converter.

The disadvantage of a standard double edged PWM is that both the rising and falling edges are moved simultaneously, which halves the number of possible duty cycles for a given clock frequency. The prototype fluxgate implements a modified algorithm where the rising and falling edges are changed independently to create an asymmetric double edge PWM (Figure 4.19). This restores the maximum number of possible states, and therefore maximum possible resolution, at the expense of introducing a very small phase variation in the PWM. The center of the PWM high state shifts by half of one bit as the rising and falling edges are changed causing the phase of the PWM to alternate between two states with a maximum variation of

$$\frac{1}{2} \cdot \frac{1}{1024} = \frac{1}{2048} = 0.05\% \tag{4.14}$$

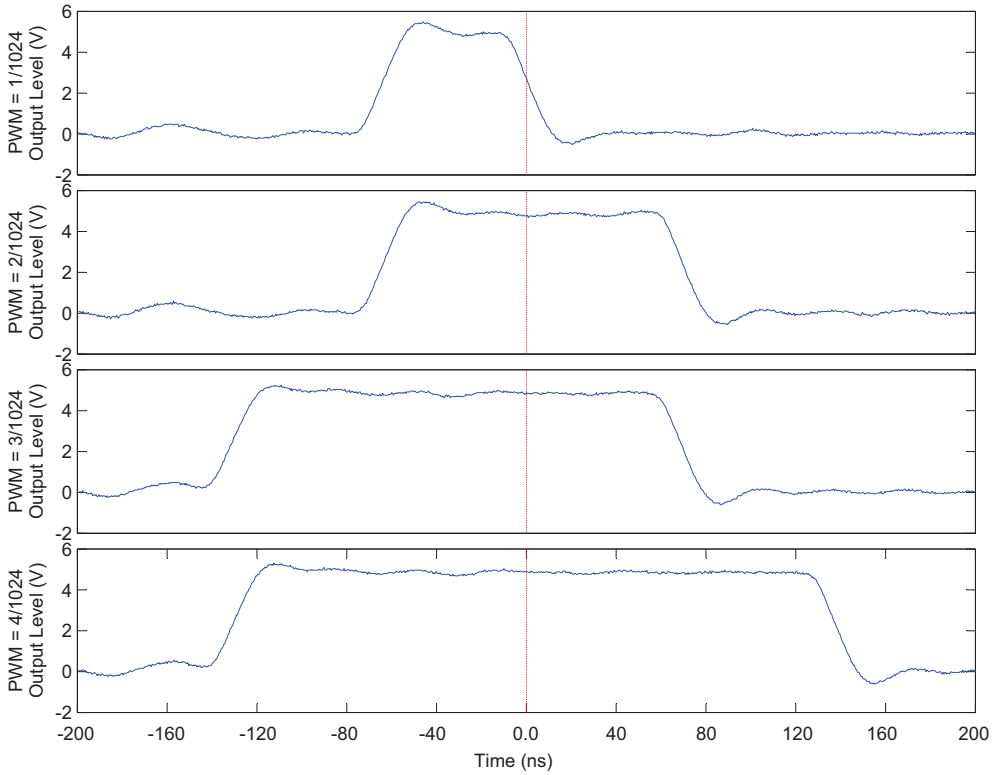

Figure 4.19: Asymmetric double edge pulse width modulation showing duty cycles of 1/1024, 2/1024, 3/1024, and 4/1024 (top to bottom respectively). The vertical red line shows an arbitrary reference phase. Note how the total phase variation is limited to one half of one increment in the PWM.

The main difficulty in implementing a PWM based digital to analog converter is shifting the 0-5 V output of the FPGA to a high-precision bi-polar ±3.5 V signal to allow the instrument to provide both positive and negative feedback. The level switching is implemented using a solid-state analog switch with its inputs connected to the highly stable +3.5 V and -3.5 V references created from the 7 V Zener reference (see Section 4.9.4).

The best available 100 krad tolerant analog switch is the Intersil HS-303ARH. The limiting parameter is the switching time required for the chip to propagate a change in signal level. This is quantified by two parameters. t_{on} is the time for the output to reach 90% of its final value in response to a low-to-high, positive going, transition at the input. t_{off} is the time for the output to reach 10% of its final value following a high-to-low, negative going, transition at the input. t_{on} is much smaller than t_{off} (i.e., the component can switch positive faster than it can switch negative), which distorts the level translated PWM signal as shown in Figures 4.20 and 4.21.

Figure 4.20 shows how the large t_{off} and small t_{on} shorten the negative-going transition in the PWM. In the extreme cases of a large PWM value (PWM duty cycle above 1022/1024), the difference between t_{on} and t_{off} prevents the transition from being propagated through the analog switch.

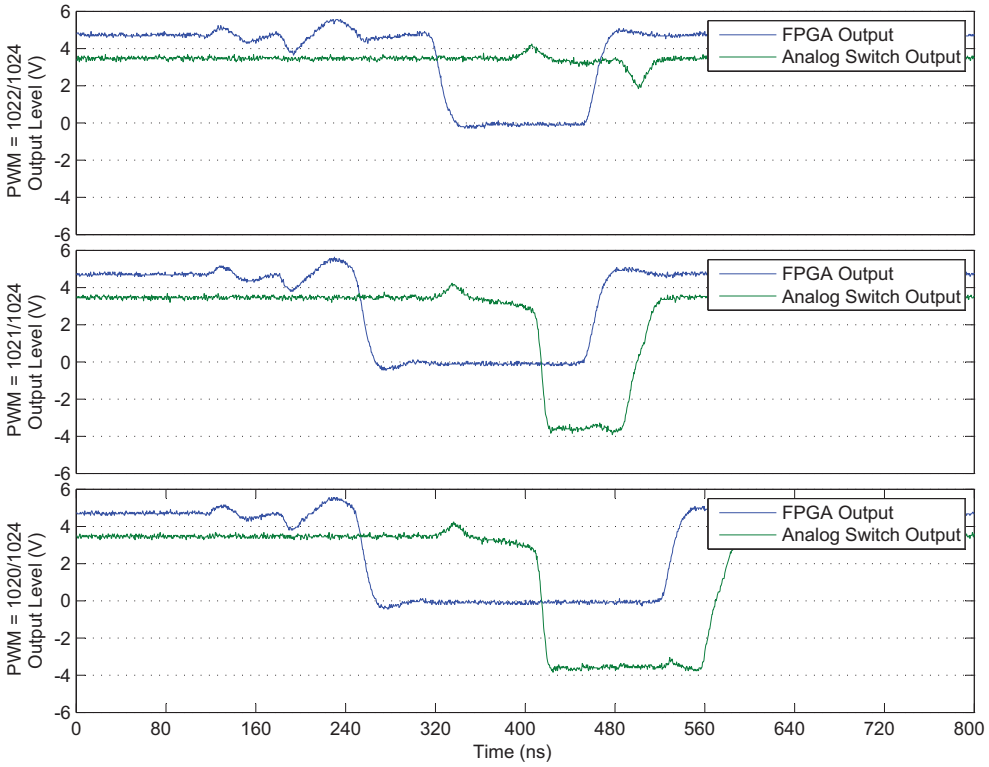

Figure 4.20: Pulse Width Modulation level translation for three negative going pulse. Note how the negative-going pulse is shortened by the analog switch due to t_{on} being much smaller than t_{off}. The short negative going pulse for PWM duty cycles above 1022/1024 fail to propagate through the analog switch

Conversely, Figure 4.21 shows how the positive-going transition is extended by the difference between t_{on} and t_{off}. This is effect is present at all PWM values but is most easily seen with short positive-going transitions associated with very small PWM values (e.g., PWM duty cycles of 1/1024 and 2/1024).

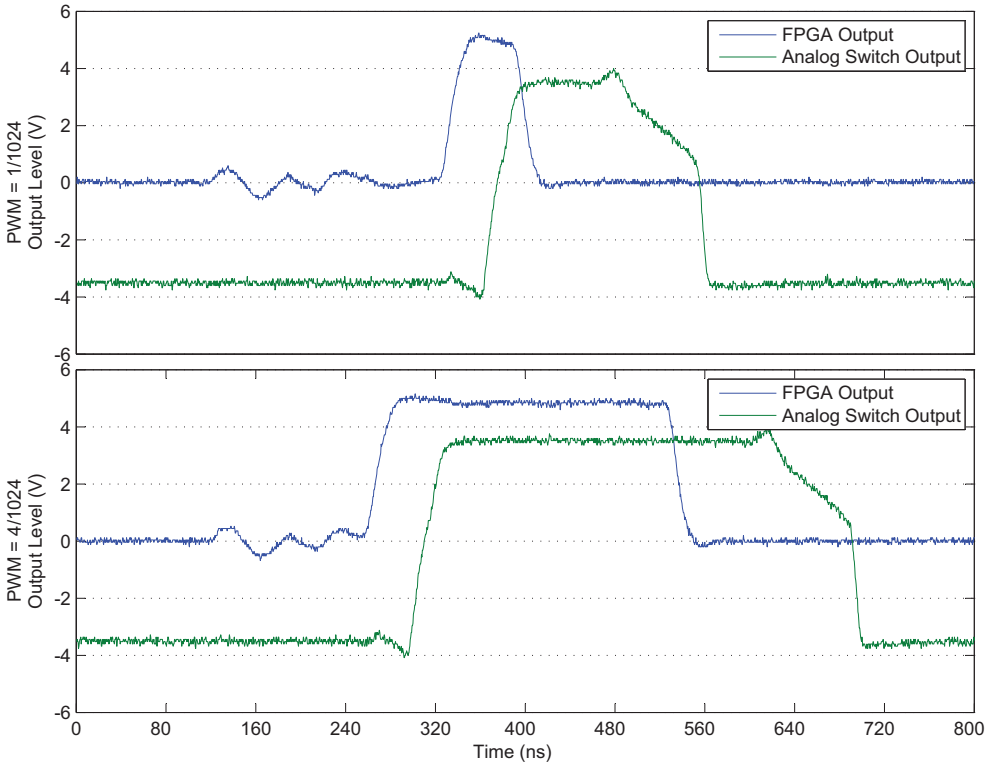

Figure 4.21: Pulse width modulation level translation for a positive going pulse. Note how the positive-going pulse is extended by the analog switch due to t_{on} being much smaller than t_{off}.

Throughout most of the PWM range, the asymmetry between t_{on} and t_{off} results in a constant offset in the average value, which can be removed using an internal calibration coefficient in the instrument. However, when the PWM value is very large and the transient does not propagate through the analog switch, the PWM output becomes non-linear. The PWM is digitally corrected in two ways to minimize this effect: an internal offset of three PWM counts is applied to minimize the static offset, and the non-linear extreme PWM values are not used by the firmware.

Despite the complexity of the asymmetric, dual edge, constant phase, level translated dual summed PWM system, the result is a radiation hard digital to analog converter that can be manufactured from 100 krad tolerant Class-S parts. This system creates an extremely linear (see Section 5.4.3) 16 bit DAC that is noise free to the 24 bit level within the frequency range of the instrument.

4.9.3 Control Loop

The prototype fluxgate has three independent control loops, one for each component of the magnetometer. The control loops are written in System Verilog Hardware Description Language (HDL) and implemented in the FPGA. A standard programming language (e.g., C++, Java, Matlab) defines a sequence of logical operations, which are executed by a processor. HDL defines discrete special purpose digital logic, which is

executed in parallel. This allows the three axes of the magnetometer to be executed simultaneously but independently and be synchronised to the accuracy of the base system clock (∼15 MHz). The firmware reads the sensor using the ADCs, servos the coarse and fine PWMs to provide feedback to keep the sensor near midrange, and accumulates the ADC and DAC values, which form the reported measurements of the magnetic field. The control loop changes the total offset from the coarse and fine PWMs based on the difference between the average ADC measurement and zero. Expressed as a control system, this is equivalent to a proportional controller with a set-point of zero. This simple algorithm is adequate for the requirements of the ORBITALS mission.

Figure 4.22 shows the Verilog code, which accumulates the ADC readings for each component into the ADCAccumulator. The ADCAccumulator is set to zero after each update so there is no integral gain in the control loop. The system was tested with small amounts of integral gain, but even small amounts cause the system to oscillate. However, the control loop settles quickly to the set-point with simple proportional gain so integral gain is not required for the ORBITALS application.

```
always @(posedge clk or posedge reset) begin
    if (reset) begin
        ADCAccumulator = 0;
    end else if (update == 1) begin
        ADCAccumulator = 0;
    end else if ( ADCSync) begin
        ADCAccumulator = ADCAccumulator + {{16{wireADCData[15]}},wireADCData};
        if (ADCAccumulator >  32'sd10000000)
            ADCAccumulator =   32'sd10000000;
        if (ADCAccumulator < -32'sd10000000)
            ADCAccumulator =  -32'sd10000000;
    end
end
```

Figure 4.22: Accumulation algorithm for analog to digital converter measurements.

The coarse and fine PWMs are recalculated at each update as shown in Figure 4.23. If the fine PWM is within the top or bottom 1/8th of its range, the coarse PWM is incremented or decremented by one and, simultaneously, the fine PWM is moved by an equivalent 512 bits in the opposite direction. This restores the fine PWM to near midrange but does not affect the total feedback current sent to to the fluxgate sensor. The fine PWM is servoed in proportion to the value in the ADCAccumulator to drive the error signal back towards the setpoint of zero.

```
always @(posedge clk or posedge reset) begin
if (reset)
    begin
    CoarsePWM_next = 32'sb0;
    FinePWM_next = 32'sb0;
    FinePWM_adjust = 32'sb0;
    end
else
    begin
    if (update == 1)
        begin
        if ((FinePWM >= 32'sd384)  && (CoarsePWM <= 32'sd512 - 32'sd1) )
            begin
            CoarsePWM_next = CoarsePWM + 32'sd1;
            FinePWM_adjust = -32'sd512;
            end
        else if ((FinePWM <= -32'sd384)  && (CoarsePWM >= -32'sd512 + 32'sd1))
            begin
            CoarsePWM_next = CoarsePWM - 32'sd1;
            FinePWM_adjust = 32'sd512;
            end
        else
            begin
            CoarsePWM_next = CoarsePWM;
            FinePWM_adjust = 0;
            end
        end
    else
        begin
        CoarsePWM_next = CoarsePWM;
        FinePWM_adjust = 0;
        end

    if (update == 1)
        begin
        FinePWM_next =    (ADCAccumulator/((FINEPWMSCALE*ADCRATE)/(ADCSCALE*↩
            UPDATERATE))) + FinePWM + FinePWM_adjust;
        if (FinePWM_next > 32'sd510) FinePWM_next = 32'sd510;
        if (FinePWM_next < -32'sd510) FinePWM_next = -32'sd510;
        end
    else
        begin
        FinePWM_next = FinePWM;
        end
    end
end
```

Figure 4.23: Control logic for the coarse and fine pulse width modulations

The science data measurements are built up from the coarse and fine PWM values and the value in the ADCAccumulator as shown in Figure 4.24. The coefficients COARSEPWMSCALE, FINEPWMSCALE, ADCSCALE, and OFFSET are experimentally determined calibration coefficients (see Section 5.5) and are unique for each component and each instrument. The sampling rate for the instrument (UPDATERATE) is included in all the calculations using a macro so that the sampling rate of the instrument can be changed by redefining one variable. Note that while the coarse and fine PWM values are temperature compensated, the ADCAccumulator value is not.

```
always @(posedge clk or posedge reset) begin
    if (reset) begin
        outputData <= 32'sd000000;
        regdataReady <= 0;
    end else if (update == 1) begin
        outputData <= nextData;
        nextData <= COARSEPWMSCALE*CoarsePWM + FINEPWMSCALE*FinePWM + (↩
            ADCAccumulator*ADCSCALE)/(ADCRATE/UPDATERATE) - OFFSET;
        regdataReady <= 1;
    end else begin
        outputData <= 0;
        regdataReady <= 0;
    end
end
```

Figure 4.24: Algorithm to calculate science data from internal values.

This control loop meets the requirements for the ORBITALS mission. However, for applications were the spin rate is much faster (e.g., the 6 Hz spin rate of the ICI-4 sounding rocket mission) some differential gain may be required to efficiently track the spin signal. In future work, it may be useful to re-write the control loop using a traditional Proportional Integral Derivative (PID) controller (cf. Bennett [1993]) so that the next feedback value can be determined not just by the difference between the current value and the ideal value (proportional gain in a PID) but also the rate of change (differential gain in a PID) and the average recent value (integral gain in a PID). Having access to all three control variables would make it easy to tune the instrument control loop to new applications. In particular, differential gain may be required to track the fast spin rates of sounding rocket applications. However, the current algorithm meets the requirements of the ORBITALS application and was successfully validated in a variety of tests as described in Chapter 5.

4.9.4 Thermally Stabilized Reference

The most stable 100 krad tolerant Class-S Zener reference diode available is the Linear Technology Inc. RH1021BM-7. This Zener diode has a specified temperature coefficient of 5 ppm/^{o}C. Unfortunately, over the -40 to +50 ^{o}C operating temperature range of the electronics package this translates into a potential worst case error of

$$\pm 65,536 \text{ nT} \cdot (50 + 40) \ ^o\text{C} \cdot \frac{5}{1,000,000 \ ^o\text{C}} = \pm 30 \text{ nT} \tag{4.15}$$

which would be the largest accuracy error source in the instrument by at least an order of magnitude. This error source can be removed in two ways. The temperature of the Zener diode can be measured during operation and compensated using a pre-determined temperature calibration in post-processing. Alternatively, the Zener diode could be placed in a temperature controlled environment to minimize the effect of the temperature coefficient. In terrestrial applications, temperature controlled Zener references are available as integrated circuits. However, no such parts are available with 100 krad radiation tolerance.

After discussing this potential issue with the ORBITALS Principle Investigator, the decision was made to implement a custom temperature controlled reference using the RH1021BM-7 Zener diode. This subsystem necessarily implements a temperature sensor for the Zener diode, which will permit future users of the instrument to use either method of temperature compensation. The temperature of the Zener diode can be recorded and post-corrected or, alternatively, the temperature control logic can be enabled in the firmware and the diode will be held to within a small temperature range.

Active cooling, such as a Peltier heat-pump, is technically possible on orbit but is both thermally and mechanically complicated. The simplest and most reliable way to thermally stabilise a component is to continuously heat the device to the maximum operating temperature of the electronics package. The disadvantage of this technique is that, unless the devices is very well thermally isolated, it can require a significant amount of heat to hold the component at, for example, +50 ^{o}C with an ambient temperature of -40 ^{o}C. This is complicated by the need for the thermal stabilisation to work in atmosphere (for development and testing), where there is significant convective cooling, and in a vacuum, where the heat-loss is chiefly through conduction.

A test-bed was constructed to estimate the amount of power required to thermally stabilise a Zener diode in air and in vacuum. Figure 4.25 shows the relevant section of the test-bed schematic.

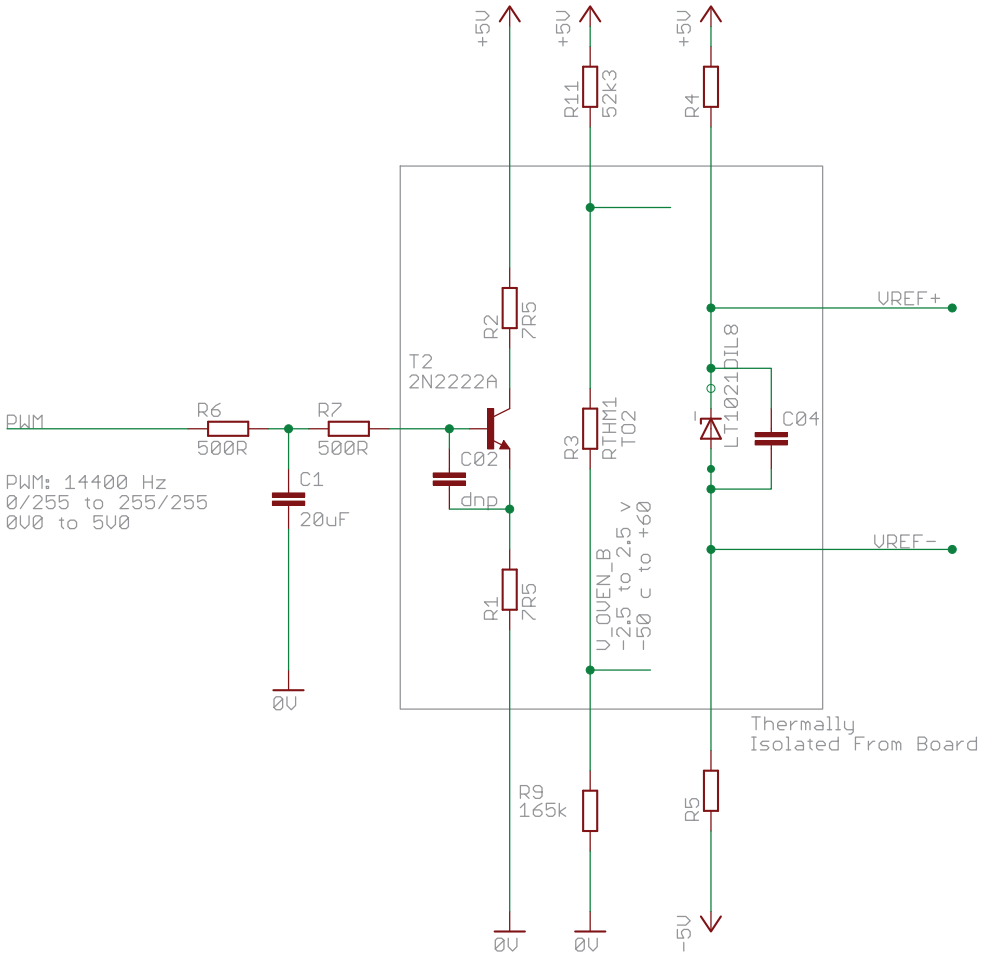

Figure 4.25: Schematic for thermally controlled Zener reference diode.

A digital PWM and low-pass filter are used to throttle a bipolar transistor (T2) and pass current through two power resistors (R1 and R2). Both the transistor and the power resistors act as heat-sources for the temperature controller. A thermistor (R3) monitors the temperature of the Zener diode (LT1021DIL8). The thermistor output is conditioned and digitised by circuitry not shown on this schematic. The grey box indicates the thermal isolation boundary created by milling away printed circuit board material in a square (Figure 4.26).

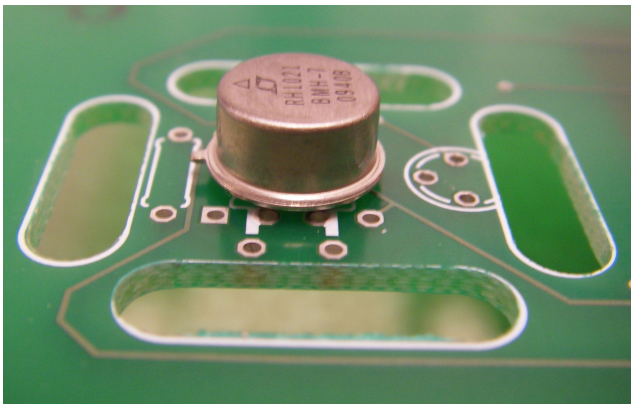

Figure 4.26: Thermal isolation for the Zener reference diode.

A test-bed and a custom aluminium plate were manufactured (Figure 4.27) to mimic the best possible conductive heat path (e.g., worst case thermal design) available in orbit. The printed circuit board has thermal contact with the 8 mm aluminium wall and through 4 stand-offs. The bottom of the aluminium plate is curved to match the internal surface of a vacuum chamber.

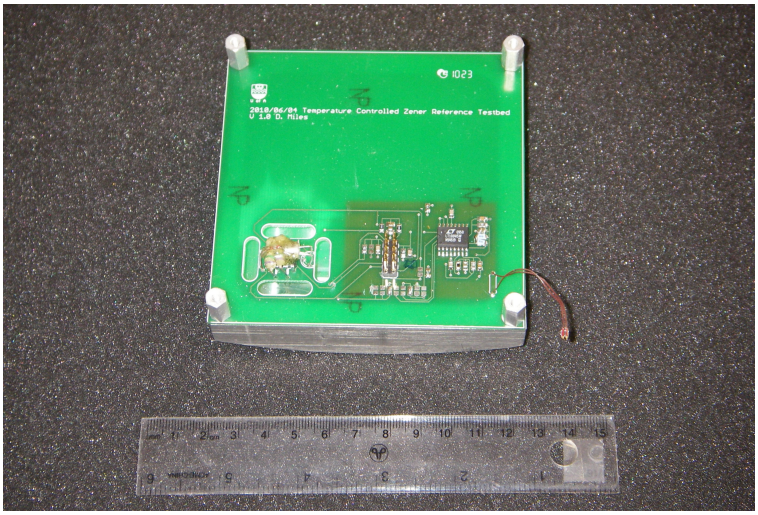

Figure 4.27: Test-bed for thermally controlled Zener reference diode.

The vacuum chamber was placed in a freezer, pumped down into vacuum and chilled to -40 ^{o}C using dry ice. The test-bed required about 250 mW to maintain the Zener diode at +50 ^{o}C in vacuum. The test was repeated in air with a small Styrofoam cap over the diode and the test-bed required 1.25 W to maintain the same temperature. This test led to two requirements for the prototype. The power-supply must be designed to provide up to 1.25 W (before margin) for the Zener reference. However, the on-orbit power budget should only allocate a nominal 250 mW for the Zener heater. Based on this successful test, the schematic and layout for the temperature controlled Zener reference were copied to the design for the analog electronics card.

4.10 Instrument Design Summary

The design of the fluxgate magnetometer presented in this thesis is heavily influenced by the limited selection of 100 krad tolerant space qualified electronic components, which can survive and operate in the harsh radiation environment of the Van Allen radiation belts. The instrument implements an offsetting algorithm, where the main field is subtracted off using a high precision reference, to achieve 8 pT resolution irrespective of the magnitude of the geomagnetic field. A novel feedback design, using two filtered and summed PWM signals, combines the simplicity and radiation tolerance of digital feedback with analog temperature compensation of the sensor. The drive frequency of the instrument has been increased to 28.8 kHz to move the FGM's magnetic signature above the measurement band of its intended co-manifest SCM. These changes significantly improve the AC performance of the instrument, allowing it to tolerate the 60 Hz noise found in most laboratory environments, and to track the apparent large amplitude field caused by a rotating spacecraft frame.

Chapter 5

Instrument Characterization

5.1 Test Facilities and Experimental Set-up

The performance of the prototype FGM was characterized at two facilities. The NRCan Geomagnetic Laboratory in Ottawa maintains Canada's official geomagnetic reference, and one of their the facilities was used to characterise the absolute accuracy and noise of the prototype instrument. Facilities in the CARISMA laboratory at the UAlberta was developed to support the CARISMA array of ground magnetometers was also used for general development and to assess the prototype's AC performance. These two test facilities are described in Sections 5.1.1 and 5.1.2 respectively.

5.1.1 National Resources Canada Geomagnetics Laboratory

Magnetic noise and RMS error analysis (Tests 2 and 3 in Section 5.4) were conducted at the NRCan Geomagnetics Laboratory on Anderson Rd, Ottawa, ON using the "Building 8" facility. This is a magnetically quiet location with a large Helmholtz coil capable of dynamically nulling the Earth's magnetic field to O (10 nT) based on a nearby reference magnetometer. Configurable test signals can be added to the Helmholtz coil. A high-precision current measurement, combined with the coil coefficients of the Helmholtz coils, is then used to calculate the exact magnetic field experienced by the magnetometer under test. Figure 5.1 shows a simplified block diagram of one axis of the test configuration. In testing, all three components of the local field were nulled, but the test signals were applied in one axis at a time. A photograph of the test setup is presented as Figure 5.2. Magnetometer test data were transmitted over a serial connection and visualised and logged using a laptop computer with a custom Labview interface (Section 5.3).

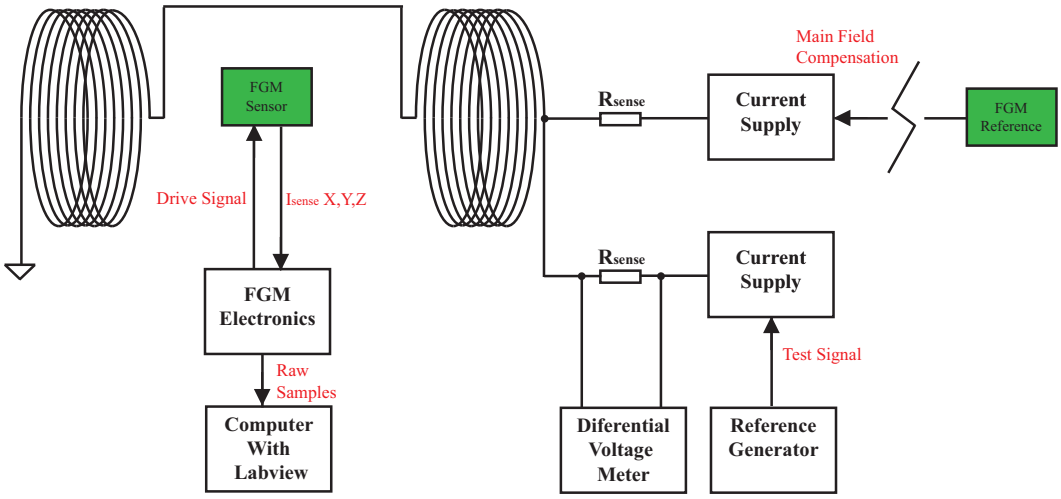

Figure 5.1: Simplified single axis test schematic of NRCan Geomagnetics Laboratory Building 8 Facility.

Figure 5.2: Test setup photo. NRCan, Geomagnetics Laboratory, Building 8.

5.1.2 CARISMA Laboratory — University of Alberta

Instrument resolution and slew rate analyses (see Tests 1 and 4 in Section 5.4) were completed at the UAlberta CARISMA laboratory in Edmonton, AB. The fluxgate sensor was placed in a test solenoid within a three layer mu-metal magnetic shield. The magnetic shield suppresses the ambient magnetic noise and creates a near-zero magnetic field (O (10 nT) in each direction). Test signals were generated by driving the solenoid with a Stanford Research DS360 ultra low distortion function generator. Magnetometer test data were transmitted over a serial connection and visualised and logged using a laptop computer with a custom Labview interface (Section 5.3). This

is shown schematically in Figure 5.3 and a photograph of the equipment employed is presented as Figure 5.4. This facility has significantly more magnetic noise than the NRCan facility and the test solenoid and signal generator are not calibrated against an established geomagnetic reference. However, the test fixture in the CARISMA laboratory was developed for testing induction coil magnetometers and is ideal for testing the dynamic performance of the FGM.

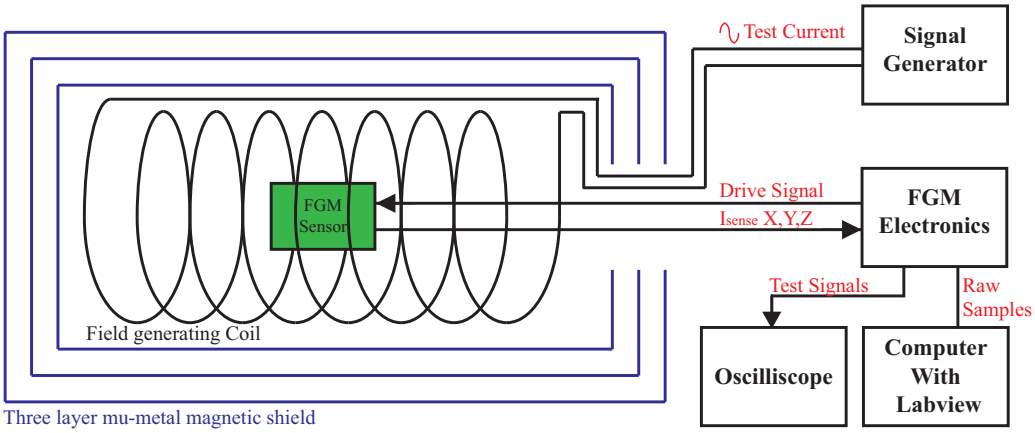

Figure 5.3: Test setup schematic of UAlberta CARISMA laboratory. Adapted from Milling et al. [2011].

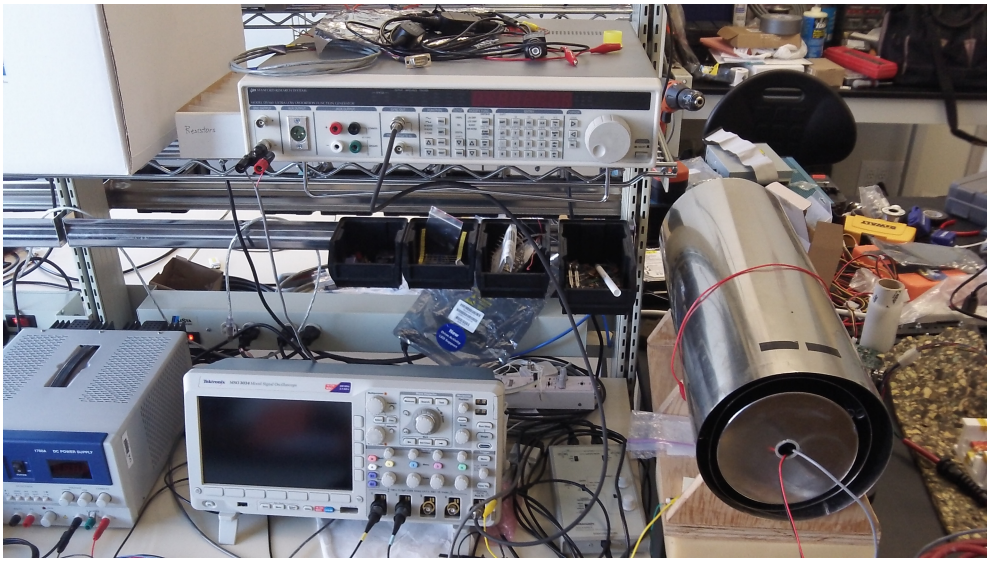

Figure 5.4: Test setup photo at UAlberta CARISMA laboratory.

5.2 Spectral Analysis Techniques

Two types of spectral plots were used in the characterisation of this instrument. Amplitude spectra are used to measure the amplitude of known test signals and Power Spectral Density (PSD) is used to measure the incoherent noise floor. The amplitude

spectra plots are normalised such that the amplitude of the coherent test signals is in calibrated physical units (nT) and is independent of the number of spectral bins. However, the amplitude of the noise floor in the amplitude spectra depends on the number of spectral bins and should not be used. The PSD plots are normalised such that the amplitude of the noise floor is in calibrated physical units (nT^2/Hz) and is independent of the number of spectral bins. However, in the PSD plots the apparent amplitude of a coherent signals depends on the number of spectral bins and should not be used. Both spectral products are are calculated using an overlapped segmented averaged modified periodogram (Welch's algorithm) following the methods described by Heinzel [2002]. Further details of the spectral analysis techniques used can be found in Appendix A.

5.3 Operation of Instrument

The science operation and data-flow of the FGM is shown schematically in Figure 5.5.

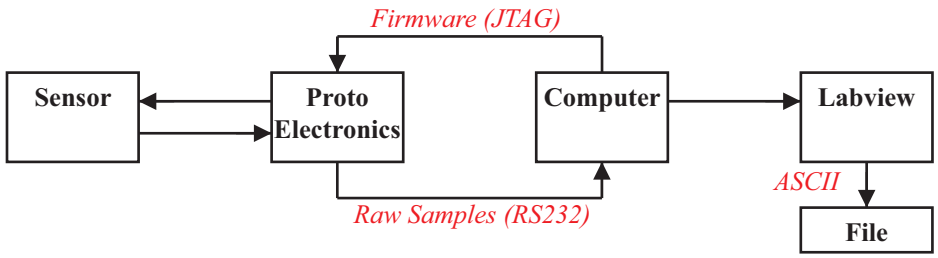

Figure 5.5: Operation and data flow in prototype instrument.

The instrument's operation is controlled by firmware written in the System Verilog HDL, which implements the control loop described in Section 4.9.3. This source code was synthesized into firmware on a host computer and then loaded into the prototype electronics using a Quartus in-circuit programmer. The electronics drive the sensor and servo it into range using the feedback network. The firmware uses the programmed scaling coefficients to manufacture 900 scaled magnetic field measurements per second for each of the three magnetometer components. These data are transmitted as frames of raw binary values over a standard RS-232 serial connection back to the host computer. A custom Labview user interface, shown in Figure 5.6, was written to capture and display this information.

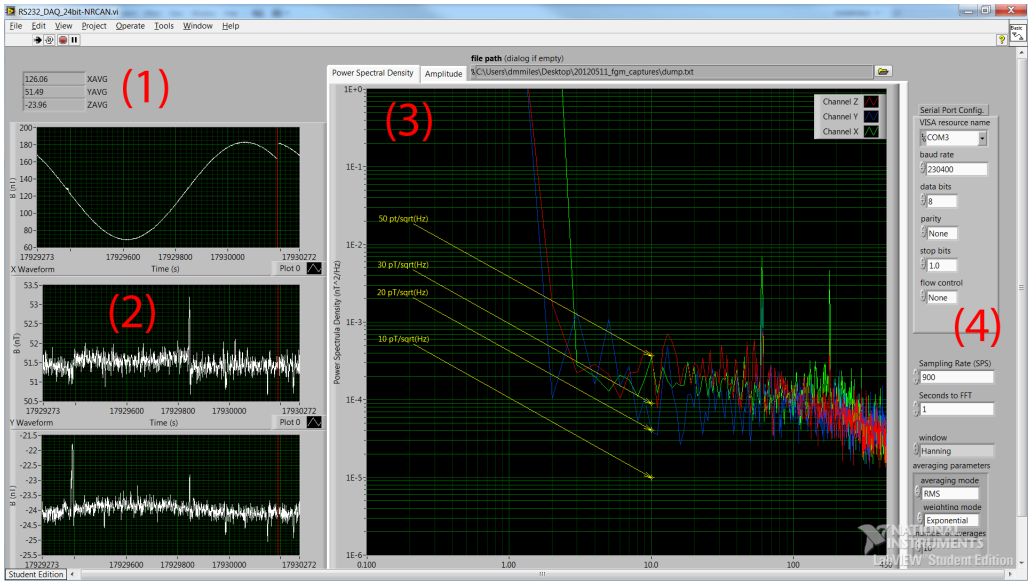

Figure 5.6: Custom Labview based real–time data capture and visualisation tool

The Labview tool captures the serial data stream of magnetic field measurements, synchronises to framing information within the data and saves the magnetometer output into a standard ascii data file. Several Matlab scripts were created to undertake detailed analysis of the instrument performance. However, the labview script was useful as it allowed realtime visualisation of the instrument data during instrument development and testing.

Figure 5.6 shows the standard tools provided by the Labview user interface. Figure 5.6 (1) shows a configurable length simple average for each magnetometer component. The length of the average needs to be set to a multiple of 60 Hz to allow an accurate measurement of the static field. Figure 5.6 (2) shows a simple time series display for each magnetometer component. The vertical axis can be auto-ranged to provide a simple visualisation of the field or alternatively locked to a particular range for noise or small-field measurements. Figure 5.6 (3) shows the spectral display for all three components. The two tabs shift between a PSD plot for noise measurements and an amplitude plot for signal measurement. The FFT size, window function and averaging modes are configured using the control panel shown in Figure 5.6 (4)

5.4 Instrument Performance Under Test

5.4.1 Test 1 — Instrument Resolution

Test 1, instrument resolution, is used to validate three core requirements defined by Milling et al. [2009]:

1. Measurement Resolution: the FGM payload shall measure each magnetic field sample to a resolution of at least 0.1 nT;

2. Cadence: the FGM payload shall measure the 3-D vector magnetic field with a cadence of at least 32 samples per second; and

3. AC Range: the FGM payload shall measure the AC 3-D vector magnetic field up to a frequency of at least 10 Hz.

The prototype instrument is designed such that the analog-to-digital converter has a least significant bit of 57 pT. This is the smallest resolution that can safely accommodate the analog error signal under normal operating conditions. However, the error signal is digitized at 57,600 sps and down-sampled by 64 into a 900 sps data product. Oversampling by four times creates one effective bit of resolution. Therefore, oversampling by $N = 64 = 4^3$ creates three additional bits of resolution for an effective resolution of

$$\left\lceil \frac{\text{Physical Resolution}}{2^{\frac{\log N}{\log 4}}} \right\rceil = \left\lceil \frac{57 \text{ pT}}{2^3} \right\rceil = \left\lceil 7.1 \text{ pT} \right\rceil \tag{5.1}$$

or, to the next largest integer, 8 pT resolution.

The instrument was driven with a series of test signals to validate that the resolution requirement was met. Figure 5.7 shows environmental noise with no test signal applied. A 50 pT peak-to-peak sine wave was applied at 10 Hz, 1 Hz, 0.1 Hz, 0.01 Hz, and 0.001 Hz (Figures 5.8, 5.9, 5.10, 5.11, and 5.12, respectively). As shown below, the test signal is clearly visible at 10, 1, 0.1 and 0.01 Hz and meets the 1/f noise floor at 0.001 Hz. The slight amplitude increase at 0.01 Hz is due to the non-negligible power contributed by the 1/f noise floor. The different shape and scatter of the noise floor in the spectral plots reflect slightly different test durations. These were completed in periods when the CARISMA laboratory could be unused to minimise noise from laboratory equipment or the movement of ferrous materials, such as laboratory chairs. Despite the different test durations, the amplitude of the test signal, and its visibility above the noise floor, is correct in each case. The 50 pT peak-to-peak sinusoidal test signal appears as a

$$\frac{50 \text{ pT-pp}}{2\sqrt{2}} = 18 \text{ pT-RMS} \tag{5.2}$$

amplitude feature on the spectra plots below. The test signal has been marked with an arrow. These test data were captured at the UAlberta CARISMA laboratory. The prototype resolves the 18 pT-RMS signal up to 10 Hz thus meeting the 0.1 nT at 10 Hz mission requirement.

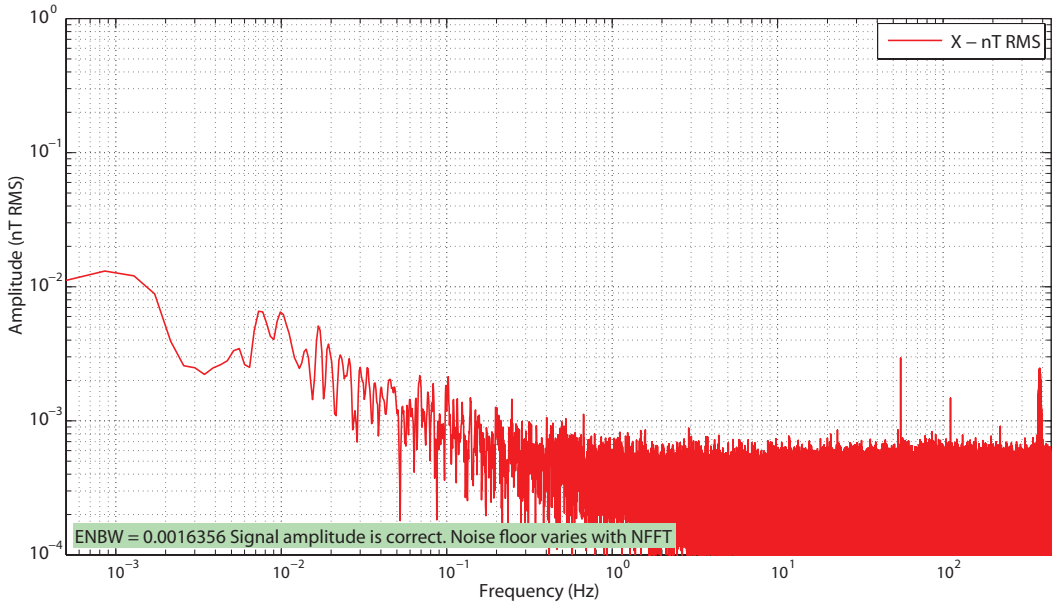

Figure 5.7: Amplitude spectrum - No test signal.

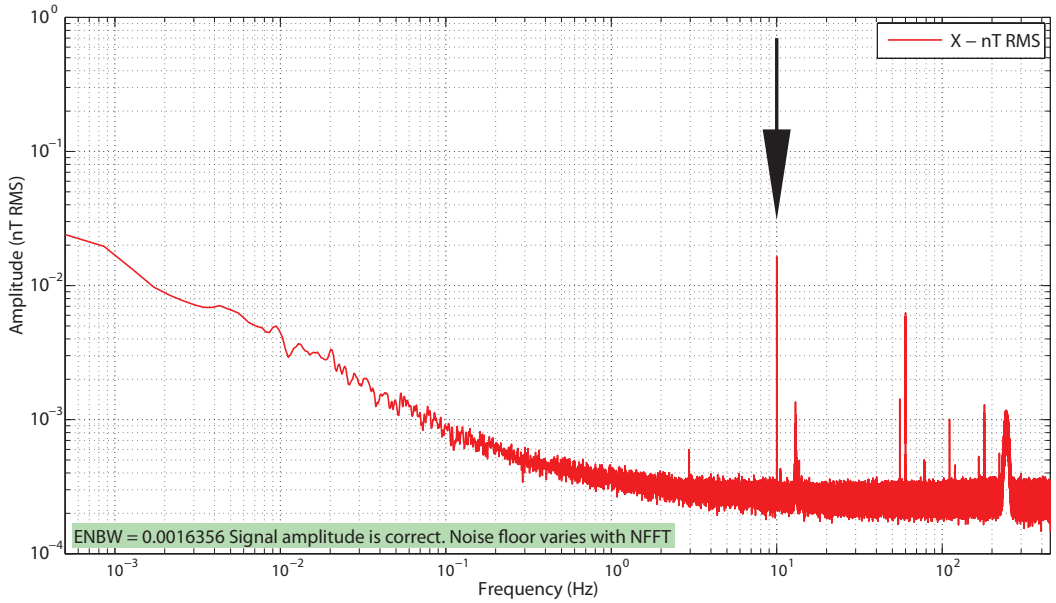

Figure 5.8: Amplitude spectrum - 18 pT-RMS at 10 Hz signal. Arrow shows test signal.

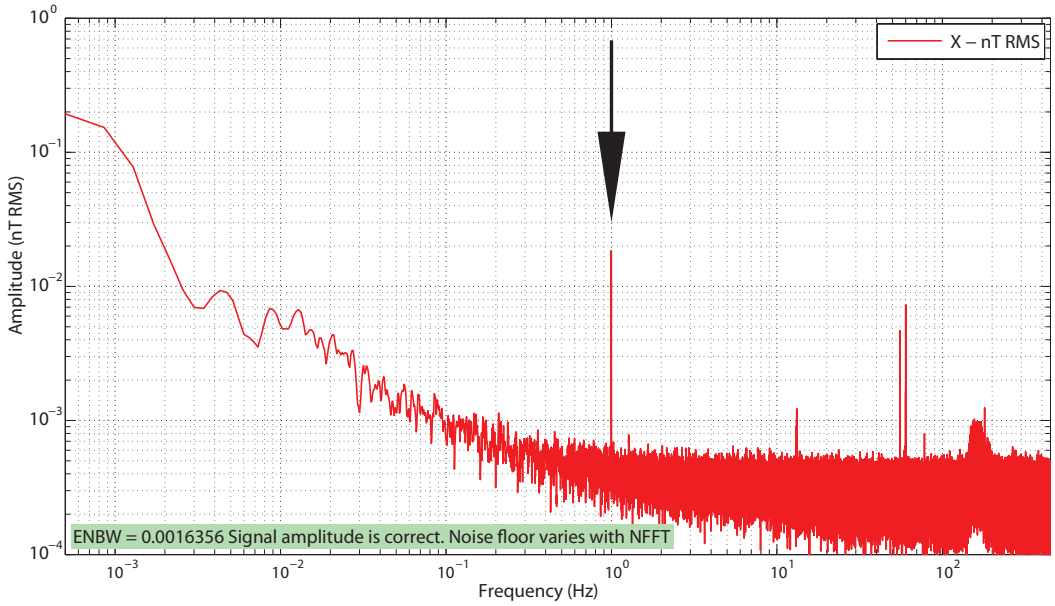

Figure 5.9: Amplitude spectrum - 18 pT-RMS at 1 Hz signal. Arrow shows test signal.

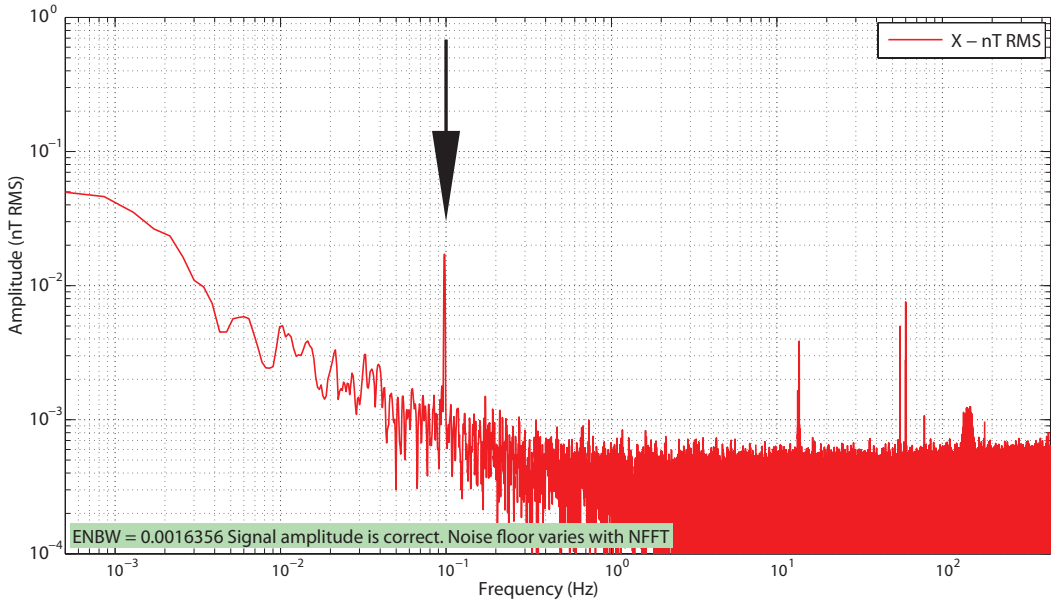

Figure 5.10: Amplitude spectrum - 18 pT-RMS at 0.1 Hz signal. Arrow shows test signal.

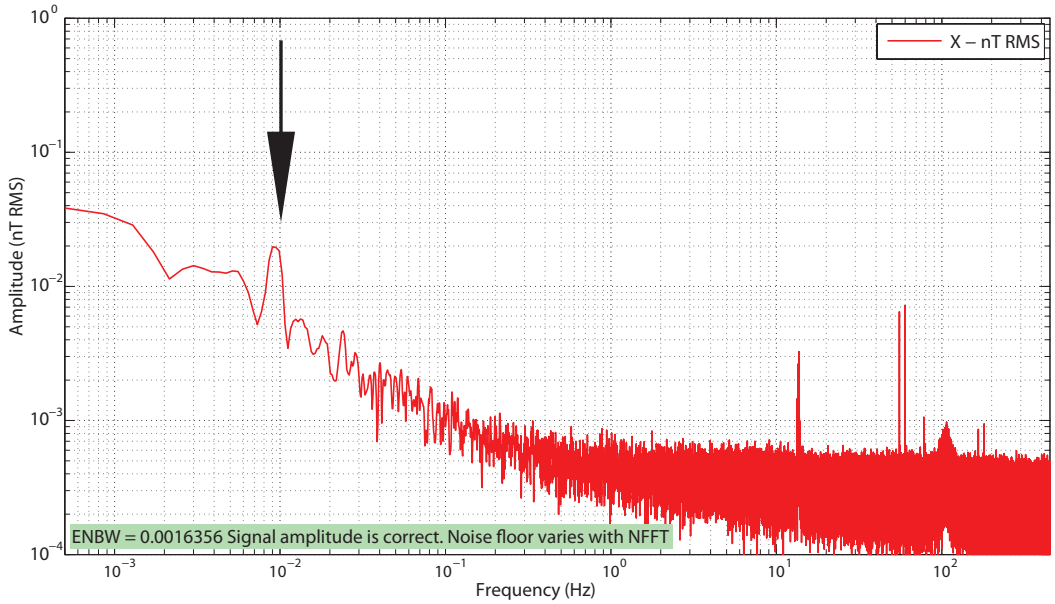

Figure 5.11: Amplitude spectrum - 18 pT-RMS at 0.01 Hz signal. Arrow shows test signal.

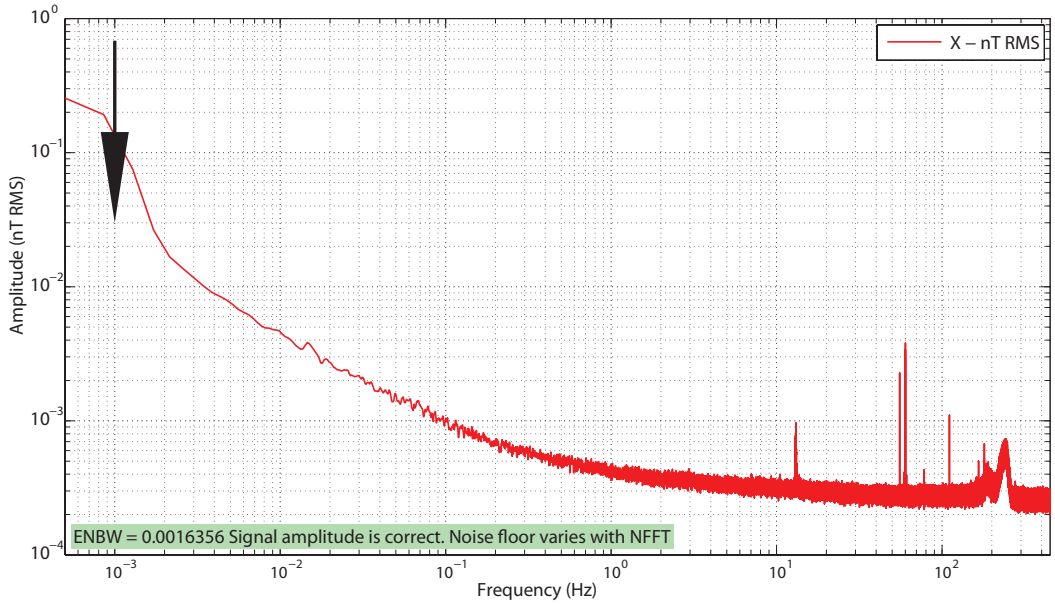

Figure 5.12: Amplitude spectrum - 18 pT-RMS at 0.001 Hz signal. Arrow shows test signal. Note test signal is mixed with the 1/f noise floor and cannot be clearly resolved.

5.4.2 Test 2 — Magnetic Noise

Test 2, magnetic noise, is used to verify the requirement that the FGM payload shall have a maximum equivalent magnetic field noise of 20 $\mathrm{pT}/\sqrt{\mathrm{Hz}}$ rms at 1 Hz.

An hour of magnetically quiet data was captured and the average PSD was calculated in order to validate the magnetic noise requirement. The test data was obtained at the NRCan Geomagnetics Laboratory Building 8 Helmholtz coil to achieve a sufficiently low environmental noise such that the instrument noise could be measured. The fluxgate sensor was placed in a five layer mu-metal magnetic shield within the Helmholtz coil nulled field at the Building 8 test facility.

Figure 5.13 shows the PSD noise floor above 0.1 Hz. Note how the 1/f noise floor dominates below 1Hz. However, for the full specified range, the noise floor meets the 20 pT/$\sqrt{\text{Hz}}$ requirement.

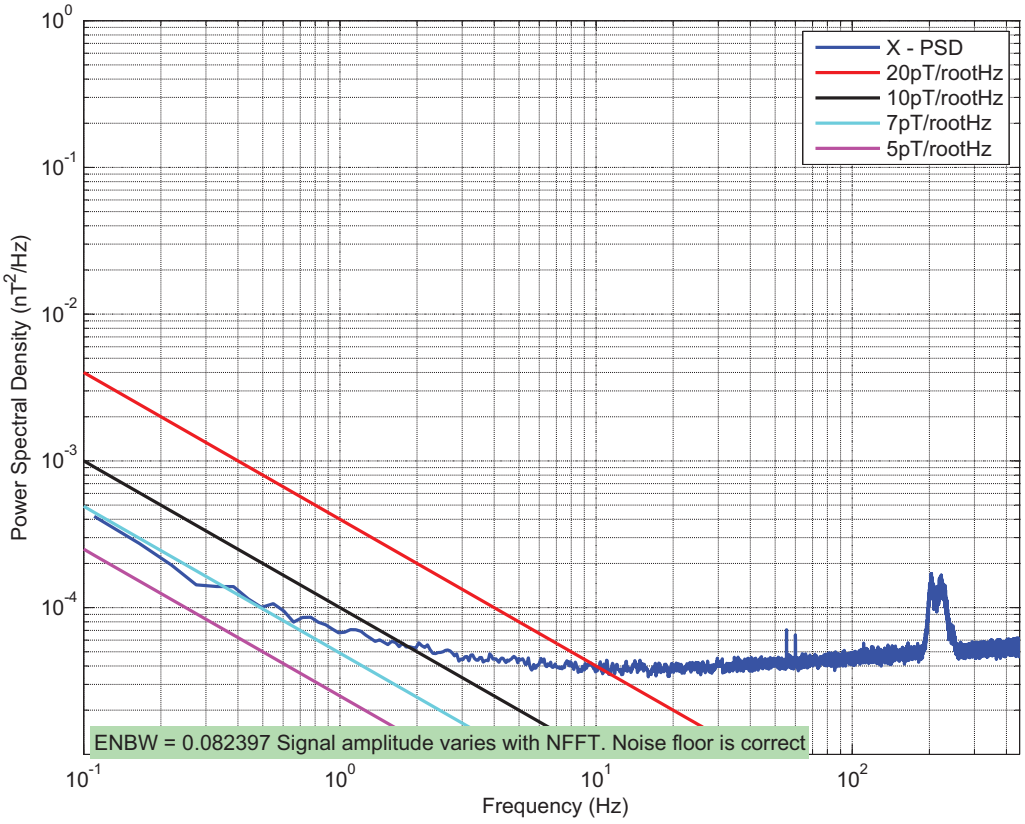

Figure 5.13: Power spectral density noise floor of the fluxgate magnetometer.

Figure 5.14 shows the PSD noise floor down to 0.001 Hz. At these lower frequencies, the previously observed sub 10 pT/$\sqrt{\text{Hz}}$ floor is polluted by statistical noise from the limited data length (1 hour) and large number of bins (1,048,576) in the Discrete Fourier Transform (DFT). However, the measured noise floor is essentially 10 pT/$\sqrt{\text{Hz}}$ over the full frequency range and meets the 20 pT/$\sqrt{\text{Hz}}$ requirement.

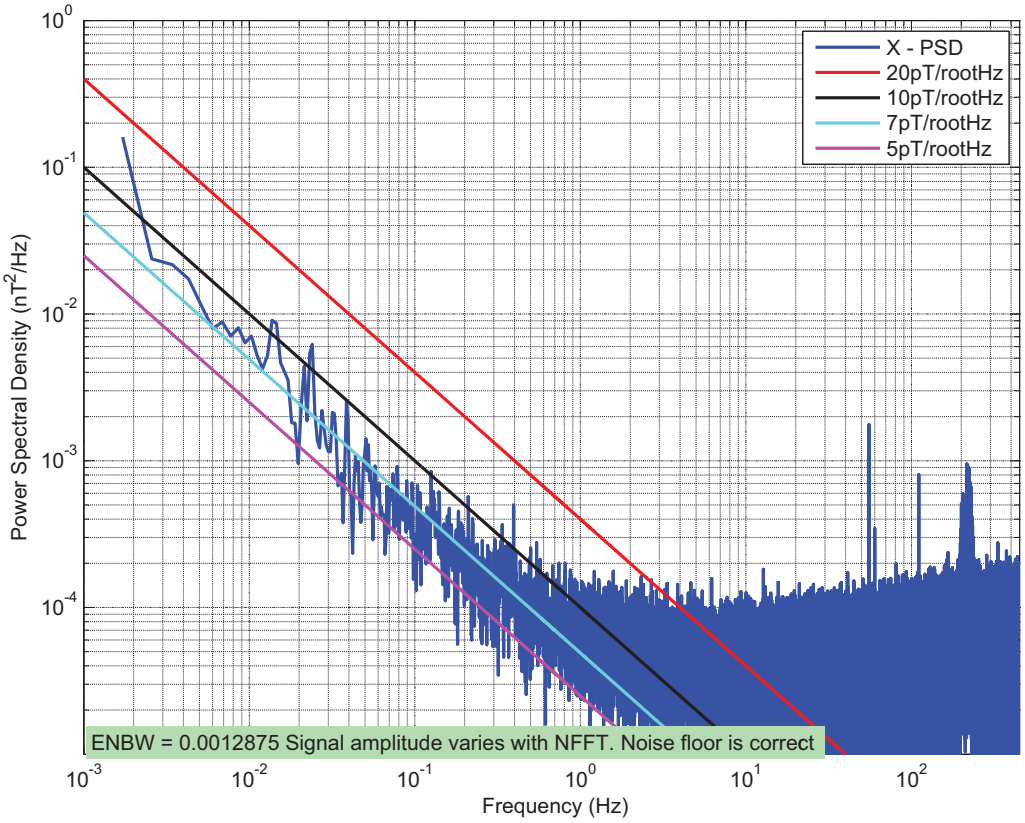

Figure 5.14: Low frequency power spectral density noise floor.

5.4.3 Test 3 — Measurement Accuracy

Test 3, RMS deviation, is used to validate the requirement that the FGM payload shall measure the magnetic field on three axes with an accuracy of at least 0.1%.

To quantify the RMS error, the FGM sensor was placed within a known field generated by the Helmholtz coil test equipment at NRCan. Each component was varied over the full scale range and compared to a measurement of the current used to drive the Helmholtz coil.

The RMS error provides an estimate of the expected absolute error of the instrument at any point in its ±65,536 nT range. It is calculated by using the known absolute current measurements to create a set of ideal instrument measurements. The difference between each measured point and the ideal measurement are then averaged by a RMS calculation following the equation

$$\text{RMS Deviation} = \sqrt{\frac{\sum_{i=1}^{n} (\text{Ideal}_n - \text{Actual}_n)^2}{n}} \tag{5.3}$$

Each datum is taken as the arithmetic mean of 900 samples (1 second) to cancel out the 60 Hz contamination. Figure 5.15 plots the RMS deviation data for a single component

and demonstrates the high linearity and accuracy of the developed instrument.

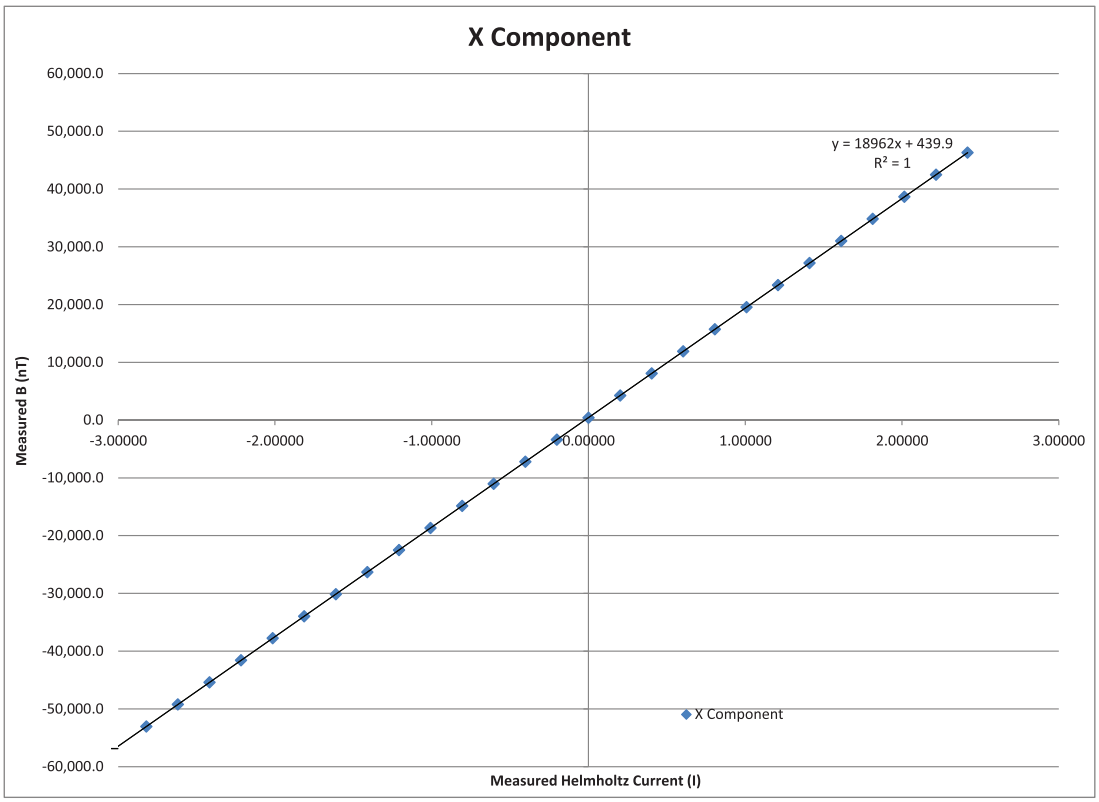

Figure 5.15: Linearity of the fluxgate magnetometer X component. Error bars too small to display.

These analyses indicate that the prototype FGM has an RMS error of 6.5 nT (X Component), 6.4 nT (Y Component) and 5.5 nT (Z Component) RMS per point. This is equivalent to

$$\frac{7 \text{ nT}}{\pm 65,536 \text{ nT}} = 0.00005 \tag{5.4}$$

or 0.005% of full scale.

5.4.4 Test 4 — Instrument Slew Rate

The FGM prototype was intended to demonstrate that an offsetting system built from 100 krad equivalent parts could track the maximum spin-field expected to be encountered by the ORBITALS spacecraft.

The spin rate test was carried out at the UAlberta CARISMA laboratory. A signal generator was used to apply a sinusoidal field of ±7,000 nT at 0.2 Hz (or twice the maximum expected magnetic slew rate of 10 second spin period). An oscilloscope was used to visualise the coarse and fine PWM signals and the error signal of the

magnetometer component under test. The pass/fail criteria was for both PWMs to remain in range and for the error signal to remain well nulled while the FGM tracked the large applied field.

Figure 5.16 shows a pass condition for the FGM test. The feedback PWM on component 1 is approximately midrange, demonstrating that the PWM is still within compliance, and the error signal on component 2 is fairly symmetric and measures less than $\pm$ 1.25 volts peak to peak (Vpp). This indicates the magnetometer is successfully tracking the changing magnetic field and that the sum of the feedback and residual error signal will correctly reconstruct the local magnetic field.

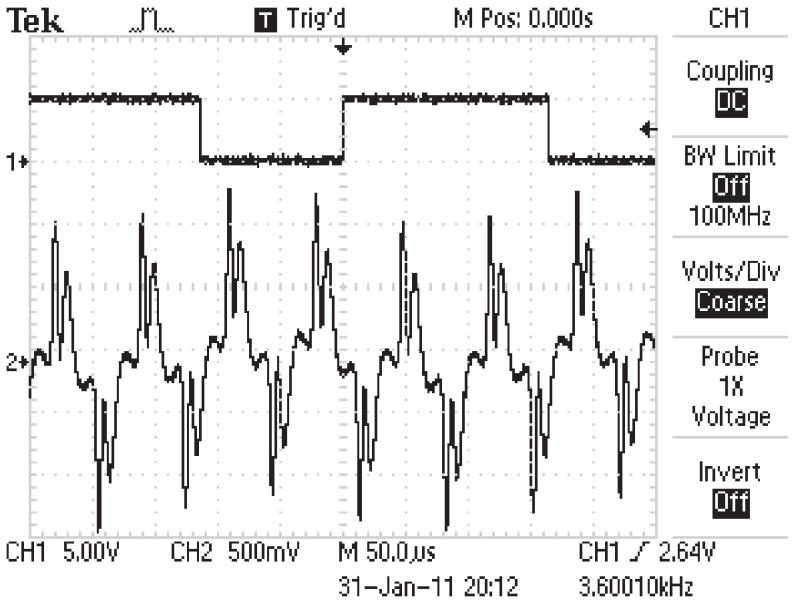

Figure 5.16: Correctly nulled instrument showing small error signal.

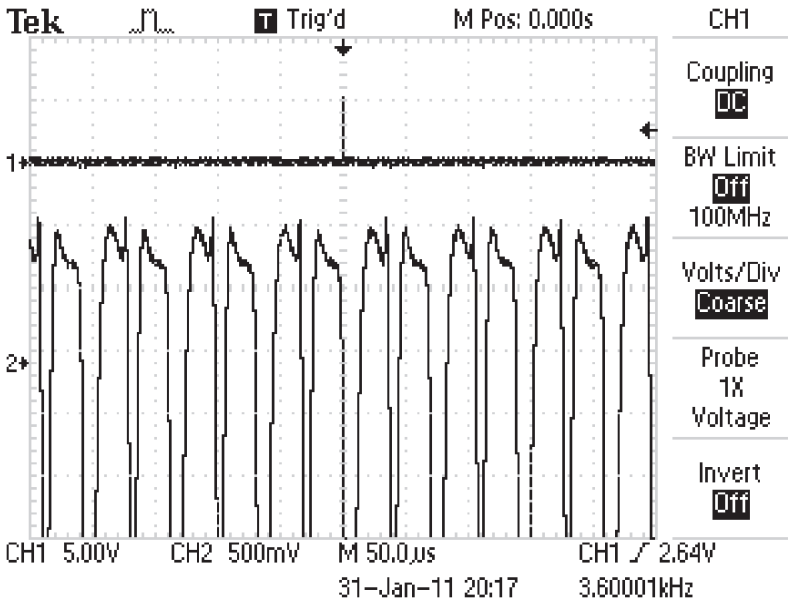

Figure 5.17: Out-of-range instrument showing large and asymmetric error signal.

Figure 5.17 shows a fail condition for the FGM test. The feedback PWM on component 1 is at one extreme, demonstrating that the PWM is out of compliance, and that the error signal on component 2 is asymmetric and large (greater than ± 1.25 Vpp). In this condition, the magnetometer is failing to track the changing magnetic field. The PWM is providing insufficient feedback, which is driving residual error signal beyond the digitising range of the ADC. Because the ADC is out of range, the sum of the feedback and the residual error signals will not correctly reconstruct the local magnetic field. The fail condition would be expected if the instrument is exposed to a magnetic slew rate much faster than the worst-case condition. During instrument development it is also diagnostic of a failure of the control loop.

Figure 5.18 shows the captured waveform for the acceptance testing of the prototype. During this test the residual error signal and feedback PWM both fulfilled the Pass Criteria. These measurements demonstrate that the prototype hardware successfully tracks the worst-case spin-field of ± 7000 nT at a 10 second period with a safety margin of two.

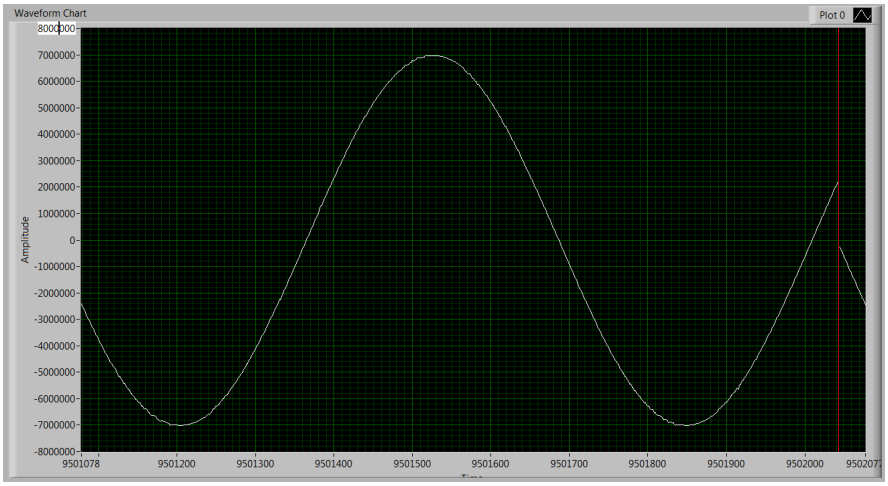

Figure 5.18: Successfully tracking the worst-case ORBITALS spin field.

5.5 Instrument Calibration

Calibrating the FGM has two major stages. First, the scaling factors for the two PWMs and the error signal for each component need to be determined to ensure that the instrument produces self-consistent data. Second, the instrument needs to be calibrated against a reliable magnetic reference to determine its absolute accuracy.

The internal scaling coefficients for each component were determined experimentally at the UAlberta CARISMA laboratory, and the instrument was then calibrated against the test facility at the NRCan Geomagnetism Laboratory. This process has five steps, which are described in the following sections.

The steps in Section 5.5.1 through 5.5.4 were completed with the sensor placed in a test solenoid within a magnetic shield. This configuration creates a small (O (10) nT per component) static field and reduces the local magnetic noise. A bench top current supply was used to create a static test signal using the solenoid. The Fluke 8845A precision multimeter was used to measure the solenoid current, which was used to calculate the applied magnetic field. Each datum is taken as the arithmetic mean of 900 samples (1 second) to suppress the environmental 60 Hz noise.

The calibration coefficients k_c, k_f, k_e, and k_o were calculated using the relationship

$$B_{applied} = k_c \cdot \text{CoarsePWM} + k_f \cdot \text{FinePWM} + k_e \cdot \text{ADCValue} + k_o \qquad (5.5)$$

5.5.1 Error Signal Scaling

Both feedback PWMs were fixed at mid-range. Ten measurements of the averaged applied magnetic field and the measured error signal were taken in the linear ±1000 nT region of the sensor. The slope of a linear fit to

$$B_{applied} = k_e \cdot \text{ADCValue} \tag{5.6}$$

determines the nT/bit scale, k_e of each ADC, which digitises the error signal from the sensor.

5.5.2 Fine Pulse Width Modulation Scaling

The fine PWM was re-enabled to allow its response to an applied field to be measured. The coarse PWM was left fixed at mid-range to remove it from the calibration. Ten measurements were taken spaced evenly through the Fine PWM duty cycle of the applied magnetic field, the Fine PWM value, and the error signal. The slope of a linear fit to

$$B_{applied} - k_e \cdot \text{ADCValue} = k_f \cdot \text{FinePWM} \tag{5.7}$$

was used to determine the nT/bit scaling, k_f, for the Fine PWM.

5.5.3 Coarse Pulse Width Modulation Scaling

Both the coarse and the fine PWMs were enabled. Ten measurements were taken spaced evenly through the Coarse PWM duty cycle of the applied magnetic field, the Coarse PWM value, the Fine PWM value, and the error signal. The slope of a linear fit to

$$B_{applied} - k_f \cdot \text{FinePWM} - k_e \cdot \text{ADCValue} = k_c \cdot \text{CoarsePWM} \tag{5.8}$$

was used to determine the nT/bit scaling, k_c, for the Coarse PWM.

5.5.4 Offset Correction

A sensor flip test was used to estimate the internal offset of the prototype and differentiate it from the small residual field in the magnetic shield where the test was conducted. The sensor was aligned in the magnetic shield and the on-axis measurement was recorded as $Value1$. The sensor was then rotated 180^o and $Value2$ was recorded. Figure 5.19 shows how $Value1$ and $Value2$ are both composed of the instrument offset and the small stray field in the shield.

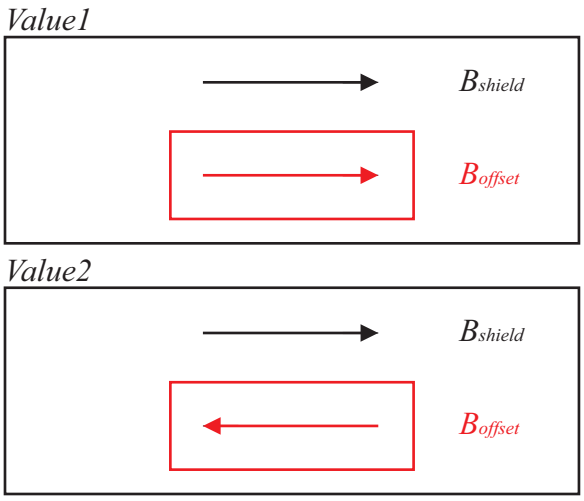

Figure 5.19: 180^o sensor rotation to estimate sensor offset.

The two measurements can be written as:

$$Value1 = B_{offset} + B_{shield} \tag{5.9}$$

$$Value2 = B_{offset} - B_{shield} \tag{5.10}$$

Therefore the offset of the instrument, k_o, is estimated by

$$\begin{aligned} k_o &= \frac{Value1 + Value2}{2} && (5.11)\\ &= \frac{B_{offset} + B_{shield} + B_{offset} - B_{shield}}{2} && (5.12)\\ &= \frac{2 \cdot B_{offset}}{2} && (5.13)\\ &= B_{offset} && (5.14) \end{aligned}$$

5.5.5 Absolute Calibration

After the previous steps were completed, the coefficients for coarse PWM, fine PWM, error signal and offset are correctly scaled with respect to each other but not yet with respect to an accepted reference. The prototype was taken to the NRCan Geomagnetics Laboratory and placed in the compensated Helmholtz coil. Each component was then stepped through a range of ±65,000 nT and measurements were taken of the constant currents applied to the Helmholtz coil at each step and measured magnetic field. The known absolute scaling factor for the coils were then used to create a nT/nT scaling factor to correct each axis and to further refine the offset for each component. The final calibration coefficients for the prototype instrument are included in Table 5.1.

Coefficient	X component (pT)	Y component (pT)	Z component (pT)
Coarse PWM	127,779	127,380	121,382
Fine PWM	490	488	465
Error Signal	57	57	54
Offset	405	38	58

Table 5.1: Calibration coefficients of prototype instrument.

5.6 Limitations of Current Prototype

The current FGM prototype has three notable limitations:

1. It has a transient ring whenever the coarse PWM changes;
2. It has a small, but non-zero, induction coil pickup at high frequencies; and
3. It does not discriminate out aliased signals above the Nyquist frequency.

Each of these issues are discussed below.

5.6.1 Step Transients

Figure 5.20 shows how the measured output of the FGM responds to an increasing magnetic field. The coarse PWM changes twice, at approximately -325 nT and -200 nT. In the firmware, the coarse PWM is changed by 1 bit and the fine PWM is simultaneously changed by an equal but opposite amount. Ideally, this would put the fine PWM back into mid-range, but would have no effect on the feedback current or the measured output. However, this change in the PWMs takes a finite time to propagate through the low-pass filters in the scaling and feedback network. Until the filters settle, the sensor experiences a different amount of feedback current than the controller is nominally applying. The damped oscillation visible in Figure 5.20 is a result of this feedback delay.

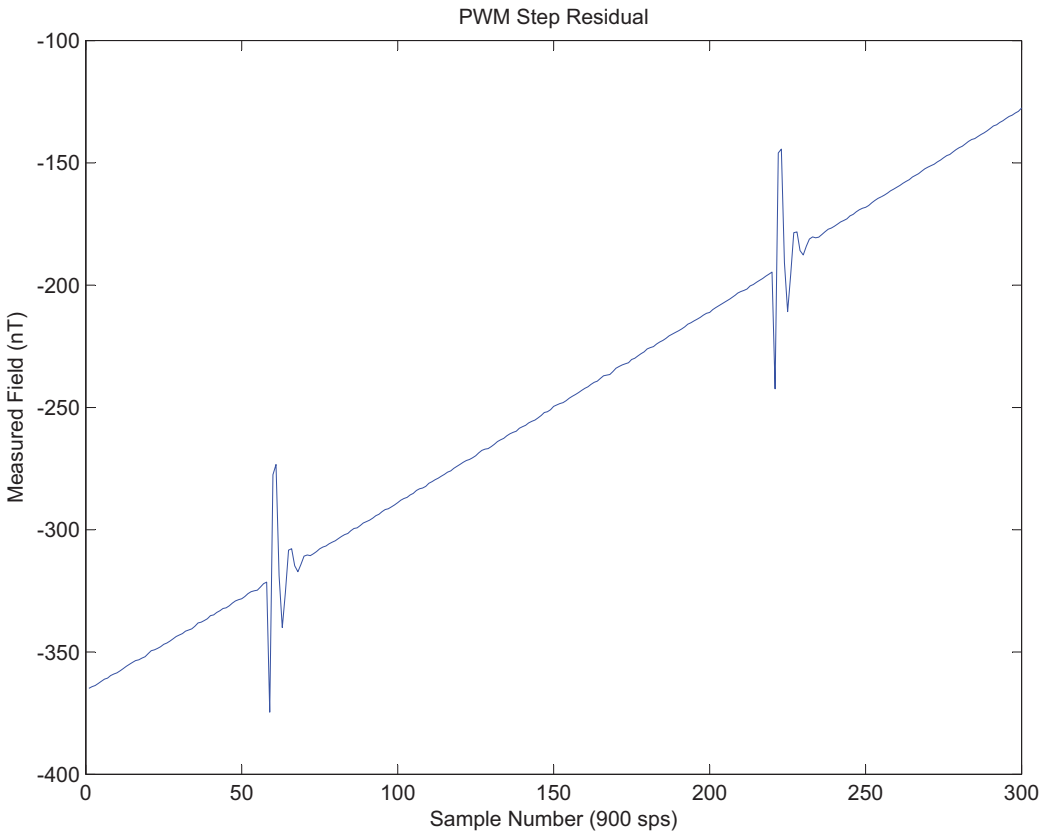

Figure 5.20: Residual contamination from coarse pulse width modulation steps.

The transient steps are consistent and repeatable, and could therefore be removed in post processing as is done on the CASSIOPE/e-POP MGF. The next hardware revision could also be designed with a faster analog switch and PWM repetition rate to reduce the amplitude and duration of these transient oscillations.

5.6.2 Induction Coil Pickup

The FGM prototype has a small, but non-zero, induction coil pickup because it does not employ a traditional analog bandpass of the error signal around the 2f frequency. Figure 5.21 illustrates the sensitivity of this induction action by operating the FGM with the core-drive electronics disabled. This is a worst case approximation as, during normal operation, the core is saturated part of the time, which reduces μ_r and hence the gain of the $(NA\mu_0\mu_r)\,\frac{dH}{dt}$ induction coil action.

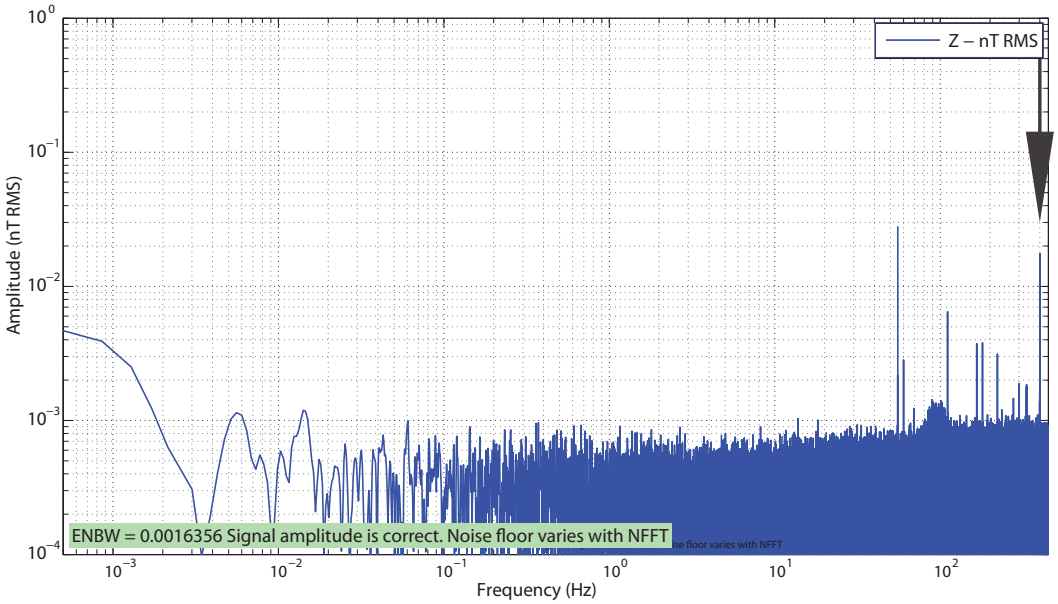

Figure 5.21: Induction coil pickup from the fluxgate magnetometer sensor. Arrow shows test signal. Amplitude spectrum - 404 pT-RMS at 400 Hz signal.

A sinusoidal test signal of 404 pT RMS with the core-drive electronics disabled was required to produce the same measurement as a 18 pT RMS test signal with the core-drive electronics enabled. This suggests that, at high frequencies, the induction coil pickup can contribute up to a 5% amplitude error. In the 0 to 10 Hz frequency range the induction coil pickup is negligible. It contributes a small variation of sensitivity with frequency, which can be calibrated out. However, at higher frequencies, a digital bandpass filter will be required to reject the base-band induction coil signal and prevent it from interfering with the 2f modulated fluxgate signal. This signal could also be isolated using a digital low-pass filter to provide additional science data at higher frequencies.

5.6.3 High Frequency Aliasing

High frequency aliasing occurs when signals that are above the Nyquist frequency appear as non-physical signals within the sampled data. Aliasing is an intrinsic problem of sampled signals and can only be prevented by ensuring that the source is filtered to have no spectral content above the Nyquist frequency.

Figure 5.22 shows how a 550 Hz test signal is measured by the FGM as an apparent 350 Hz signal (marked with an arrow). This is an aliasing effect called "frequency folding" where the aliasing signals fold over the Nyquist frequency of of 450 Hz. 550 Hz - 450 Hz = 100 Hz and 450 Hz - 100 Hz = 350 Hz. This aliasing effect occurs because the analog anti-aliasing filters were removed in the digital FGM design. In future work, this issue could be resolved using a digital low-pass filter on the raw 2f data before the signal is down-sampled into the final data product.

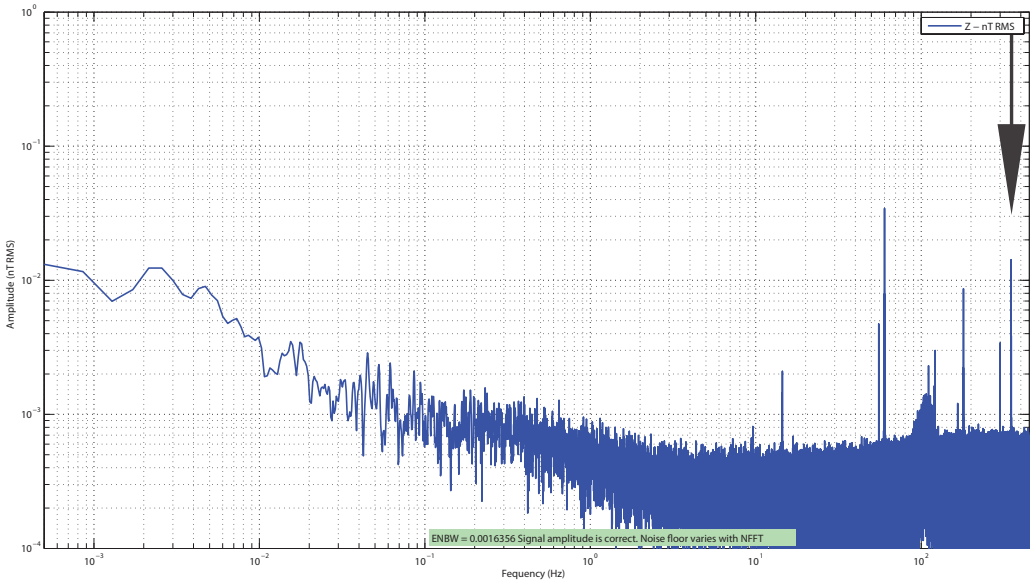

Figure 5.22: 550 Hz test signal aliased to 350 Hz. Amplitude spectrum. Arrow shows the aliased signal.

5.7 High Frequency Performance

The short-circuit coil and transimpedance amplifier topology used in this prototype is functionally the same pre-amplifier topology used by Primdahl et al. [1994] in a paper on high frequency fluxgate performance. In that paper, the authors used a more conventional digital switch synchronous detector and analog integrator. However, the functionality is very similar. Primdahl reported that the -3 dB point in the amplitude response of the instrument occurred at approximately 1,500 Hz.

Primdahl's results, and the fact that there is no obvious physical reason why the fluxgate action should decay with frequency, suggested that the AC response of the FGM should be explored. Figures 5.23, and 5.24 show two more instrument resolution plots (as in Section 5.4.1 but the arrows marking 100 Hz and 400 Hz respectively). In both cases the amplitude response of the instrument remains within -3 dB.

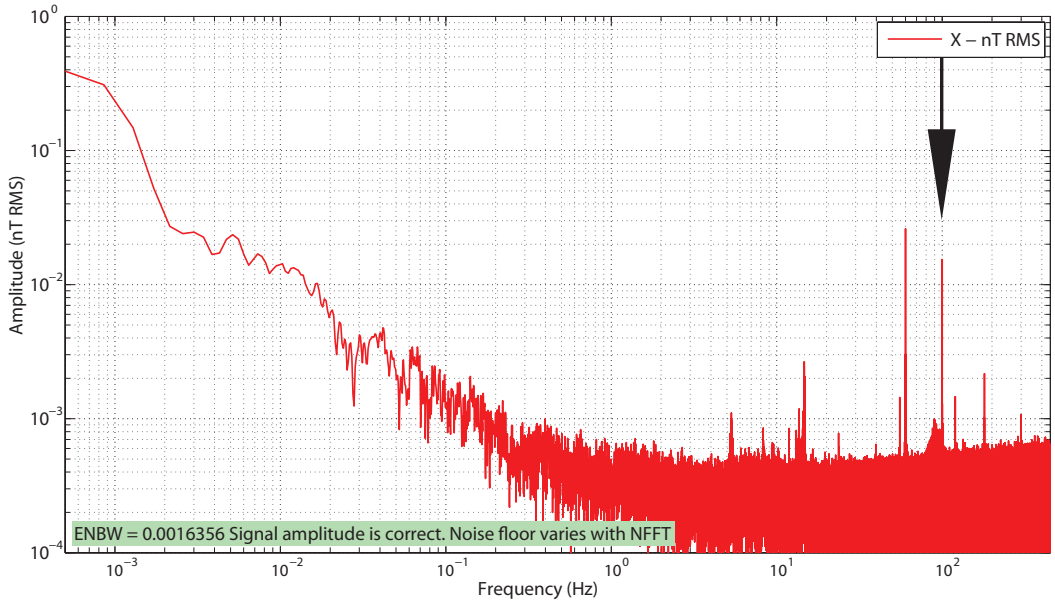

Figure 5.23: Amplitude spectrum - 18 pT-RMS at 100 Hz signal. Arrow shows test signal.

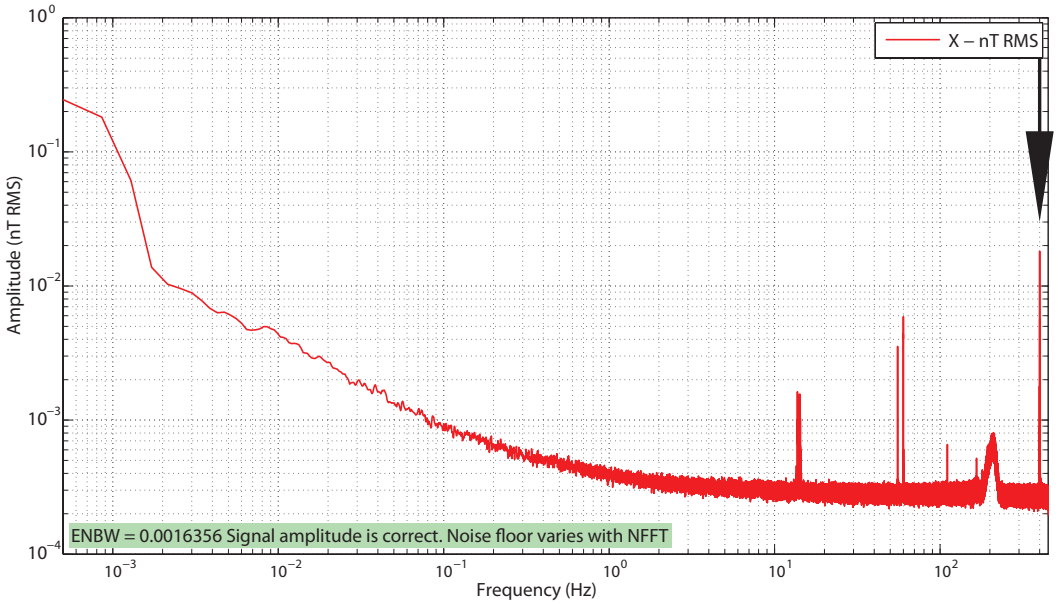

Figure 5.24: Amplitude spectrum - 18 pT-RMS at 400 Hz signal. Arrow shows test signal.

The repetition rate of the feedback PWMs limits the prototype instrument to 900 samples per second or 450 Hz Nyquist. Testing the performance of the instrument above this frequency therefore requires probing the analog pre-amplifier signal directly.

The feedback network of the instrument was temporarily disabled by fixing both the coarse and fine PWM at mid-range. In this configuration, the error signal from the pre-

amplifier is analogous to a standard Amplitude Modulation (AM) radio signal. The 2f signal replaces the carrier (frequency ω_c, amplitude A) and the applied magnetic field acts as the modulating signal (frequency ω_m, amplitude AM). As in AM radio, the result is a time series of the form:

$$y(t) = A \cdot \sin(\omega_c t) + \frac{AM}{2} \left[\sin(\omega_c + \omega_m)\, t + \sin(\omega_c - \omega_m)\, t\right] \tag{5.15}$$

This analogy allows us to visualise the fluxgate action directly from the error signal. As shown in Section 4.9.1, the 2f carrier frequency shows as a spectral feature at 57,600 Hz whose amplitude is dependent on the static field strength. However, an applied AC test signal will appear as two sideband carriers at 57,600 Hz plus or minus the AC signal frequency. The panels in Figure 5.25 show the resulting spectral plots for: no test signal, 100 Hz, 200 Hz, 500 Hz, 1,000 Hz, and 1,500 Hz respectively. Note that the amplitude of the sideband carriers is constant with frequency up to 1,500 Hz, and that there are no other large amplitude features within this frequency range. This suggests that if the PWM frequency and sampling frequency were increased, the prototype fluxgate could provide valid data up to at least 1,500 Hz.

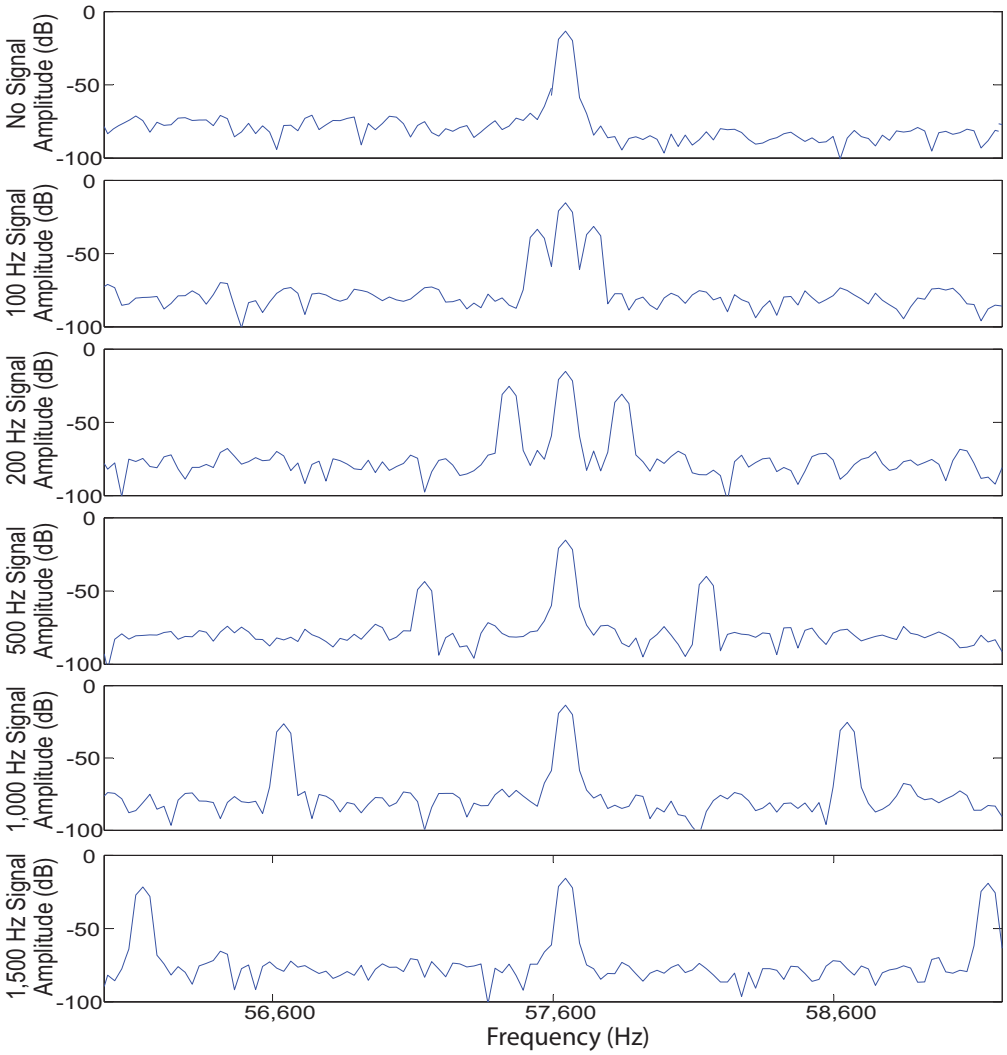

Figure 5.25: Spectral analysis of the directly sampled error signal shows the modulation $2f$ major carrier sidebands by applied sinusoidal magnetic signals up to 1,500 Hz.

Chapter 6

Conclusions and Future Work

6.1 Comparison of Prototype to Previous Designs

Table 6.1 compares the performance of the current radiation hardened prototype instrument to the state-of-the-art established in Chapter 3 by previous, generally much less radiation tolerant, spaceflight fluxgate magnetometers.

Parameter	State of the art	Current Prototype
Range	± 65,000 nT	± 65,536 nT
Resolution	0.010 nT	0.008 nT
Cadence	100 sps	900 sps
Noise	10 pT/$\sqrt{\text{Hz}}$ at 1 Hz	< 10 pT/$\sqrt{\text{Hz}}$ at 1 Hz
Power	< 1 W	1.5 W (2.5 W with reference heater)

Table 6.1: Current prototype compared to the state-of-the-art spaceflight fluxgate.

The current radiation hardened prototype presented in this thesis matches the state-of-the-art in measurement range, resolution, noise, while sampling at a cadence almost an order of magnitude faster than most other instruments. This performance is achieved using only parts that are functionally equivalent to available 100 krad tolerant, space grade components and without the use components with embedded shielding. Embedded shielding, while commonly used in lower radiation applications, is ineffective in the intense radiation of the Van Allen belts where the spacecraft and electronics box already provide significant shielding. This performance is achieved by implementing most of the signal conditioning in digital processing. However, this novel design combines digital design techniques with the analog temperature compensation needed to provide accurate measurements over a broad range of mission temperatures.

The current prototype draws more power than most spaceflight fluxgates due to its construction from parts that are functionally equivalent to 100 krad tolerant parts. Both the radiation hardened parts and their functionally equivalents are generally based on older, higher power electronics processes than those used in low-radiation applications. The prototype provides the option to expend increased power in a thermally stabilized voltage reference to provide improved long-term stability. Overall, the prototype

provides state-of-the-art science performance, significantly improved high frequency performance, and robust radiation tolerance suitable harsh radiation of the Van Allen radiation belts.

6.2 Performance Versus Mission Requirements

Table 6.2 compares the prototype instrument to the requirements and constraints defined in Chapter 2. The current values have been established by direct measurements when practical and by estimation based on the existing prototype when direct measurement was impractical or premature. For example, the power consumption of the combined payload of two instruments is calculated as twice the consumption of one prototype. Finally, some parameters are listed as compliant "by design" when the instrument was designed to meet a requirement; however, it is not yet appropriate or useful to verify the parameter. For example, for the ORBITALS application, the electronics box is intended to have 7 mm aluminium wall, but has not yet been constructed. Validation of some parameters has been listed as "deferred" where the requirement is not yet fully defined or is dependent on other instruments or hardware not available during the course of this thesis.

Parameters	Requirement	Current Value	Compliant	Comment
Resolution	< 0.1 nT	0.008 nT	Yes	Measured
Cadence	≥ 128 sps	900 sps	Yes	By Design
AC Range	≥ 10 Hz	450 Hz	Yes	Measured
Noise Floor	≤ 20 pT/$\sqrt{\text{Hz}}$ at 1 Hz	10 pT/$\sqrt{\text{Hz}}$ at 1 Hz	Yes	Measured
Phase Response	$\leq \pm 180^0$ (0 - 10 Hz)	TBD	TBD	Deferred
Amplitude Accuracy	$\leq 0.1\%$	0.005%	Yes	Measured
Timing Accuracy	≤ 40 μs	0.067 μs	Yes	By Design
FGM/EFW Timing	≤ 0.2 ms (40 μs goal)	TBD	TBD	Deferred
Peak Power (2 units)	≤ 5 W	5 W	Yes	Estimated
Electronics Mass	≤ 5 kg	2.5 kg	Yes	Estimated
Electronics Dimensions	$\leq$ 150x150x100 mm	150x150x30 mm	Yes	Estimated
Sensor Heat Generation	≤ 100 mW	TBD	TBD	Deferred
Average Telemetry Rate	≤ 6.8 kbps	2.5 kbps at 32 sps	Yes	Estimated
EMC	TBD	TBD	TBD	Deferred
TID Tolerance	≥ 100 krad	100 krad	Yes	By Design
Radiation Shielding	$\geq 7 + 1$ mm Al	7 + 1 mm Al	Yes	By Design
Single Event Threshold	≥ 35 LET	35 LET	Yes	By Design
Sensor Survival Temp	-55 to $+85^o$c	-55 to $+85^o$c	Yes	By Design
Sensor Operating Temp	-40 to $+60^o$c	-40 to $+60^o$c	Yes	By Design
Elect. Survival Temp	-55 to $+85^o$c	-55 to $+85^o$c	Yes	By Design
Elect. Operating Temp	-40 to $+50^o$c	-40 to $+50^o$c	Yes	By Design
Dual FGM units	Fully Independent	Fully Independent	Yes	By Design
18 Month Reliability	≥ 0.978 for payload	0.978	Yes	Estimated
Storm Operation	Operate During	TBD	TBD	Deferred
Product Assurance	TBD	TBD	TBD	Deferred

Table 6.2: Performance of prototype instrument against mission requirements (Section 2.2.3) and constraints (Section 2.3.7).

Table 6.2 shows that the FGM, when fully developed, will be compliant with the ORBITALS requirements. The current prototype has demonstrated and experimen-

tally verified all the critical instrument characteristics. This state of development exceeds that expected for an instrument at the end of the Phase A concept study and demonstrates that the instrument is ready to proceed to a design phase and then construction for a future space physics mission.

6.3 Conclusions

Space-based measurements of the Earth's magnetic field and the plasma waves it supports are required to understand the plasma processes that cause the solar-terrestrial interactions that energize the Van Allen radiation belts and cause space weather. The prototype fluxgate magnetometer developed for this thesis meets both the scientific and the programmatic requirements for making high fidelity magnetic field measurements on the Canadian Space Agency's ORBITALS small satellite mission.

The prototype instrument can resolve 8 pT on a 65,000 nT field at 900 samples per second with a magnetic noise of less than 10 pT/$\sqrt{\text{Hz}}$ at 1 Hz. The magnetometer is designed to be radiation tolerant to 100 krad and to be entirely constructed from space grade (Class S) parts. It is based on the CASSIOPE/e-POP MGF instrument and uses a novel digital feedback process to improve the sampling rate and resolution while reducing complexity, parts count and physical size. If the prototype was constructed from commercial grade parts, it could form the basis of a low-cost instrument for terrestrial applications where radiation hardening is not required.

The prototype instrument was successfully validated at the NRCan Geomagnetics Laboratory in Ottawa, ON, Canada. Test results suggest that the instrument could be modified to provide useful magnetic measurements at rates of at least 3,000 samples per second. This improved high frequency performance makes the instrument suitable for a variety of applications including sub-orbital sounding rockets.

6.4 Future Work

Several future space-physics programs and missions, which could use Canadian instrument provision for in-situ magnetic measurements, have been identified including: the PRIMO payload on the CSA's PCW mission, the proposed CSA I-SWEAT satellite, the JAXA/CSA SCOPE collaboration, and Norwegian ICI-4 sounding rocket program. The science and technical requirements for these missions should be estimated so that, if possible, the next iteration of the FGM instrument can address the combined requirements of these proposed programs. Multi-mission flexibility would reduce the amount of redesign and re-qualification required and provide a lower cost instrument through a manufacturing economy of scale.

The current prototype was built using the engineering model CASSIOPE/e-POP sensor with legacy, low noise Infinetics ring cores. A very limited supply of these legacy cores exist so the re-use of this magnetometer design for future missions will require a new source of low-noise ring cores. Narod Geophysics Ltd. is undertaking research that may provide an alternative source. However, the final specifications and availability of

these cores remains to be determined. In the absence of these cores, the instrument can be constructed from existing and available higher noise cores; however, the noise floor will be degraded to about 30 pT/$\sqrt{\text{Hz}}$ at 1 Hz. Future work should include identifying or developing low-noise cores for future missions.

Firmware based digital filtering of the raw sensor samples should be implemented to either remove the induction coil component of the sensor output or capture it and create a high-frequency data product. Digital anti-aliasing filtering should also be implemented to prevent high-frequency signals above the Nyquist frequency from aliasing into the measured data as noise. The firmware should be expanded to provide configurable down-sampling rates allowing the instrument to be rapidly configured for applications with different and/or dynamic science objectives and telemetry requirements. The firmware could also be modified to provide in-flight calibration but the risks and benefits of the added complexity should be assessed on a case by case basis. Finally, the firmware should be migrated to a flash based Actel FPGA architecture to provide a closer analog to the radiation hardened flight hardware.

The prototype was built using two printed circuit boards, one for the digital electronics and one for the analog electronics. This was convenient for development and reduced the costs of successive hardware iterations. However, the design is now sufficiently far advanced that the two electronics cards should be merged together. Most of the in-circuit test hardware is no longer required and can be removed, and the instrument should be tested as a single unit. The power draw measurements should be repeated with the development and testing hardware removed to better quantify the power requirements of the instrument. The instrument's power supply and the power supply rejection ratio should be improved to remove the double-peaked noise feature between 200 and 300 Hz seen in the PSD noise floor of the instrument. The thermal testing should be repeated to ensure that the concentrated heat of the fully integrated instrument does not cause thermal hot spot issues. The commercial grade hardware should be calibrated and tested for use in terrestrial ground applications such as in magnetotelluric surveys for geophysics.

The drive frequency of the sensor should be doubled to 57.6 kHz to reduce potential high-frequency magnetic interference with any search coil type high frequency magnetometer that might also be flown as part of the payload of a future mission. This will also double the amount of raw measurements and should add another 1/2 bit of resolution. A faster analog switch or a third PWM on each component could be added to increase the speed of the digital feedback loop and the bandwidth of the instrument. Faster digital feedback may also require a more sophisticated control algorithm (likely a PID controller) to allow the instrument to track very high slew rates.

Bibliography

Acuña, M. H. (1974). Fluxgate magnetometers for outer planets exploration. *IEEE T.Mag*, *10*, 519–523.

Acuña, M. H., Connerney, J. E. P., Ness, N. F., Lin, R. P., Mitchell, D., Carlson, C. W., McFadden, J., Anderson, K. A., Rème, H., Mazelle, C., Vignes, D., Wasilewski, P., & Cloutier, P. (1999). Global distribution of crustal magnetization discovered by the mars global surveyor mag/er experiment. *Science*, *284*(5415), 790–793.

Acuña, M. H. & Ness, N. F. (1975). The Pioneer XI high field fluxgate magnetometer. Technical report.

Acuña, M. H., Scearce, C. S., Seek, J., & Scheifele, J. (1978). The MAGSAT vector magnetometer: A precision fluxgate magnetometer for the measurement of the geomagnetic field. Technical report.

Angelopoulos, V., Sibeck, D., Carlson, C., McFadden, J., Larson, D., Lin, R., Bonnell, J., Mozer, F., Ergun, R., Cully, C., et al. (2008). First results from the THEMIS mission. *Space Science Reviews*, *141*(1), 453–476.

Auster, H., Glassmeier, K., Magnes, W., Aydogar, O., Baumjohann, W., Constantinescu, D., Fischer, D., Fornacon, K., Georgescu, E., Harvey, P., Hillenmaier, O., Kroth, R., Ludlam, M., Narita, Y., & Nakamura, R. (2008). The THEMIS Fluxgate Magnetometer. *Space Science Reviews*, *141*, 235–264. 10.1007/s11214-008-9365-9.

Avery, K., Finchel, J., Mee, J., Kemp, W., Netzer, R., Elkins, D., Zufelt, B., & Alexander, D. (2011). Total dose test results for cubesat electronics. In *Radiation Effects Data Workshop (REDW), 2011 IEEE*, (pp. 1 –8).

Baker, D. (1998). What is space weather? *Adv. Space Res.*, *22*(1), 7–16.

Bennett, S. (1993). *A History of Control Engineering, 1930-1955*. IEEE Control Engineering Series. P. Peregrinus.

Bobrinsky, N. & Monte, L. D. (2010). The space situational awareness program of the european space agency. *Cosmic Research*, *48*(5), 392–398.

Bolduc, L. (2002). GIC observations and studies in the Hydro-Québec power system. *Journal of Atmospheric and Solar-Terrestrial Physics*, *64*(16), 1793–1802.

Carr, C., Brown, P., Zhang, T., Gloag, J., Horbury, T., Lucek, E., Magnes, W., O'Brien, H., Oddy, T., Auster, U., et al. (2005). The double star magnetic field investigation: instrument design, performance and highlights of the first year's observations. In *Annales Geophysicae*, volume 23, (pp. 2713–2732).

Dungey, J. W. (1963). The structure of the exosphere or adventures in velocity space. In C. DeWitt-Morette (Ed.), *Geophysique extérieure: Geophysics: the earth's environment*. Gordon and Breach.

Eaton, D. W., Adams, J., Asudeh, I., Atkinson, G. M., Bostock, M. G., Cassidy, J. F., Ferguson, I. J., Samson, C., Snyder, D. B., Tiampo, K. F., & Unsworth, M. J. (2005). Investigating Canada's Lithosphere and earthquake hazards with portable arrays. *EOS Transactions*, *86*, 169–173.

Escoubet, C., Fehringer, M., Goldstein, M., et al. (2001). The Cluster mission. In *Annales Geophysicae*, volume 19, (pp. 1197–1200).

Fennell, J., Koons, H., Chen, M., & Blake, J. (2000). Internal charging: a preliminary environmental specification for satellites. *Plasma Science, IEEE Transactions on*, *28*(6), 2029 –2036.

Forslund, A., Belyayev, S., Ivchenko, N., Olsson, G., Edberg, T., & Marusenkov, A. (2008). Miniaturized digital fluxgate magnetometer for small spacecraft applications. *Measurement Science and Technology*, *19*(1), 015202.

Freden, S. & White, R. (1962). Trapped proton and cosmic-ray albedo neutron fluxes. *Journal of Geophysical Research*, *67*(1), 25–29.

Fujimoto, M., Tsuda, Y., Saito, Y., Shinohara, I., Takashima, T., Matsuoka, A., Kojima, H., & Kasaba, Y. (2009). The SCOPE mission. *AIP Conference Proceedings*, *1144*(1), 29–35.

Halekas, J., Delory, G., Brain, D., Lin, R., & Mitchell, D. (2008). Density cavity observed over a strong lunar crustal magnetic anomaly in the solar wind: A mini-magnetosphere? *Planetary and Space Science*, *56*(7), 941 – 946.

Hargreaves, J. (1979). *The upper atmosphere and solar-terrestrial relations: an introduction to the aerospace environment*. Van Nostrand Reinhold.

Harris, F. (1978). On the use of windows for harmonic analysis with the discrete fourier transform. *Proceedings of the IEEE*, *66*(1), 51 – 83.

Heinzel, G. (2002). Spectrum and spectral density estimation by the discrete fourier transform (DFT), including a comprehensive list of window functions and some new flat-top windows. Technical report, Max-Planck-Institut fur Gravitationsphysik, Teilinstitut Hannover.

Holdrew, J. P. & Beddington, J. (2011). Celestial storm warnings. The New York Times, March 10, 2012.

Irom, F. (2006). Interoffice memorandum electronic parts engineering office - latchup rates for the Linear Technology LTC1604 Analog to Digital Converter. Technical report.

Keiling, A., Wygant, J., Cattell, C., Mozer, F., & Russell, C. (2003). The global morphology of wave poynting flux: Powering the aurora. *Science*, *299*(5605), 383–386.

Kivelson, M. & Russell, C. (1995). *Introduction to space physics*. Cambridge atmospheric and space science series. Cambridge University Press.

Kletzing, C. (2011). Forthcoming measurements of plasma waves by the EMFISIS investigation on the RBSP spacecraft. In *General Assembly and Scientific Symposium, 2011 XXXth URSI*, (pp. 1 –2).

Li, W., Thorne, R. M., Angelopoulos, V., Bortnik, J., Cully, C. M., Ni, B., LeContel, O., Roux, A., Auster, U., & Magnes, W. (2009). Global distribution of whistler-mode chorus waves observed on the THEMIS spacecraft. *Geophysical Research Letters*, *36*, 9104.

Li, X., Baker, D., O'Brien, T., Xie, L., & Zong, Q. (2006). Correlation between the inner edge of outer radiation belt electrons and the innermost plasmapause location. *Geophysical research letters*, *33*(14), L14107.

Liu, K., Gary, S. P., & Winske, D. (2011). Excitation of magnetosonic waves in the terrestrial magnetosphere: Particle-in-cell simulations. *Journal of Geophysical Research (Space Physics)*, *116*, 7212.

Luehr, H., Kloecker, N., Oelschlaegel, W., Haeusler, B., & Acuña, M. (1985). The IRM fluxgate magnetometer. *IEEE Transactions on Geoscience and Remote Sensing*, *23*, 259–261.

Magnes, W., Oberst, M., Valavanoglou, A., Hauer, H., Hagen, C., Jernej, I., Neubauer, H., Baumjohann, W., Pierce, D., Means, J., & Falkner, P. (2008). Highly integrated front-end electronics for spaceborne fluxgate sensors. *Measurement Science and Technology*, *19*(11), 115801.

Magnes, W., Pierce, D., Valavanoglou, A., Means, J., Baumjohann, W., Russell, C. T., Schwingenschuh, K., & Graber, G. (2003). A sigmadelta fluxgate magnetometer for space applications. *Measurement Science and Technology*, *14*(7), 1003.

Mann, I., Loto'aniu, P. T. M., Ozeke, L. G., Yau, A., Kale, Z., Miles, D., & Hum, B. (2009). ORBITALS Mission Requirements Document (MRD) - Revision B. Technical report, University of Alberta for the Canadian Space Agency.

Mann, I., Milling, D., Rae, I., Ozeke, L., Kale, A., Kale, Z., Murphy, K., Parent, A., Usanova, M., Pahud, D., Lee, E.-A., Amalraj, V., Wallis, D., Angelopoulos, V., Glassmeier, K.-H., Russell, C., Auster, H.-U., & Singer, H. (2008). The upgraded CARISMA magnetometer array in the THEMIS era. *Space Science Reviews*, *141*, 413–451. 10.1007/s11214-008-9457-6.

Mann, I., Rae, I. J., Ozeke, L., Miles, D., & Yau, A. (2011). Plasma and Radiation In Molniya Orbit (PRIMO) Science Objective and User's Needs Definition Document. Technical report, Universities of Alberta and Calgary for the Canadian Space Agency.

Mann et al. (2006). The outer radiation belt injection, transport, acceleration and loss satellite (ORBITALS): A canadian small satellite mission for ILWS. *Adv. Space Res.*, *38*.

Maxwell Technologies (2009). 7872A 14-bit A/D Converter. Technical report, Maxwell Technologies.

McClure, S., Garrett, H., Jun, I., Oldham, T. R., Baze, M., & Ecoffet, R. (2011). Course space radiation environments and their effects on devices and systems: Back to the basics. 2011 IEEE Nuclear and Space Radiation Effects Conference Short Course.

Millan, R. & Thorne, R. (2007). Review of radiation belt relativistic electron losses. *Journal of Atmospheric and Solar-Terrestrial Physics*, *69*(3), 362 – 377. Global Aspects of Magnetosphere-Ionosphere Coupling.

Milling, D., Miles, D., & Mann, I. (2009). ORBITALS flux gate magnetometer (FGM) instrument specification document. Technical report, University of Alberta Department of Physics.

Milling, D., Miles, D., Mann, I., & Ciurzynski, M. (2011). ORBITALS Search Coil Magnetometer Phase A2 - Instrument Design Document. Technical report, University of Alberta Department of Physics.

Moffat, B. & Girard, T. (2011). ORBITALS Magnetometers Phase A2 Final Report. Technical report, COM DEV.

Narod, B. & Bennest, J. (1990). Ring-core fluxgate magnetometers for use as observatory variometers. *Physics of the Earth and Planetary Interiors*, *59*(1-2), 23 – 28.

Ness, N. F., Behannon, K. W., Lepping, R. P., & Schatten, K. H. (1971). Use of two magnetometers for magnetic field measurements on a spacecraft. *Journal of Geophysical Research*, *76*, 3564–3573.

O'Brien, H., Brown, P., Beek, T., Carr, C., Cupido, E., & Oddy, T. (2007). A radiation tolerant digital fluxgate magnetometer. *Measurement Science and Technology*, *18*(11), 3645.

Ozeke, L. & Mann, I. (2011). ORBITALS Mission Radiation and Surface Charging: Worst Case Particle Flux, TID and DDC estimates. Technical report, University of Alberta, Department of Physics, Edmonton, Alberta, Canada.

Pedersen, E. B., Primdahl, F., Petersen, J. R., Merayo, J. M. G., Brauer, P., & Nielsen, O. V. (1999). Digital fluxgate magnetometer for the Astrid-2 satellite. *Measurement Science and Technology*, *10*(11), N124.

Primdahl, F., Nielsen, O., Petersen, J., & Ripka, P. (1994). High frequency fluxgate sensor noise. *Electronics Letters*, *30*(6), 481 –482.

Rae, I. J., Miles, D., Barona, D., & Silin, I. (2011). Science Data Downlink and Data Rate Allocation Report - ORBITALS Mission and Instrument Extended Phase A. Technical report, University of Alberta Department of Physics.

Ratcliffe, J. A. (1972). *An Introduction to Ionosphere and Magnetosphere*. Cambridge University Press.

Ripka, P. (2001). *Magnetic Sensors and Magnetometers*. 685 Canton Street, Northwood, MA, 02062: Artech House, Inc.

Rooney, S. & Frye, M. A. (2008). 5962-95813 microcircuit, linear radiation hardened cmos, dual spdt analog switches, monolithic silicon. Standard Microcircuit Drawing. Defense Supply Center Columbus, Columbus, OHIO, 43218-3990.

Rostoker, G., Samson, J., Creutzberg, F., Hughes, T., McDiarmid, D., McNamara, A., Jones, A., Wallis, D., & Cogger, L. (1995). Canopusa ground-based instrument array for remote sensing the high latitude ionosphere during the istp/ggs program. *Space Science Reviews*, *71*(1), 743–760.

Schultz, A. (2009). Emscope: A continental scale magnetotelluric observatory and data discovery resource. *Data Science Journal*, *8*, IGY6–IGY20.

Shea, M. A. & Smart, D. F. (1998). Space weather: The effects on operations in space. *Adv. Space Res.*, *22*(1), 29–32.

Singer, H. J., Sullivan, W. P., Anderson, P., Mozer, F., Harvey, P., Wygant, J., & McNeil, W. (1992). Fluxgate magnetometer instrument on the CRRES. *Journal of Spacecraft and Rockets*, *29*, 599–601.

Thomas, D., Shaw, M., Lee, P., Griffin, G., Duggan, P., Aktik, M., Schaulthess, H., & Roald, K. (2006). CASSIOPE environmental requirements and test specifications. Technical report, MacDonald, Dettwiler and Associates Ltd.

Trishchenko, A. & Garand, L. (2011). Spatial and temporal sampling of polar regions from two-satellite system on molniya orbit. *Journal of Atmospheric and Oceanic Technology*, *28*(8), 977–992.

Usanova, M. E., Mann, I. R., Rae, I. J., Kale, Z. C., Angelopoulos, V., Bonnell, J. W., Glassmeier, K. H., Auster, H. U., & Singer, H. J. (2008). Multipoint observations of magnetospheric compression-related EMIC Pc1 waves by THEMIS and CARISMA. *Geophysical Research Letters*, *35*, 17.

Vaivads, A., Andersson, G., Bale, S. D., Cully, C. M., Keyser, J. D., Fujimoto, M., Grahn, S., Haaland, S., Ji, H., Khotyaintsev, Y. V., Lazarian, A., Lavraud, B., & Mann, I. R. (2011). EIDOSCOPE: particle acceleration at plasma boundaries. *Physics and Astronomy, Experimental Astronomy*.

Wallis, D. D., Narod, B. B., & Bennest, J. R. (2006). The ePOP / CASSIOPE Magnetic Field Instrument. Annual Geophysical Meeting.

Walt, M. (2005). *Introduction To Geomagnetically Trapped Radiation*. Cambridge Atmospheric and Space Science Series. Cambridge University Press.

Welch, P. (1967). The use of fast fourier transform for the estimation of power spectra: a method based on time averaging over short, modified periodograms. *Audio and Electroacoustics, IEEE Transactions on*, *15*(2), 70–73.

Wilson, III, L. B., Cattell, C. A., Kellogg, P. J., Wygant, J. R., Goetz, K., Breneman, A., & Kersten, K. (2011). The properties of large amplitude whistler mode waves in the magnetosphere: Propagation and relationship with geomagnetic activity. *Geophysical Research Letters*, *38*, 17107.

Yau, A., Langley, R. B., Noel, J., Wallis, D. D., Harrison, P., & Lunscher, W. (2008). A new atmospheric neutral analyzer instrument for thermospheric composition, density and wind velocity measurements on the ISWEAT micro-satellite. American Geophysical Union, Fall Meeting. Abstract SA23A-08.

Appendix A

Spectral Analysis

A.1 Techniques Used In This Thesis

Frequency domain analysis using a DFT is a powerful tool for characterising the frequency dependent performance parameters of a fluxgate magnetometer. Some properties, such as the nT^2/Hz noise floor of the instrument are most easily calculated using a DFT. However, parameters such as the number of bins in the transform, window type, averaging, and normalisation can have an enormous impact on the inferred response derived on the basis of a spectral transform. Many authors in the literature are imprecise about the algorithm used and the details of how their calculations were conducted, making it difficult to accurately compare to their results. This section describes the approach to spectral analysis used in this thesis and follows the excellent review of spectrum and spectral density estimation by Heinzel [2002].

Two types of analysis are used in this thesis. Amplitude spectra (in units of nT) are used to determine the sensitivity and accuracy of the FGM's measurement of a magnetic sinusoidal test signal. Power spectral density (in units of nT^2/Hz) is used to characterise the noise floor of the instrument. By convention, the noise floor of the instrument is often quoted in units if $nT/\sqrt{Hz}$, which is the square root of PSD. In both cases, the technique used is a overlapped segmented averaging of a modified periodogram. Here we use the term periodogram to refer to a Discrete Fourier Transform (DFT) of one segment of a long time series, which is modified by the application of a time domain window function. A succession of these periodograms are then averaged to reduce the variance of the spectral estimation. Overlapping segments are taken from the original time series to avoid discarding signal from the application of a window function. This method is often referred to as "Welch's Algorithm" [Welch, 1967] and is provided by the Matlab signal processing toolbox as the "pwelch" function.

A.2 Types of Fourier Transforms

The generalised discrete Fourier transform takes a vector of N samples of the time series data $x_k, k = 0, 1, ..., N-1$ and produces a vector of N complex numbers $y_m, m = 0, 1, ..., N-1$ representing the frequency content as derived from the application of a DFT. Equations A.1, A.2, and A.3 show three common definitions of the DFT, which differ only in how they are normalized.

$$y_m^{(1)} = \sum_{k=0}^{N-1} x_k \exp\left(-2\pi i \frac{mk}{N}\right), m = 0, 1, ..., N-1 \tag{A.1}$$

$$y_m^{(2)} = \frac{1}{\sqrt{N}} y_m^{(1)} \tag{A.2}$$

$$y_m^{(3)} = \frac{1}{N} y_m^{(1)} \tag{A.3}$$

The reverse transforms have the opposite sign in the exponential and require different normalisation. (e.g., $+2\pi i \frac{mk}{N}$ rather than $-2\pi i \frac{mk}{N}$ see Heinzel [2002] for complete details). Equations A.1, A.2, and A.3 are equally valid mathematically (all satisfy Parsevals theorem) although Equation A.2 is sometimes preferred since the normalisation term, $1/\sqrt{N}$, is symmetric in the forward and backward transform.

Equation A.3 normalises the output of the DFT against changes in N. Without this normalisation, as N increases the output values of the DFT to grow in proportion to N.

The scripts used to analyse magnetometer time series data in this thesis (Sections A.5.2 and A.5.1) use the Matlab pwelch function, which uses the FFTW library to calculated an optimised DFT using Equation A.1. Normalisation against N is included in a normalisation coefficient called Effective Noise Bandwidth (ENBW) (see Section A.4.1), which converts the output into physical units. Other software packages (e.g., IDL) may calculate a different DFT and may need to be normalised differently.

A.3 Converting Between Amplitude and PSD

Consider a hypothetical test signal with two components: a sinusoid magnetic field with a magnitude of 1 nT and white noise with a power spectral density of 0.1 nT^2/Hz. An ideal spectral transform would simultaneously characterize both outputs. However, it is obvious from the units (nT vs nT^2/Hz) that different scaling and approaches are required to measure the two parameters.

Table A.1 shows four different ways to express the results of a DFT, their inter-relationships, and their units assuming that the input time series is in units of nT.

Abbrev.	Name	Relation	Unit
PSD	Power Spectral Density		nT^2/Hz
PS	Power Spectrum	$\text{PS} = \text{PSD} \cdot \text{ENBW}$	nT^2
LSD	Linear Spectral Density Amplitude Spectral Density	$\text{LSD} = \sqrt{\text{PSD}}$	$\text{nT}/\sqrt{\text{Hz}}$
LS	Linear Spectrum Amplitude Spectrum	$\text{LS} = \sqrt{\text{PS}} = \text{LSD} \cdot \sqrt{\text{ENBW}}$	nT

Table A.1: Naming conventions, inter-relationships, and units for different DFT outputs assuming the input signal is in units of nT. ENBW is defined in Equation A.4. Following from Heinzel [2002].

Effective Noise Bandwidth (ENBW) is a normalisation coefficient for the window function and is described in Section A.4.1. At this stage, it is sufficient to note that it is

not possible to convert from a PSD spectrum to an amplitude spectrum and maintain physically significant units without the use of the ENBW scaling factor. For this reason, the ENBW scaling factor used is shown explicitly on all the spectral plots shown in Chapter 5.

A.4 Parameter Selection

Five factors need to be considered when using a DFT to make quantitative measurements from a time series. The DFT output must be normalised into physical units, the number of spectral bins must provide sufficient amplitude and spectral resolution, an appropriate window function must be selected for the parameter being measured, the minimum potential spectral separation of signals must be checked, and the affect and potential necessity of averaging must be assessed. Each of these parameters is discussed below.

A.4.1 Normalisation of the DFT

ENBW, the normalisation term used to preserve the physical units of the input time series, is calculated as

$$\text{ENBW} = \text{NENBW} \cdot \frac{f_s}{N} \tag{A.4}$$

Where f_s is the sampling frequency, N is in the number of frequency bins in the DFT, and Normalised Effective Noise Bandwidth (NENBW) is specific to the window function used. NENBW is calculated as

$$\text{NENBW} = N\frac{S_2}{(S_1)^2} \tag{A.5}$$

Where S_1 and S_2 are calculated for a particular window as the sum of the coefficients w_j, which define the window function at each of N points.

$$S_1 = \sum_{j=0}^{N-1} w_j \tag{A.6}$$

$$S_2 = \sum_{j=0}^{N-1} (w_j)^2 \tag{A.7}$$

The NENBW value for the window functions in this thesis are given in Section A.4.3.

A.4.2 Number of Frequency Bins

The number of spectral bins (NFFT) in the DFT should be selected based on the frequency resolution required and the impact on the apparent amplitude of coherent signals. The frequency of a feature in an amplitude or PSD plot cannot be determined more precisely than the width of one frequency bin. Finer frequency resolution therefore requires a larger NFFT and a corresponding increase in the variance of the spectral

estimates as the finite information in the time series is divided between more spectral bins. However, in many cases, the frequency broadening effect of a window function will impose a coarser frequency resolution (Section A.4.3 below).

Both coherent signals and incoherent broadband noise can contribute to the value in a spectral bin in a DFT. In the laboratory test case of an applied sinusoidal test signal, this can be approximated as having two contributions: a coherent single frequency sinusoid and any broad-spectrum noise. It is easy to forget that the amplitude of a spectral feature corresponding to a sinusoidal test signal has a non-zero contribution from the apparent noise floor. Since the sinusoid and the noise floor are not coherent, they add as the sum of their power rather than the sum of their amplitude. For example if in an amplitude spectra, a test signal's apparent amplitude is 10 nT and the apparent noise floor is at 1 nT , the relative contributions are approximately:

$$\begin{aligned} \text{Apparent Amplitude} &= \sqrt{(\text{Sine Amplitude})^2 + (\text{Noise Amplitude})^2} && \text{(A.8)} \\ 10 &= \sqrt{(\text{Sine Amplitude})^2 + (1)^2} && \text{(A.9)} \\ \Longrightarrow \text{Sine Amplitude} &= 0.95 && \text{(A.10)} \\ & && \text{(A.11)} \end{aligned}$$

or about a 5% measurement error. This error becomes increasingly large as the amplitude of a spectral feature nears the apparent noise floor. Fortunately, the apparent noise floor can be arbitrarily lowered by increasing NFFT. If amplitude accuracy is important, NFFT should be sufficiently large that its contribution to the amplitude measurement is well below the measurement error (See Sections A.6 and A.7 for examples). Alternatively, an estimate of the contribution of the noise floor can be removed mathematically; however, this is complicated in data with many spectral features and was not attempted in this thesis.

A.4.3 Window Functions

The DFT implicitly assumes that a signal is periodic; the DFT processes a segment of N samples using cyclic continuation by assuming that the those N samples are infinitely repeated. As a consequence, the DFT usually experiences a discontinuity as is wraps from the last sample to the first sample (the exception would be either a constant signal or a periodic signal who's periodicity exactly matched the segment length). A discontinuity, like a step function, has power content spread over many frequencies and, since the discontinuity doesn't occur in the original time series, the result is the introduction of spurious power into the spectrum. The normal solution is to apply a time domain window function to the segment of N samples such that the amplitude (and potentially the derivatives) of the signal segment is forced to zero or near zero at its start and end, which minimises the effect of the cyclical extension discontinuity.

Many options for window functions, which can be applied to the data, exist and each has a slightly different effect on the transformed signal. In general, it is impossible to simultaneously optimise a window function for both narrow frequency determination and amplitude accuracy so the choice of which window function to apply should reflect what type of measurement is being taken in the spectral domain. A third significant parameter is the degree of spectral leakage whereby energy is spread between frequency bins.

The Hanning window is a well-known and widely used window function. Figure A.1 (A) shows its amplitude in the time domain. Hanning windows are often used for their excellent frequency resolution. Its narrow central peak in the frequency domain will resolve a single frequency sine wave into a narrow spectral feature.

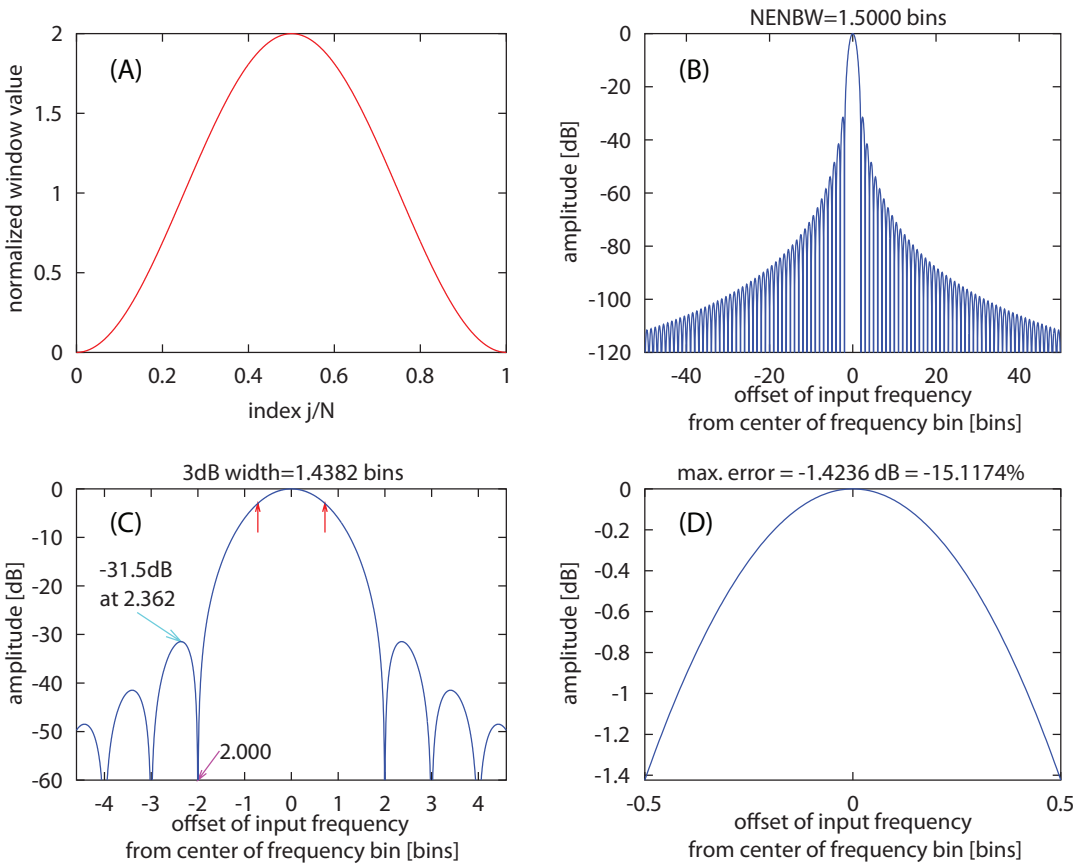

Figure A.1: Parameters of a Hanning window function. (A) shows the normalised window value in the time domain. Plots in blue show the transform of the window function corresponding to the apparent amplitude of a sinusoidal input signal whose frequency is offset from the center of the frequency bin. Since this is a normalised window function, frequency is measured in bins. (C) through (D) show successive zooms of the transfer function compared to offset of the input frequency. Adapted from Heinzel [2002].

However, this spectral resolution comes at a cost. The maximum amplitude error of a window function is the worst case error introduced into the estimation of the amplitude of a sinusoidal signal that may fall anywhere within one frequency bin [Heinzel, 2002]. Figure A.1 (B), (C), and (D) show the transform of the Hanning window showing the amplitude response of the window. Since this is a normalised window function frequency is measured in bins. Figure A.1 (D) shows how the amplitude passed by the window function varies by -1.42 dB within ± 0.5 bins of the central frequency. As a result, the measured amplitude of any signal, even a perfect single frequency sinusoid, will vary by up to

$$-1.42 \text{ dB} = 20 \log_{10} \left(\frac{\text{signal amplitude}}{\text{reference amplitude}} \right) \Longrightarrow \frac{\text{signal amplitude}}{\text{reference amplitude}} = 0.85 \quad \text{(A.12)}$$

or -15% depending on how the sinusoidal signal's frequency compares to the range spanned by the frequency bin (known as scalloping loss). In comparison, the HFT95 window shown in Figure A.2 belongs to the flat-top style of window functions.

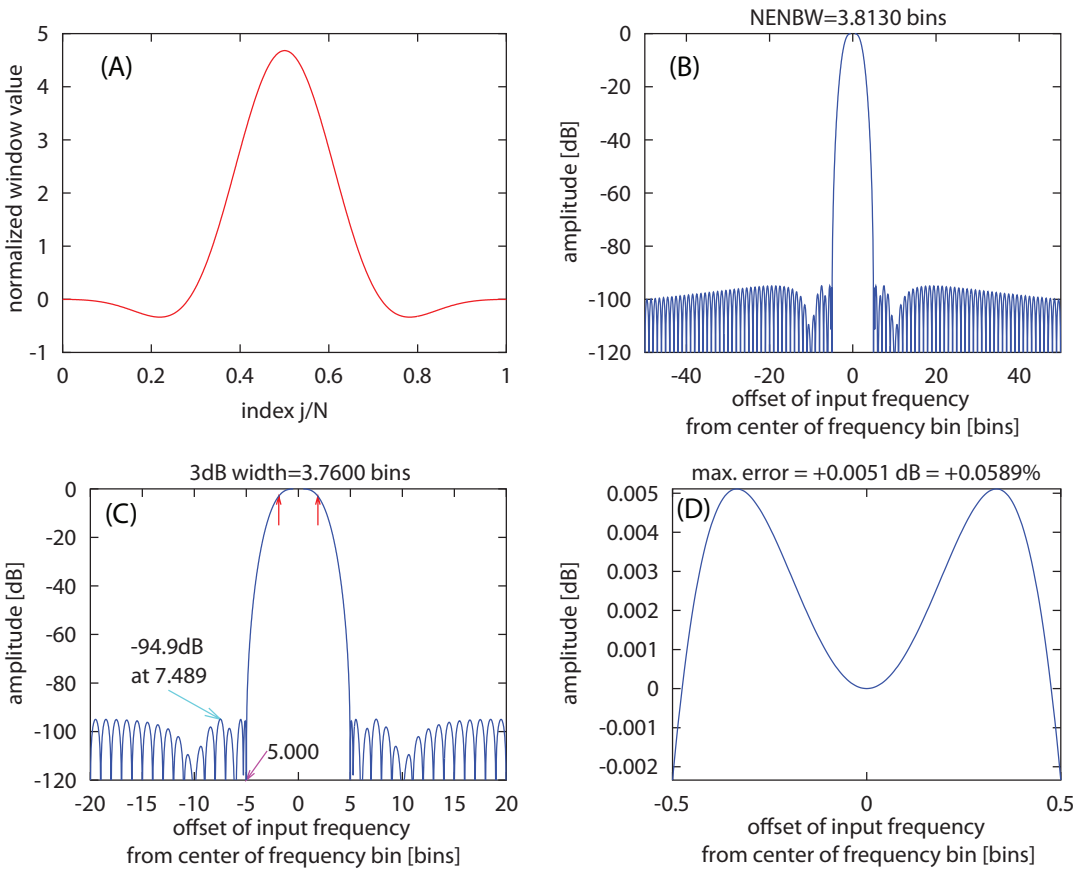

Figure A.2: Parameters of a HFT95 flat-top window function. (A) shows the normalised window value in the time domain. Plots in blue show the transform of the window function corresponding to the apparent amplitude of a sinusoidal input signal whose frequency is offset from the center of frequency bin. Since this is a normalised window function, frequency is measured in bins. (C) through (D) show successive zooms of the transfer function compared to offset of the input frequency. Adapted from Heinzel [2002].

Figure A.2 (D) shows how the amplitude varies by a maximum of +0.0051 dB within ±0.5 bins of the centre of the frequency bin. This provides amplitude measurement accurate, for an ideal single frequency sinusoid, to

$$+0.0051 \text{ dB} = 20log_{10}\left(\frac{\text{signal amplitude}}{\text{reference amplitude}}\right) \Longrightarrow \frac{\text{signal amplitude}}{\text{reference amplitude}} = 1.00059 \tag{A.13}$$

or at worst about +0.06%. However, this increased amplitude resolution comes at the expense of frequency resolution as the central lobe of HFT95 window is broader (-3 dB at 3.76 bins compared to 1.44 bins in a Hanning window). Visually, this has the effect of taking taking a single frequency sine wave, which would peak in one frequency bin using a Hanning window, and broadening it to 3 or 4 bins through the HFT95 flattop window.

Because the Fourier transform of both a window function and a segment of a longer time series have non-zero amplitude in frequency bins away from the central carrier

frequency, power in the input time series will be spuriously deposited in some or all of the spectral bins in a process called "spectral leakage". Consequently, large amplitude signals can swamp nearby (in frequency) small-amplitude signals and will increase the measured value of the incoherent noise floor. Significant 60 Hz tone generated by the power lines is present in both of the test environments used in this thesis and makes precise measurement of nearby frequencies difficult. Similarly, the large static geomagnetic field is often the largest signal present by several orders of magnitude. The average linear trend of all test data was removed before the DFT was calculated so that the total static offset was zero and the resulting spectral leakage was minimized. Removing the static component from the time series invalidates the bottom bin in the spectral transform and, consequently, it is never displayed or used in the results shown in this thesis. The scripts used for the instrument characterisation are presented in Sections A.5.1 and A.5.2 below.

The measurements used to calibrate the instrument were taken using the arithmetic average of the time series of a static magnetic field, rather than using a DFT, and are not subject to window function induced error. The PSD plots use a Hanning window because the frequency broadening effect of flat-top window makes them inaccurate near 0 Hz.

A.4.4 Minimum Spectral Separation

A window function imposes a minimum width on any spectral feature that can be resolved so another important consideration is how close two equal strength signals can be without merging into a single spectral peak. This is usually approximated by the -3.0 dB bandwidth of the window function (cf. Figures A.1 and A.2). However, Harris [1978] showed that, for the coherent addition in a DFT, the -6 dB bandwidth defines the minimum frequency separation of two equal amplitude signals. If the amplitude of the two signals is different, the problem becomes significantly more complex. Minimum spectral separation is more of an issue in telecommunication applications for identifying sidebands. However, the presence of strong spectral features such as 50/60 Hz from the power lines can make it difficult to resolve and quantify nearby (in frequency) test signals especially given the broad spectral peak of the flat-top window (Figure A.2) used for amplitude measurement.

A.4.5 Averaging

The parameters discussed so far relate to the determination of a single spectral estimate based on one segment of a longer time series. However, the results of such an estimate are typically very noisy (have a high variance). The standard deviation of the spectral estimate in one frequency bin is equal to the estimate itself (i.e., 100%) for a stochastic signal. The solution, particularly in an experimental setup where long datasets can be captured, is to take an average of many (M) spectral estimates and hence reduce the standard deviation by $1/\sqrt{M}$.

Welch's method of overlapping periodograms is employed in this thesis to make efficient use of the input data. Figure A.3 shows a continuous data set split into several non-overlapping segments of length N, each of which is processed by a DFT with a window function. Since the window function is usually at or near zero at its boundaries, much of the original time series has little or no contribution to the final averaged periodogram. Figure A.4 shows a schematic of Welch's method of overlapping periodograms. Note how, in general, the edges of each periodogram, which are significantly reduced by the window function, are counted twice restoring a more equal weighting to all portions of the original time series.

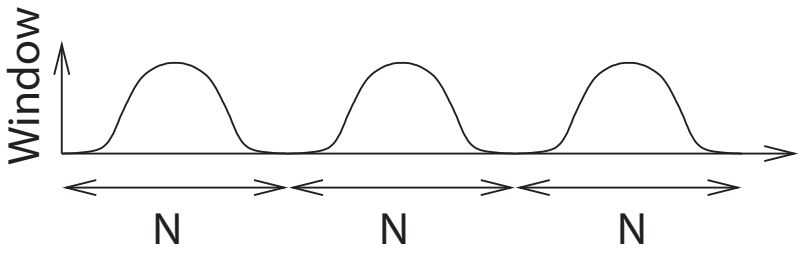

Figure A.3: Segmented windowed time series with no overlap. From Heinzel [2002].

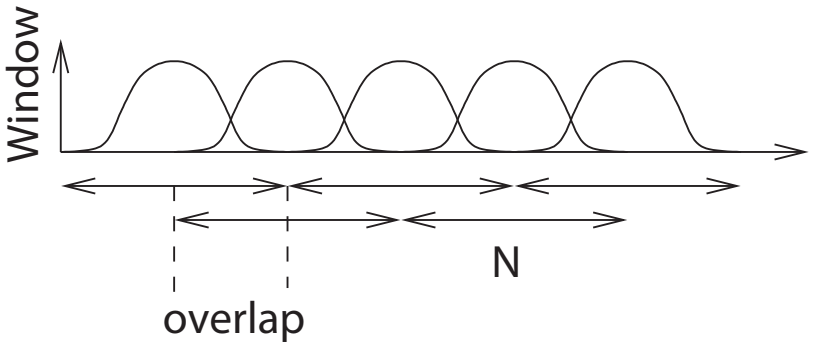

Figure A.4: Segmented windowed time series with overlapping segments. From Heinzel [2002].

A.5 Implementation of Spectral Transforms

A.5.1 Implementation of Power Spectral Density

PSD plots used in this thesis were calculated using the Matlab script below. The linear trend was removed from the overall time series to reduce the effect of spectral leakage from the large static field. The Matlab pwelch algorithm was used to divide the 900 sample per second (sps) original time series into segments of 2,097,152 samples with a 3/4 overlap. Figure 5.14 is an exception and used a larger NFFT to reach very low frequencies. A Hanning window (Figure A.1) was applied to each segment and the resulting unscaled PSD spectrograms were averaged using the arithmetic mean. Finally, the spectrogram was normalised as described in Section A.4.1 to return it to physical units.

```
function [ retVal ] = psdNoiseFloor( time series, Fs, MinFreq )
%psdNoiseFloor Calculates a three component power spectral density spectrum
%   time series should contain 3x time series, Fs contains the sampling
%   frequency, MinFreq contains the minimum frequency of the FFT.

NFFT = 2^nextpow2(Fs/MinFreq)

j=0:1:NFFT-1;
z=2*pi*j/NFFT;
ENBW = 1.5000*Fs/NFFT;

window = hann(NFFT);
detrendedtime series = detrend(time series);
```

```
[Px,f] = pwelch(detrendedtime series(:,1),window,round(3*NFFT/4),NFFT,Fs,'↩
    onesided');
[Py,f] = pwelch(detrendedtime series(:,2),window,round(3*NFFT/4),NFFT,Fs,'↩
    onesided');
[Pz,f] = pwelch(detrendedtime series(:,3),window,round(3*NFFT/4),NFFT,Fs,'↩
    onesided');

ref20pt = ((0.02)^2)./f;
ref10pt = ((0.01)^2)./f;
ref7pt = ((0.007)^2)./f;
ref5pt = ((0.005)^2)./f;

p=loglog(f(3:NFFT/2,:),Px(3:NFFT/2,:), 'Red',f(3:NFFT/2,:),Py(3:NFFT/2,:), '↩
    Green',f(3:NFFT/2,:),Pz(3:NFFT/2,:), 'Blue',f,ref20pt,'red',f,ref10pt, ↩
        'Black',f,ref7pt, 'Cyan',f,ref5pt,'Magenta');

set(p,'LineWidth',1.5)

legend('X - PSD', 'Y - PSD', 'Z - PSD', '20pT/rootHz', '10pT/rootHz', '7pT/↩
    rootHz', '5pT/rootHz');

axis([1e-1 Fs/2 1e-5 1])
xlabel('Fequency (Hz)');
ylabel('Power Spectral Density (nT^2/Hz)');
grid on;
text(0.11, 1.2e-5, ['ENBW = ', num2str(ENBW), ' Signal amplitude varies with ↩
    NFFT. Noise floor is correct'], 'BackgroundColor',[.7 .9 .7]);

retVal = ENBW;
end
```

A.5.2 Implementation of Amplitude Spectrum

Amplitude spectra plots used in this thesis were calculated using the Matlab script shown below. The linear trend was removed from the overall time series to reduce the effect of spectral leakage from the large static field. The Matlab pwelch algorithm was used to divide the 900 sps original time series into segments of 2,097,152 samples with a 3/4 overlap. An HFT95 flat-top windows (Figure A.2) was applied to each segment and the resulting unscaled PSD spectrograms were averaged. Finally, the spectrogram was normalised as described in Section A.4.1 to return it to physical units.

```
function [ retVal ] = ampSpectrum( time series, Fs, MinFreq)
%ampSpectrum Calculates a three component amplitude spectrum with physical ↩
    units
%   time series should contain 3x time series, Fs contains the sampling
%   frequency, MinFreq contains the minimum frequency of the FFT.

NFFT = 2^nextpow2(Fs/MinFreq)
j=0:1:NFFT-1;
z=2*pi*j/NFFT;
ENBW = 3.8112*Fs/NFFT;

hft95win=1 - 1.9383379*cos(z) + 1.3045202*cos(2*z) - 0.4028270*cos(3*z) + ↩
    0.0350665*cos(4*z);
window = hft95win;
detrendedtime series = detrend(time series);

[Px,f] = pwelch(detrendedtime series(:,1),window,3*NFFT/4,NFFT,Fs,'onesided');
[Py,f] = pwelch(detrendedtime series(:,2),window,3*NFFT/4,NFFT,Fs,'onesided');
[Pz,f] = pwelch(detrendedtime series(:,3),window,3*NFFT/4,NFFT,Fs,'onesided');

Ax = sqrt(Px*ENBW);
```

```
Ay = sqrt(Py*ENBW);
Az = sqrt(Pz*ENBW);

p=loglog(f,Ax,'red',f,Ay,'green',f,Az,'blue');

set(p,'LineWidth',1.5)
legend('X - nT RMS','Y - nT RMS','Z - nT RMS');
xlabel('Fequency (Hz)');
ylabel('Amplitude (nT RMS)');
grid on;
axis([MinFreq Fs/2 1e-4 1])
text(0.11, 1.2e-4, ['ENBW = ', num2str(ENBW), ' Signal amplitude is correct. ↩
    Noise floor varies with NFFT'], 'BackgroundColor',[.7 .9 .7]);

retVal = ENBW;
end
```

A.6 Performance Using Synthetic Data

Figures A.5 and A.6 show the result of testing the amplitude spectrum and PSD scripts against idealised synthetic data. Figure A.5 shows the transform of a pure 50 pT-pp (17.7 pT-RMS) 10 Hz test signal with a length of one hour at 900 sps. In the amplitude spectrum, the spectral peak at 10 Hz coincides with the exact amplitude and frequency of the test signal (horizontal and vertical red lines) and is independent of the value of NFFT. In the PSD plot, the spectral peak at 10 Hz grows with the value of NFFT.

Figure A.6 uses the same 50 pT-pp (17.7 pT-RMS) 10 Hz test signal but adds a simulated white-noise of about 6×10^{-6} nT^2/Hz. In the amplitude spectrum, the spectral peak at 10 Hz is independent of NFFT, and matches the exact amplitude and frequency of the test signal (horizontal and vertical red lines), provided the sinusoidal signal is much larger than the apparent noise floor. However, the apparent amplitude of the noise floor varies with with NFFT. In the PSD plot, the spectral peak at 10 Hz grows with the value of NFFT. However, the amplitude of the noise floor is constant with NFFT.

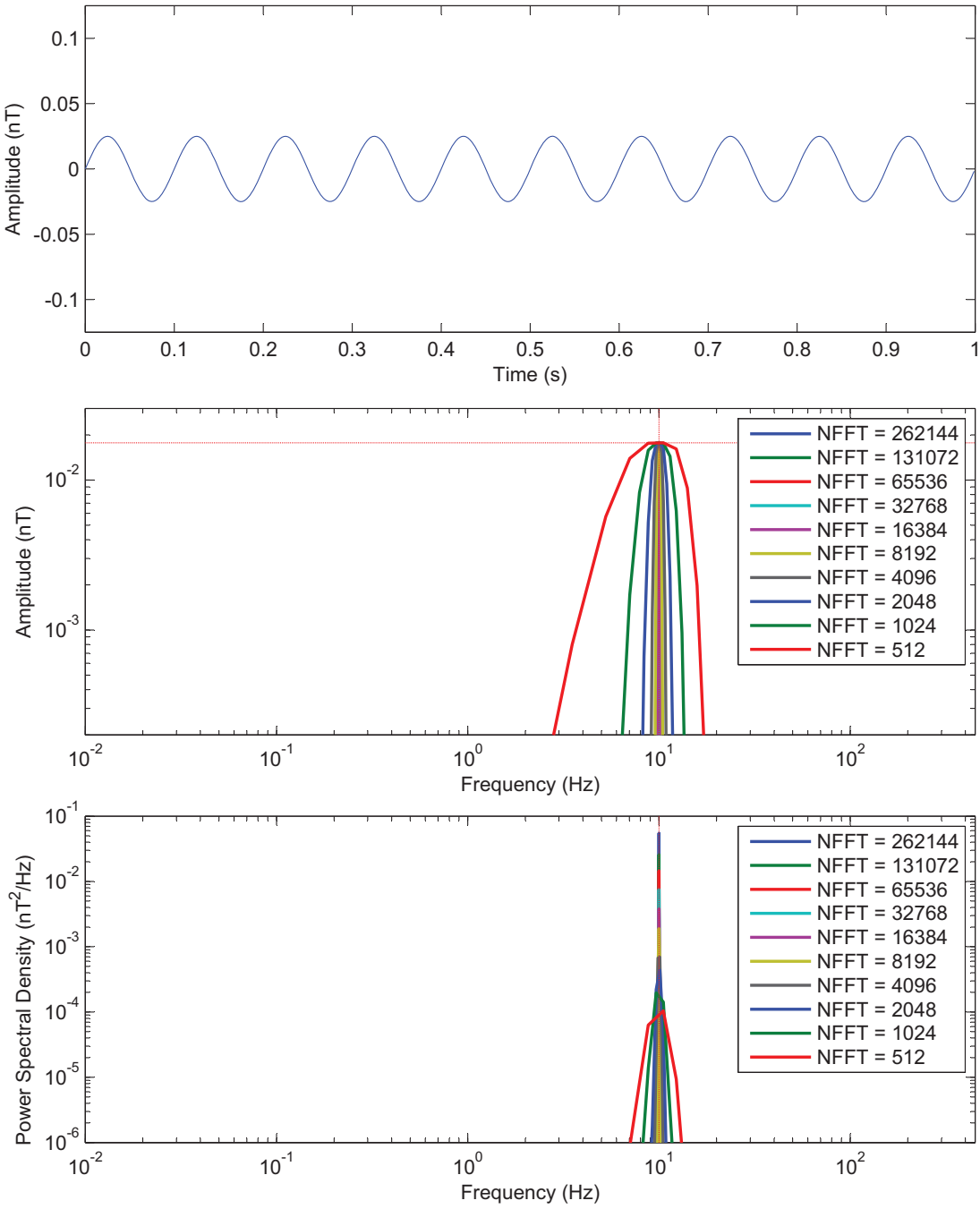

Figure A.5: Performance of spectral analysis using synthetic data of a 50 pT-pp (17.7 pT-RMS) 10 Hz test signal. The top panel shows one second of the synthetic time series. Middle panel shows the resulting averaged periodogram of the amplitude spectrum. The vertical and horizontal red bars show the exact amplitude and frequency of the sinusoidal signal. Bottom panel shows resulting averaged periodogram of the power spectral density spectrum. The vertical red line shows the exact frequency of the sinusoidal signal.

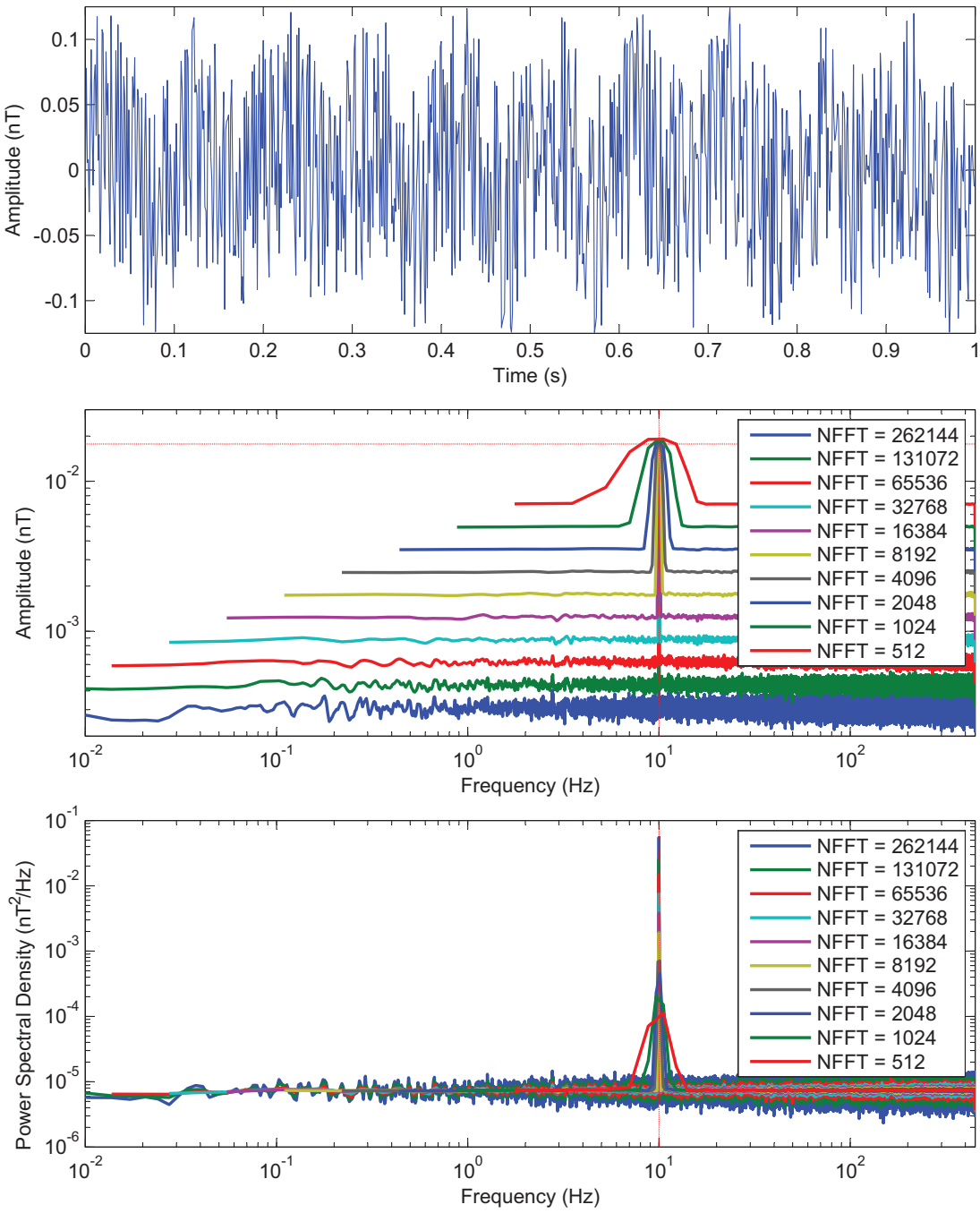

Figure A.6: Performance of spectral analysis using synthetic data of a 50 pT-pp (17.7 pT-RMS) 10 Hz test signal with a simulated white-noise of about 6×10^{-6} nT^2/Hz. Top panel shows one second of the synthetic time series. Middle panel shows the resulting averaged periodogram of the amplitude spectrum. The vertical and horizontal red lines show the exact amplitude and frequency of the sinusoidal signal. The bottom panel shows resulting averaged periodogram of the power spectral density spectrum. The vertical red line shows the exact frequency of the sinusoidal signal.

A.7 Performance Using Measured Data

Figures A.7, A.8, A.9, A.10, repeat the analysis of Section A.6 using experimental data. The input time series was taken in the CARISMA laboratory using a sensor that was hand-aligned within the test solenoid (See Section 5.1.2). Due the misalignment error, the absolute value of the measured signal is not expected to match that of the applied 50 pT-pp (17.7 pT-RMS) 10 Hz test signal. However, since all the spectra are calculated from the same original time series of measurements, any apparent difference in amplitude is due entirely to data processing.

A.7.1 Performance of Power Spectral Density Spectrum Calculation

Figure A.7 shows a sequence of PSD spectra calculated with different values of NFFT. The PSD of the incoherent noise floor is essentially constant regardless of NFFT. However, coherent signals such as the 10 Hz test sinusoid and the 60 Hz power-supply tone vary strongly with NFFT. Figure A.8 shows the same sequence of PSD spectra but is zoomed onto the 10 Hz test signal. Table A.2 shows the measured PSD of a sine wave test signal as measured by the relevant bin of the psdNoiseFloor script using different values for NFFT. Note how the measured value of the spectral peak at 10 Hz grows with NFFT.

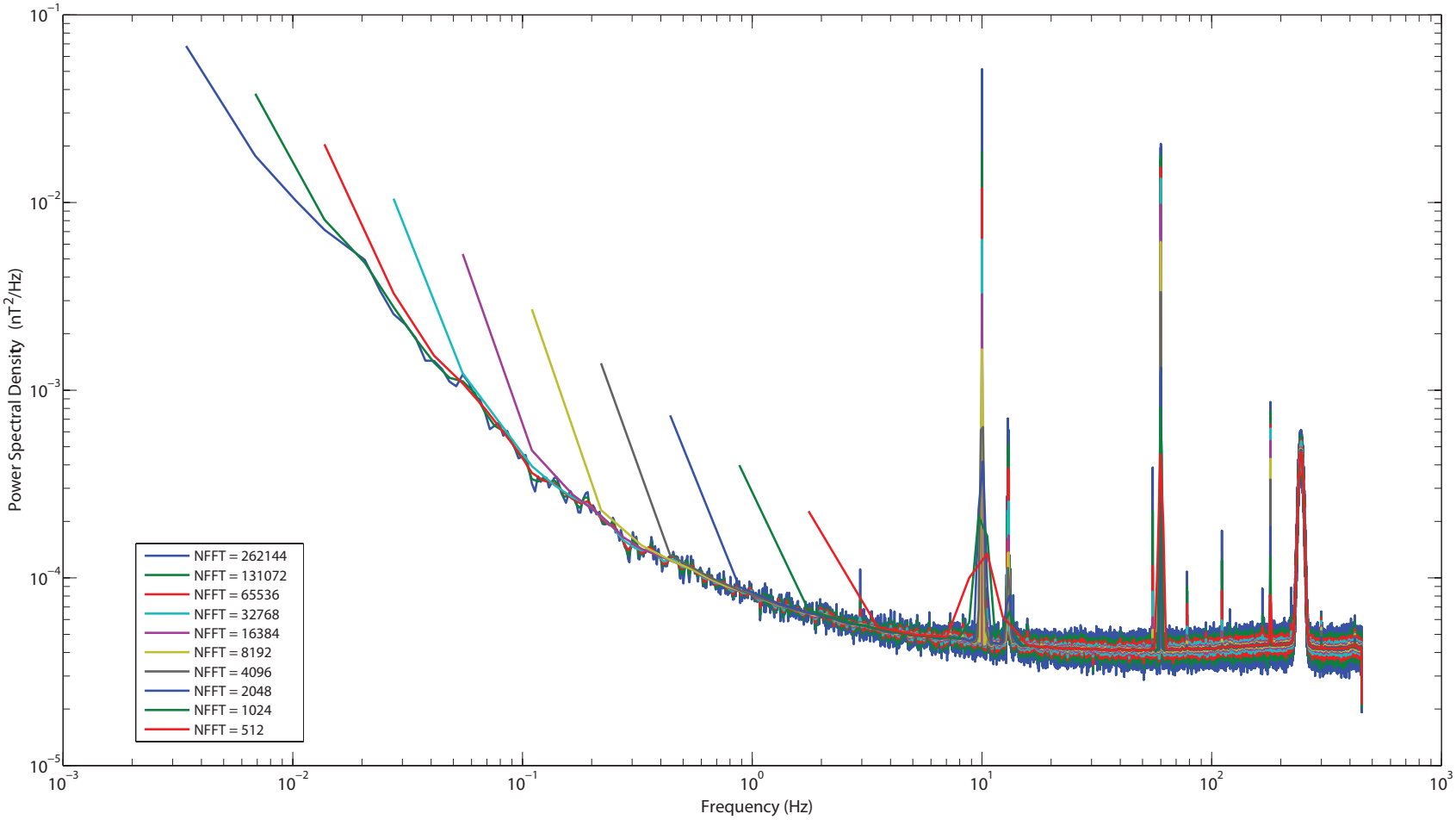

Figure A.7: Power spectral density plots of a 50 pT-pp (17.7 pT-RMS) 10 Hz sine wave at various values of NFFT. The amplitude of the measured noise floor is independent of the number of spectral bins NFFT. However, the amplitude of the coherent test signal at 10 Hz and the coherent 60 Hz power line tone both vary with NFFT.

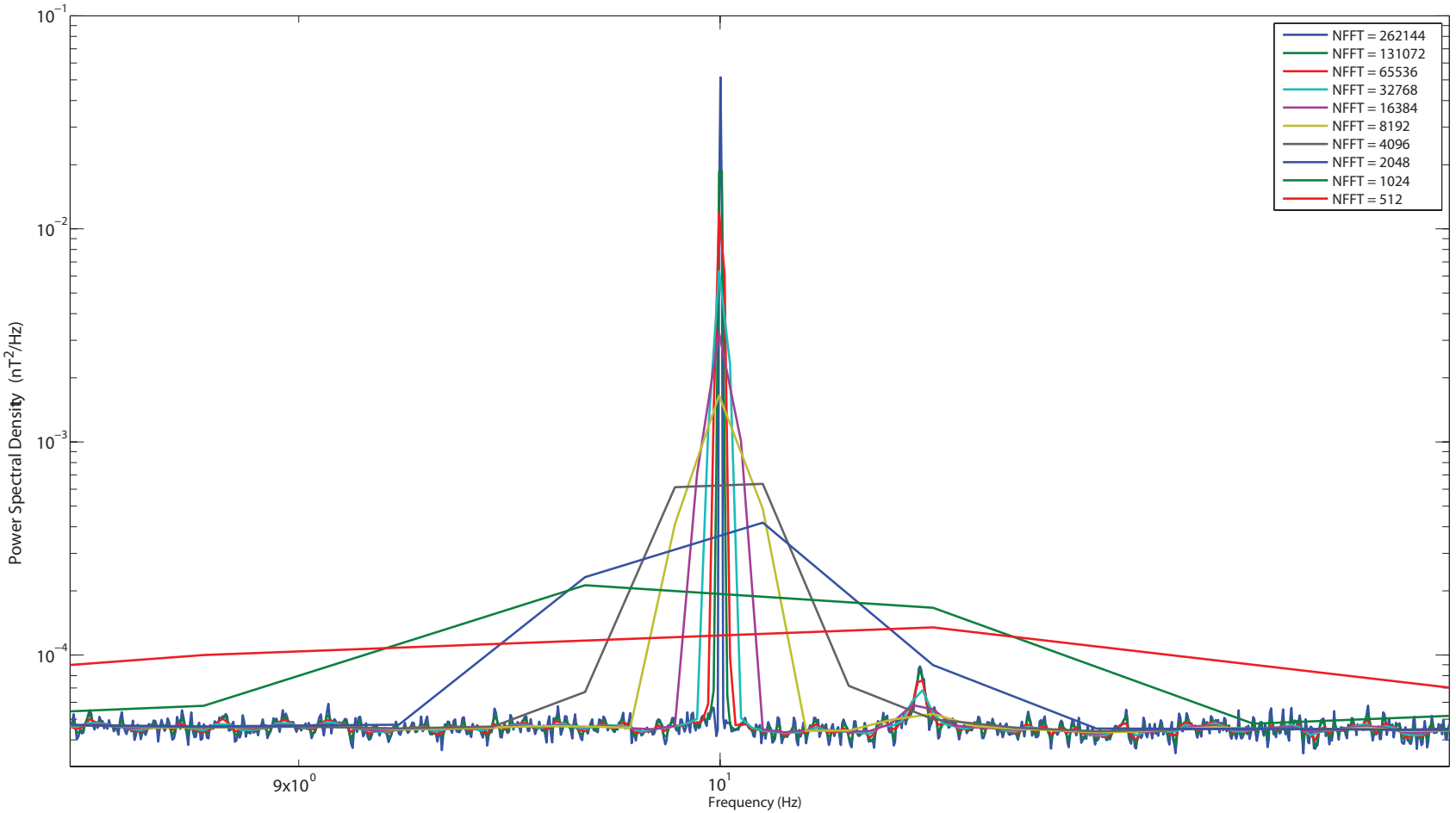

Figure A.8: Zoomed power spectral density plots of a 50 pT-pp (17.7 pT-RMS) 10 Hz sine wave at various values of NFFT. The amplitude of the measured noise floor is independent of NFFT. However, the amplitude of the coherent test signal at 10 Hz varies with NFFT.

NFFT (bins)	Measured PSD (nT^2/Hz)
512	0.000078
1024	0.000102
2048	0.000151
4096	0.000257
8192	0.000473
16384	0.000904
32768	0.001747
65536	0.003435
131072	0.006848
262144	0.013506

Table A.2: Measured amplitude of a 50 pT-pp (17.7 pT-RMS) 10 Hz sine wave test signal using different values of NFFT. The measured value in PSD varies with NFFT.

A.7.2 Performance of Amplitude Spectrum Calculation

Figure A.9 shows a sequence of amplitude spectra calculated with different NFFT values. The amplitude of the coherent test signal at 10 Hz is essentially independent of NFFT provided the signal is much larger than the noise. However, the amplitude of the noise varies with NFFT. Figure A.10 shows the same sequence of amplitude spectra but is zoomed onto the 10 Hz test signal.

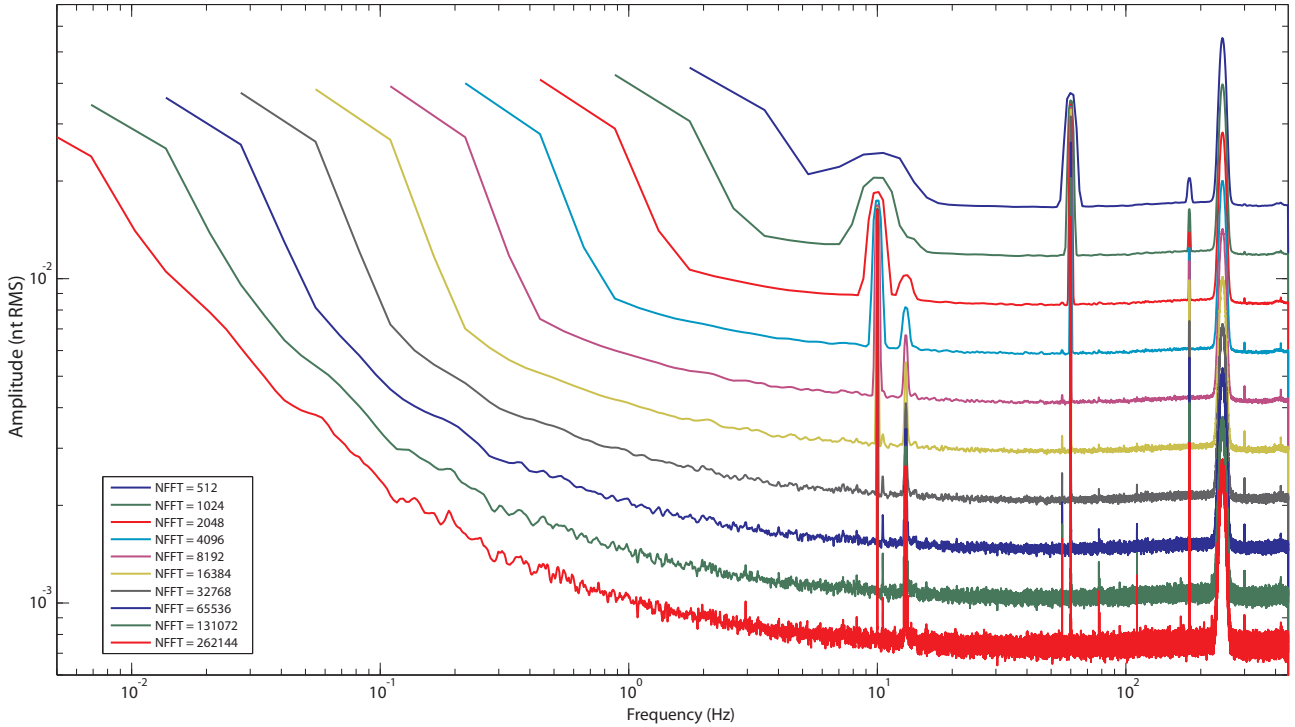

Figure A.9: Amplitude spectra density plots values of a 50 pT-pp (17.7 pT-RMS) 10 Hz sine wave at various values of number of spectral bins (NFFT). The amplitude of the coherent test signal at 10 Hz is independent of NFFT provided the signal is much larger than the apparent noise floor. However, the amplitude of the noise floor varies with with NFFT.

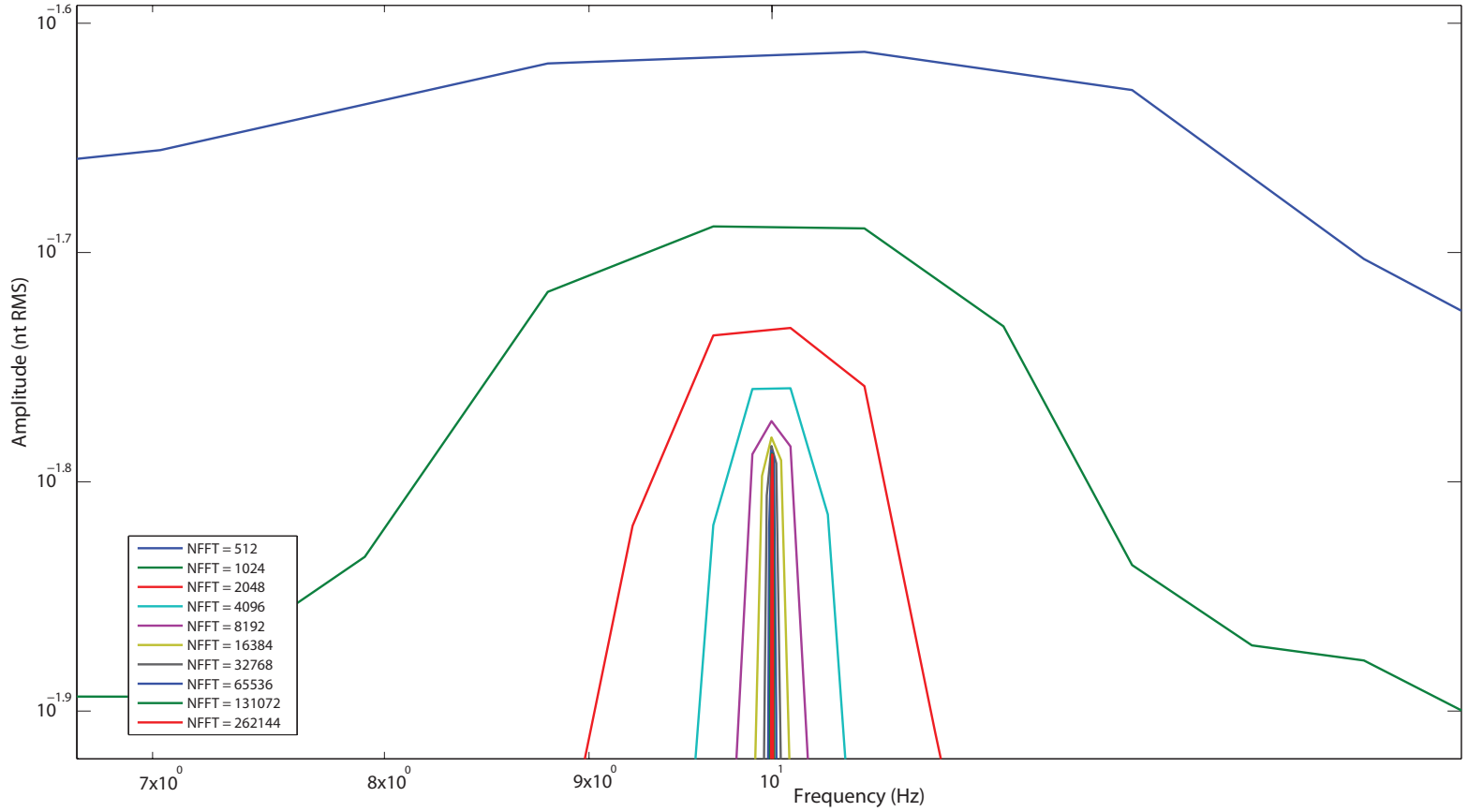

Figure A.10: Zoomed amplitude measurement of a 50 pT-pp (17.7 pT-RMS) 10 Hz sine wave test signal at various NFFT. Note how the test signal amplitude tends to a constant as NFFT increases and the contribution of the incoherent noise floor becomes small.

Table A.3 shows the amplitude of a sine wave test signal as measured by the relevant bin of the ampSpectrum script using different values for NFFT. The estimated error column is calculated as the percent difference assuming that the amplitude measured using NFFT = 262,144 is correct. Figure A.11 plots the measured amplitude versus NFFT and shows how the measured amplitude tends towards a constant (assumed correct) value as the number of spectral bins increases and the effective contribution of the apparent noise floor decreases. Further improvements to the amplitude estimation may be possible by estimating and subtracting the contributions of the noise floor; however, this is complicated by the large number of spectral features caused by environmental noise and was not attempted within this thesis.

NFFT (bins)	Measured Amplitude (nt)	Estimated Error (%)
512	0.027898	72.34
1024	0.022456	38.72
2048	0.019356	19.57
4096	0.017878	10.44
8192	0.017138	5.87
16384	0.016754	3.49
32768	0.016467	1.72
65536	0.016326	0.85
131072	0.016301	0.70
262144	0.016188	Assumed to be 0

Table A.3: Measured amplitude of a 50 pT-pp (17.7 pT-RMS) 10 Hz sine wave test signal using different values of NFFT. The estimated error is calculated as the percent difference assuming that the amplitude measured using NFFT = 262,144 is correct.

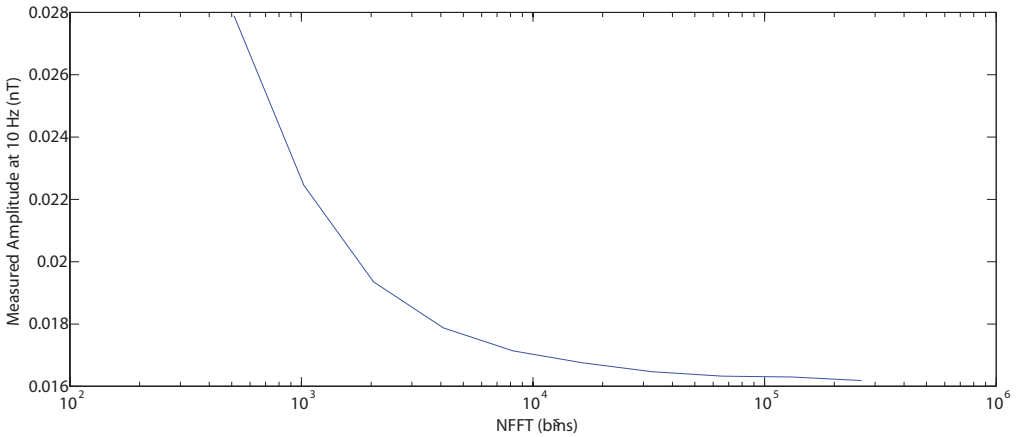

Figure A.11: Measured amplitude of a 50 pT-pp (17.7 pT-RMS) 10 Hz sine wave test signal using different values of NFFT.